RADIATION INDUCED NANOCRYSTAL FORMATION IN METALLIC GLASSES

A Dissertation

by

JESSE CARTER

Submitted to the Office of Graduate Studies of
Texas A&M University
in partial fulfillment of the requirements for the degree of

DOCTOR OF PHILOSOPHY

August 2009

Major Subject: Nuclear Engineering

RADIATION INDUCED NANOCRYSTAL FORMATION IN METALLIC GLASSES

A Dissertation

by

JESSE CARTER

Submitted to the Office of Graduate Studies of
Texas A&M University
in partial fulfillment of the requirements for the degree of

DOCTOR OF PHILOSOPHY

Approved by:

Chair of Committee,	Lin Shao
Committee Members,	Raymond Juzaitis
	Sean McDeavitt
	Xinghang Zhang
Head of Department,	Raymond Juzaitis

August 2009

Major Subject: Nuclear Engineering

ABSTRACT

Radiation Induced Nanocrystal Formation in
Metallic Glasses. (August 2009)
Jesse Carter, B.S., Texas A&M University;
M.S., Texas A&M University
Chair of Advisory Committee: Dr. Lin Shao

The irradiation of metallic glasses to induce nanocrystallization was studied in two metallic glass compositions, $Cu_{50}Zr_{45}Ti_5$ and $Zr_{55}Cu_{30}Al_{10}Ni_5$. Atomic mobility was described using a model based on localized excess free volume due to displacement cascades created by energetic particle irradiation. Due to the difference in cascade size among different masses of projectiles, a mass-dependent study was performed. Metallic glass ribbon samples produced by melt-spinning were bombarded with electron, He, Ar, and Cu particles. Electron irradiation and characterization was performed "in-situ" by means of transmission electron microscopy. The different metallic glasses showed dissimilar levels of radiation stability under electron irradiation by $Cu_{50}Zr_{45}Ti_5$ forming crystals 1-10 nm in diameter embedded in the amorphous matrix after about 30 minutes of irradiation, while $Zr_{55}Cu_{30}Al_{10}Ni_5$ showed no such crystallization. Increasing projectile mass caused an increase in the maximum nanocrystal diameter up to approximately 100 nm in Cu irradiated $Zr_{55}Cu_{30}Al_{10}Ni_5$. Studies of diffraction patterns of irradiated specimens showed nucleation of $Cu_{10}Zr_7$ phases in both specimens, as well as evidence of $CuZr_2$ in $Cu_{50}Zr_{45}Ti_5$ and both $CuZr_2$ and $NiZr_2$ in $Zr_{55}Cu_{30}Al_{10}Ni_5$. Crystal sizes in irradiated $Zr_{55}Cu_{30}Al_{10}Ni_5$ specimens showed bimodal distribution with many large (50-100 nm) crystals and many small (1-5 nm) crystals. The small crystals in irradiated $Zr_{55}Cu_{30}Al_{10}Ni_5$ were determined to be $NiZr_2$ phase because of the low abundance of Ni. After exposure to 2 keV

Ar ions, areas of composition roughly $Cu_{10}Zr_7$ were found by energy-dispersive X-ray spectroscopy but no crystallization was found. Further crystallization was achieved in decomposed specimens after electron irradiation. This shows that atomic segregation is a necessary step before nucleation in metallic glasses.

To Tess. Without her I would still be in school.

ACKNOWLEDGMENTS

I would like to thank the numerous people who helped me with this project. My committee members, Dr. Raymond Juzaitis, Dr. Sean McDeavitt, and Dr. Xinghang Zhang, have been very helpful in providing me with feedback about this project. They were able to provide a new and insightful comments on my data and point out inconsistencies. My committee also helped me to consider possible applications of my research where I was too caught up with the details. I would not have such a clear and consistent dissertation without them. Another colleague, Engang Fu, has been indispensable in this project. Engang has spent countless hours with me doing TEM into the late night hours, even on weekends and holidays. He was very resourceful in learning the proper ways to prepare samples and characterize them. I learned from him how to think about a problem from all angles. My colleages in my laboratory have been very helpful and kind while sharing laughs and frustrations. I would like to mention Michael Martin and Mark Hollander. They helped every step of the way and will be good friends for a long time. Most importantly, I would like to thank my advisor Dr. Shao. He has inspired and encouraged me through every step of this project. He was especially motivational when I lacked motivation. Without him, this project would never be finished.

TABLE OF CONTENTS

LIST OF TABLES

LIST OF FIGURES

FIGURE Page

FIGURE Page

FIGURE Page

FIGURE Page

FIGURE Page

FIGURE Page

CHAPTER I

INTRODUCTION

Metallic glasses have been of great interest in the past several decades due to their unique properties. What makes this material so unique is that it is an amorphous metallic alloy; there is no long-range atomic order. Since this is in contrast to conventional metallic alloys, metallic glasses have the ability to reach new heights in mechanical performance. For example, they exhibit strength superior to conventional polycrystalline alloys of similar composition and are also very corrosion resistant. Due to such unique performance, many applications of metallic glasses have been developed in both bulk (thick) and thin film specimens.

A wealth of knowledge has already been compiled regarding the mechanical performance and behavior of metallic glasses [1, 2, 3, 4, 5, 6]. A graphical representation metallic glass superiority regarding tensile strength can be seen in Fig. 1, taken from [1]. Metallic glasses based on the Cu-Zr-Ti and Cu-Hf-Ti systems have shown tensile strength on the order of 2000 MPa [7], and an Fe-B based metallic glass recently demonstrated compressive fracture strength of 4200 MPa [8]. In comparison, steel alloys exhibit yield strengths which do not typically exceed 1000 MPa [9]. The Vicker's hardness of metallic glasses exhibit a similar trend to Fig. 1 [1]. In general, metallic glasses have the potential to exhibit higher strength than any crystalline alloy. In the realm of corrosion resistance, there have been reports of metallic glasses with extremely high corrosion resistance such as Fe-Cr-P-C [10] and Cu-Zr-Ti [11]. Metallic glasses also have superior magnetic properties. As an example, it has been shown that amorphous metals can improve electrical transformer technology. When metallic

---

The journal model is *IEEE Transactions on Automatic Control*.

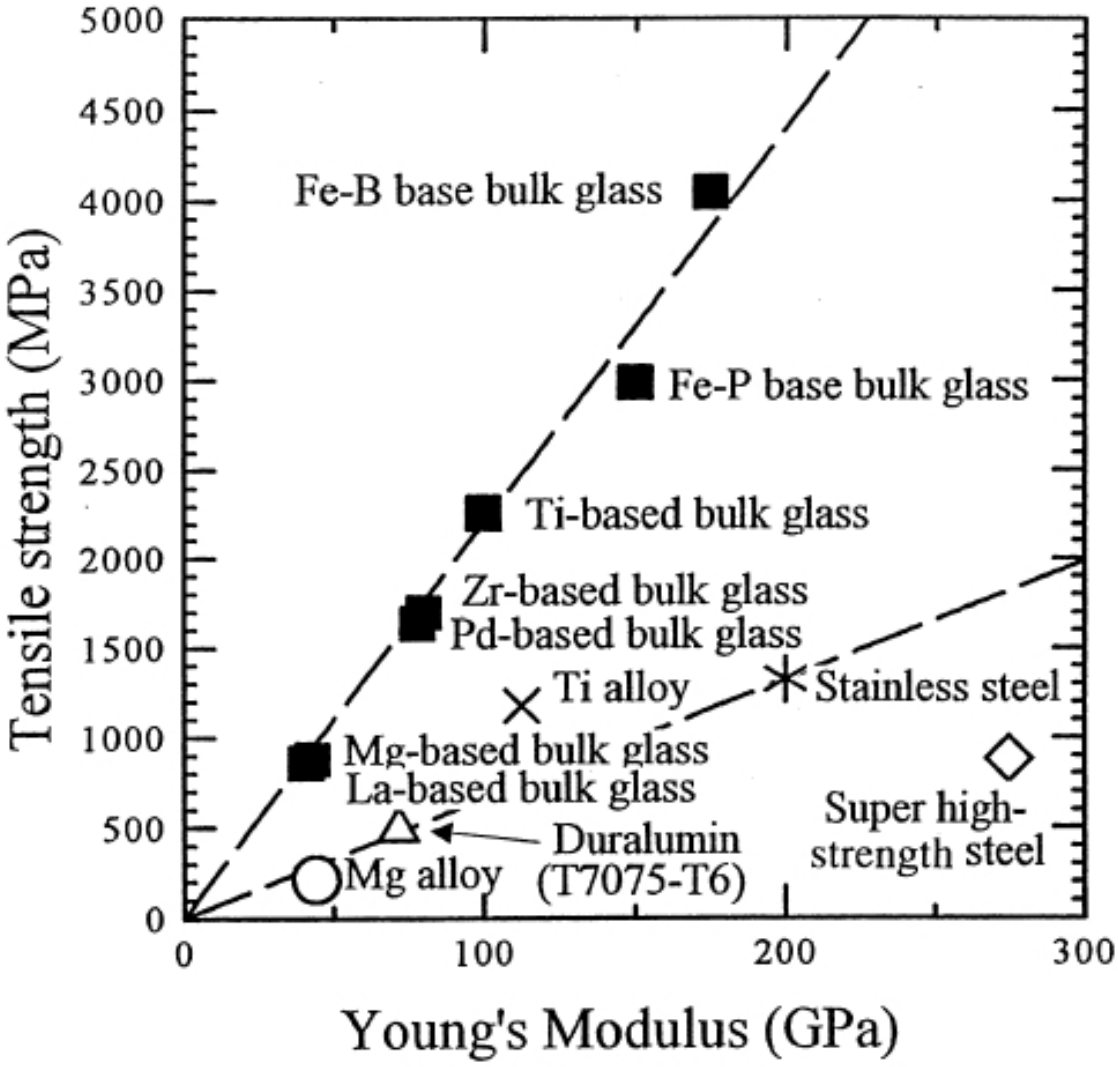

Fig. 1. Tensile strength of bulk metallic glasses and other conventional alloys plotted against Young's modulus.

glass ribbon is used as transformer core material rather than conventional nickel-iron material, transformer performance is improved while decreasing the amount of material necessary [12]. With such excellent bulk properties, bulk metallic glasses are immediately attractive for many applications.

Metallic glasses also show high hardness which has lead to applicability in small and thin film coatings of materials and devices. For instance, metallic glass, more specifically Vitreloy, was used by Surgical Specialties to produce scalpel blades. The blades were sharper and lasted longer than steel blades and were easily produced from a single mold. Also, metallic glass films are hard and very scratch resistant, so naturally thin film coatings have been used as protective coatings on electronic devices, such as cell phones [13].

A famous example of practicality with bulk metallic glasses is the use as face material in golf clubs. The material used was one of the first commercially produced metallic glasses. This proprietary alloy was trademarked as "Vitreloy" and the atomic composition was $Zr_{41.2}Ti_{13.8}Cu_{12.5}Ni_{10}Be_{22.5}$, commonly referred to as Vitreloy 1 or "Vit1". The alloy was developed by a team from the California Institute of Technology in the early 1990's [14] who started a company called Liquidmetal Technologies. Owing to the unconventional amorphous nature of the club head face, the material was twice as hard and four times as elastic as Ti drivers which allowed 99% of the impact energy to be transferred to the ball [13]. However, studies on the club showed some fractured and crystallized regions in the club leading to lower strength in the crystallized region and the long term reliability was called in to question [15]. It is the subject of this dissertation to investigate a novel way to remedy the brittle fracture of metallic glasses. The approach will be discussed later.

The unique properties of metallic glasses come from the unique microstructure of the material, or lack thereof. In order to understand the difference between metallic

glasses and conventional metallic alloys, some properties of the latter will be discussed. Historically, great efforts have been made to create metallic alloys with superior strength. Almost invariably, large-scale engineering materials will be made of numerous tiny grains and lots of work has gone into designing alloy production processes to create polycrystalline alloys with specific grain sizes, among other characteristics. This idea can be dated back to as early as 1951 in what is commonly referred to as the empirical "Hall-Petch" relationship where the yield stress (and other mechanical properties) is inversely proportional to the square root of the average grain diameter [16, 17]. Experimental data demonstrating this relationship is shown in Fig. 2 for low-carbon steel [18]. When the yield strengths of materials are plotted against the square root of the average grain size, they very closely approximate a straight line. The Hall-Petch relationship is derived from the concept that grain boundaries act as barriers to dislocation movement. As the material contains more barriers for dislocation movement, it becomes effectively strengthened. While the Hall-Petch proportionality does not hold as the grain size goes to zero, it does have applicability to grain size domains of practical measure, such as micron to millimeter sized grains.

The addition of grain boundaries to a material, a process commonly called grain boundary strengthening [9], is not without drawbacks. In effect, the very process that gives polycrystalline alloys their enhanced strength brings about more failure mechanisms. The grain boundaries themselves have high interfacial energy. Such high energy leads to formation centers for diffusion, corrosion, and cracking. The diffusion of elements towards and away from grain boundaries is an important mechanism in a highly undesirable phenomenon in nuclear reactor steels called "Irradiation Assisted Stress Corrosion Cracking (IASCC)" [19, 20, 21].

In a related effort, General Electric has claim to the world's largest single crystal

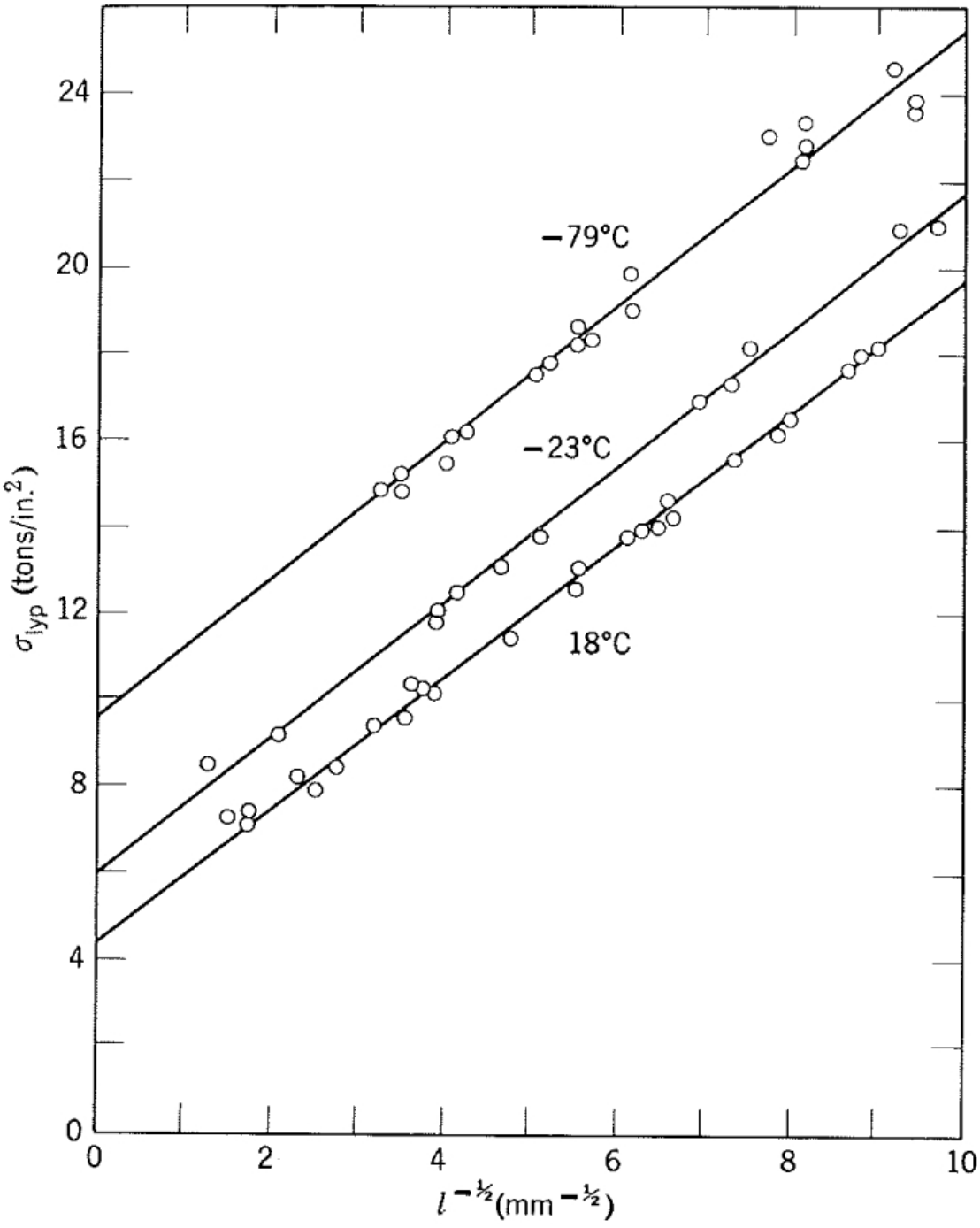

Fig. 2. Yield strength of low-carbon steel versus the inverse square root of average grain diameter at different temperatures.

Source: [18].

turbine engine blade. These 18 inch, 30 pound single crystals were developed to eliminate grain boundaries altogether. Before the development of single crystal turbine blades, the corrosion, cracking, and other phenomena occurring at grain boundaries led to shorter blade lifetimes and required lower operating temperatures which decreased the turbine's overall efficiency. From the elimination of grain boundaries, the single crystal turbine blades now exhibit longer thermal and fatigue life, are more corrosion resistant, and can operate at higher temperatures [22]. Metallic glasses also are devoid of grain boundaries, but they do so in a much different way. Instead of being completely ordered, the microstructure of metallic glass is completely disordered, so there are no domains of crystal structure at all. This at least in theory will give the metallic glass the ability to perform exhibit desirable characteristics like those seen in the single crystal engine blades.

Much like the grains in polycrystalline materials, the random atomic arrangement in metallic glasses gives it its strength but also is the cause for its downfall. The deformation mechanism in metallic glass is much different than in crystalline materials. Basically, when a metallic glass deforms due to a stress, the deformation is highly inhomogeneous and localized to small zones. This is in direct contrast to deformation in polycrystalline metals. When a polycrystalline material plastically deforms, the strain is spread throughout the volume and the whole material becomes stronger - a process known as work hardening or strain hardening [9]. When a metallic glass is loaded, the deformation continues in the same zone and the material is effectively weakened in that area.

Generally, the resulting strain in a metallic glass takes the form of shear band, a region of highly localized plastic deformation, which can spread throughout the entire material. It is due to this type of strain that metallic glasses usually fracture quickly in a brittle fashion. In a tensile test where a material is stressed until failure,

metallic glasses tend to fracture after elongation of only a few percent, sometimes two percent or less. Metallic glasses behave similarly in bending tests. For example, Figs. 3 (from [23]) and 4 show shear banding in metallic glass specimens under loading conditions. In each case, multiple shear bands are seen forming deep into the material and appear to be the only strain that exists in the specimen. The strain exists in a small portion of the specimen and the remaining portion appears undamaged. In contrast, polycrystalline materials can often withstand large deformation, ten percent in some cases, before fracture. Once again the reason for the differences goes back to the atomic microstructure. Once the shear bands form in the amorphous alloy, there is quite simply nothing to stop them.

The lack of ductility in metallic glasses is perhaps the largest barrier to widespread use in technology and engineering. The high strength and hardness of metallic glasses makes it appear very viable, but those properties come at a cost. The solution to the ductility problem comes in the form of nanostructured or composite amorphous metallic alloys. The idea is simply to put some structure into the alloy so that when shear bands do form, they are either stopped or forced to be too small to cause catastrophic failure. Careful consideration must be taken to design an alloy such that when ductility is enhanced, the benefits of having an amorphous metal are not lost.

There have been several advances in improving ductility in metallic glasses. For example, a group at California Institute of Technology showed increased ductility exceeding 10% [24]. The glass was a Zr-Ti-Nb-Cu-Be alloy and processed to introduce a large volume fraction (about 50%) of a body-centered cubic solid solution dendritic phase mixed in the amorphous glass matrix. The ratio of Be was varied to produce three different compositions. Engineering stress-strain tensile tests were performed on the three composites as well as "Vit1" for comparison, and are shown in Fig. 5.

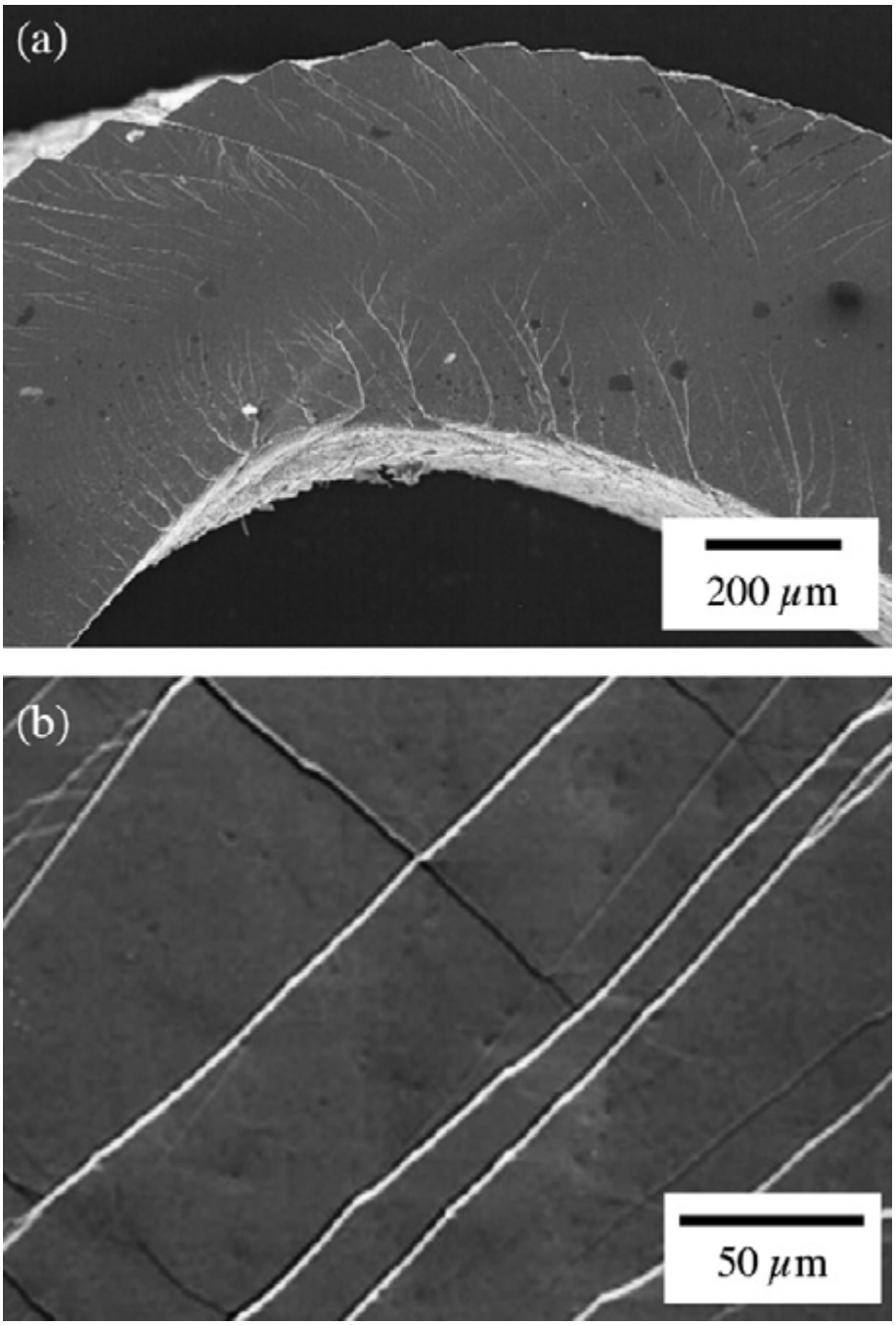

Fig. 3. Scanning electron micrographs demonstrating shear banding in (a) $Zr_{57}Nb_5Al_{10}Cu_{15.4}Ni_{12.6}$ subject to bending and (b) $Zr_{52.2}Cu_{17.9}Ni_{14.6}Al_{10}Ti_5$ subject to compression.

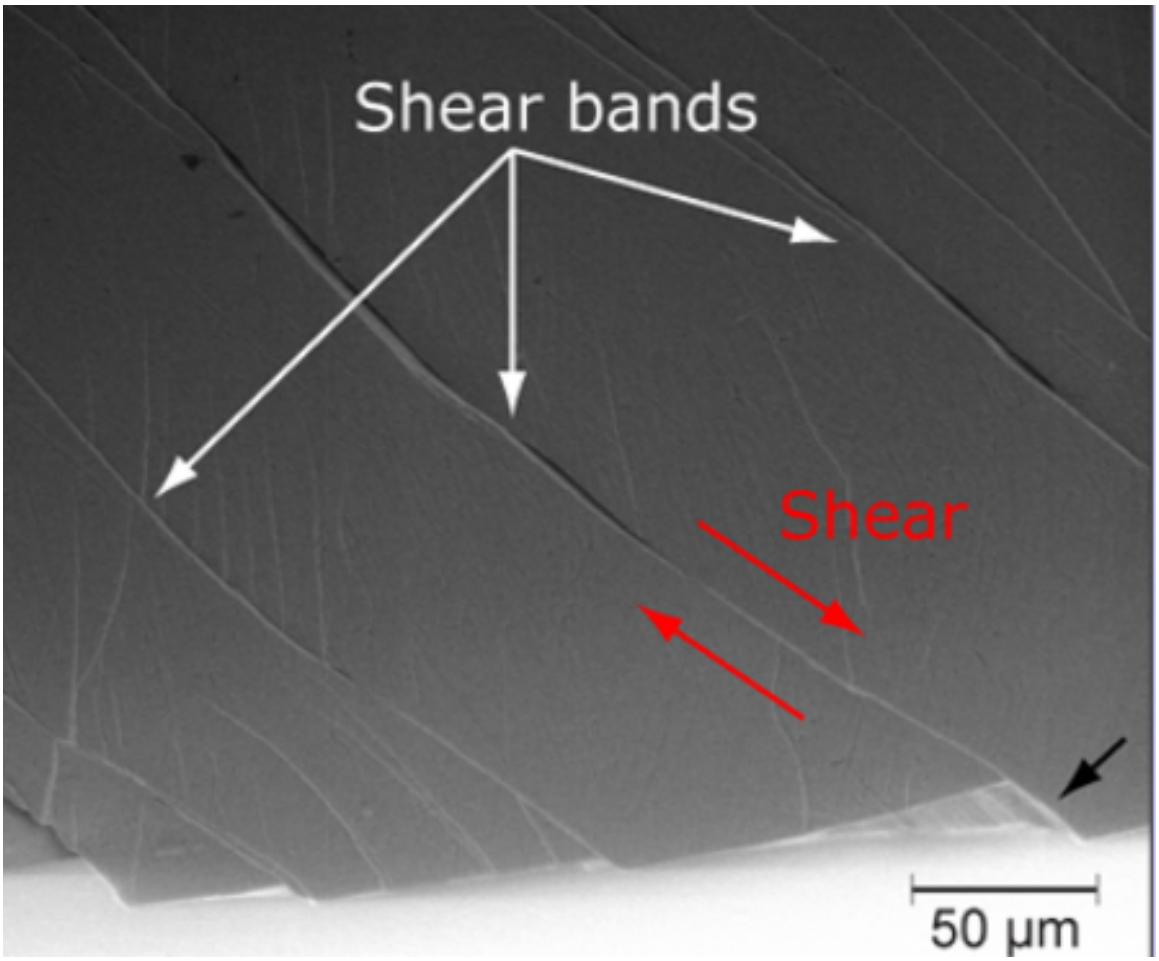

Fig. 4. Scanning electron micrograph of shear banding in metallic glass specimen subject to bending.

Source: Hufnagel Research Group, Johns Hopkins University.

The Vitreloy 1 metallic glass showed high strength but low elongation before failure, as expected. The fractured specimen is shown in Fig. 6. However, the bulk glass composites (DH1, DH2, DH3) showed increasing ductility with slightly decreased tensile strength as the dendrite concentration increased. In the end, a bulk metallic glass composite capable of 12% elongation ending in ductile fracture (necking, not brittle fracture) while maintaining a yield strength greater than 1000 MPa was created. An investigation into the deformation behavior of the glass was made by Scanning Electron Microscopy and is shown in Fig. 7. Two observations can be made regarding the shear banding in the vicinity of the dendrites: 1) Many small shear bands were formed instead of one large band, and 2) the shear bands were arrested at the interface between the glass and the embedded dendrites [24]. These two observations mean that the shear bands are spread more homogenously throughout the sample. This observation is one example of the need to modify the microstructure of metallic glasses in order to give the material a reasonable amount of ductility while maintaining high strength. While this attempt to achieve ductile metallic glasses is considered successful, it must be noted that the process to achieve the dendritic phase involves a complex procedure involving processing the liquid alloy below its melting temperature as a semi-solid, two-phase mixture allowing the dendrites to grow to a size that matches with the deformation scale size of the glass, followed by rapid quenching.

Much work has been done on creating nanostructured metallic glass composites, ie, glass with crystals of nanometer size formed inside [1, 25, 26]. For example, in the work done by Q.S. Zhang et al. [26], rods of $Cu_{50}Zr_{45}Ti_5$ with diameters of 1.5 mm and 2.5 mm were formed and examined. The rods were formed by copper mold casting, a traditional metallic glass production method, but were not found to be completely amorphous (the thickness, to be discussed later, was too large). Instead, the 1.5 mm rod was found to be 96% amorphous by volume with crystals between 2

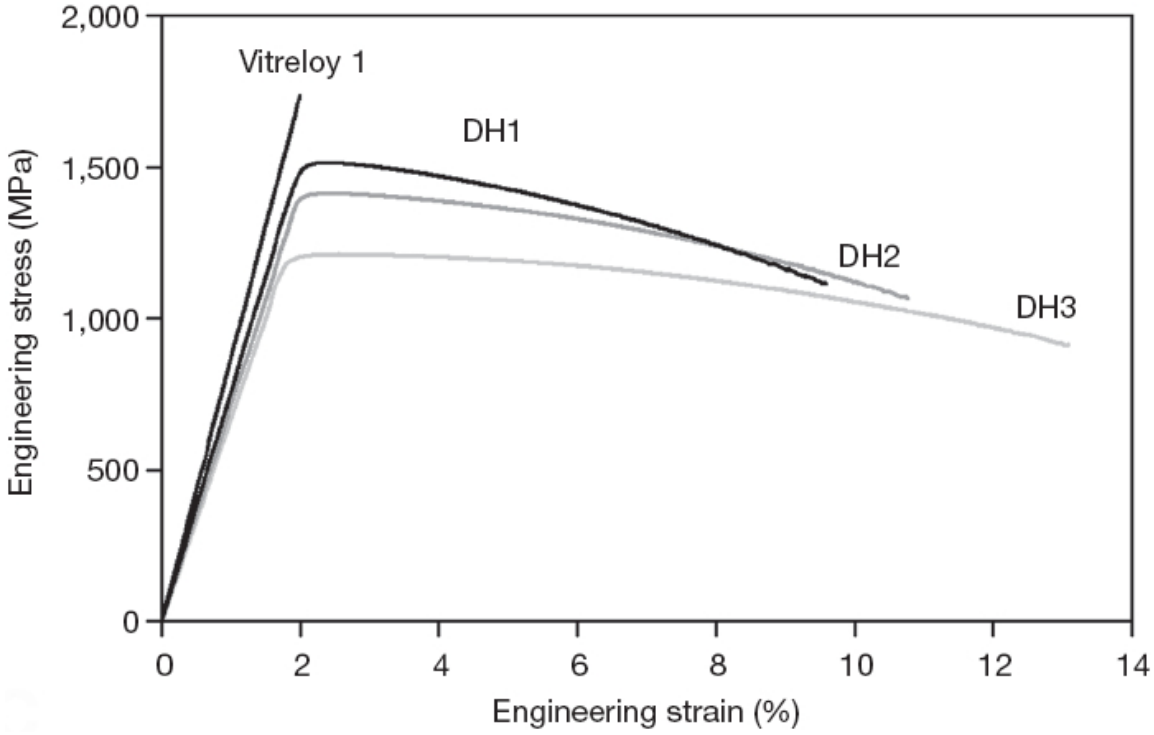

Fig. 5. Engineering stress-strain curves of bulk monolithic metallic glass designated Vitreloy 1 and three bulk glass composites (DH1, DH2, DH3) listed in order of increasing dendrite volume fraction.

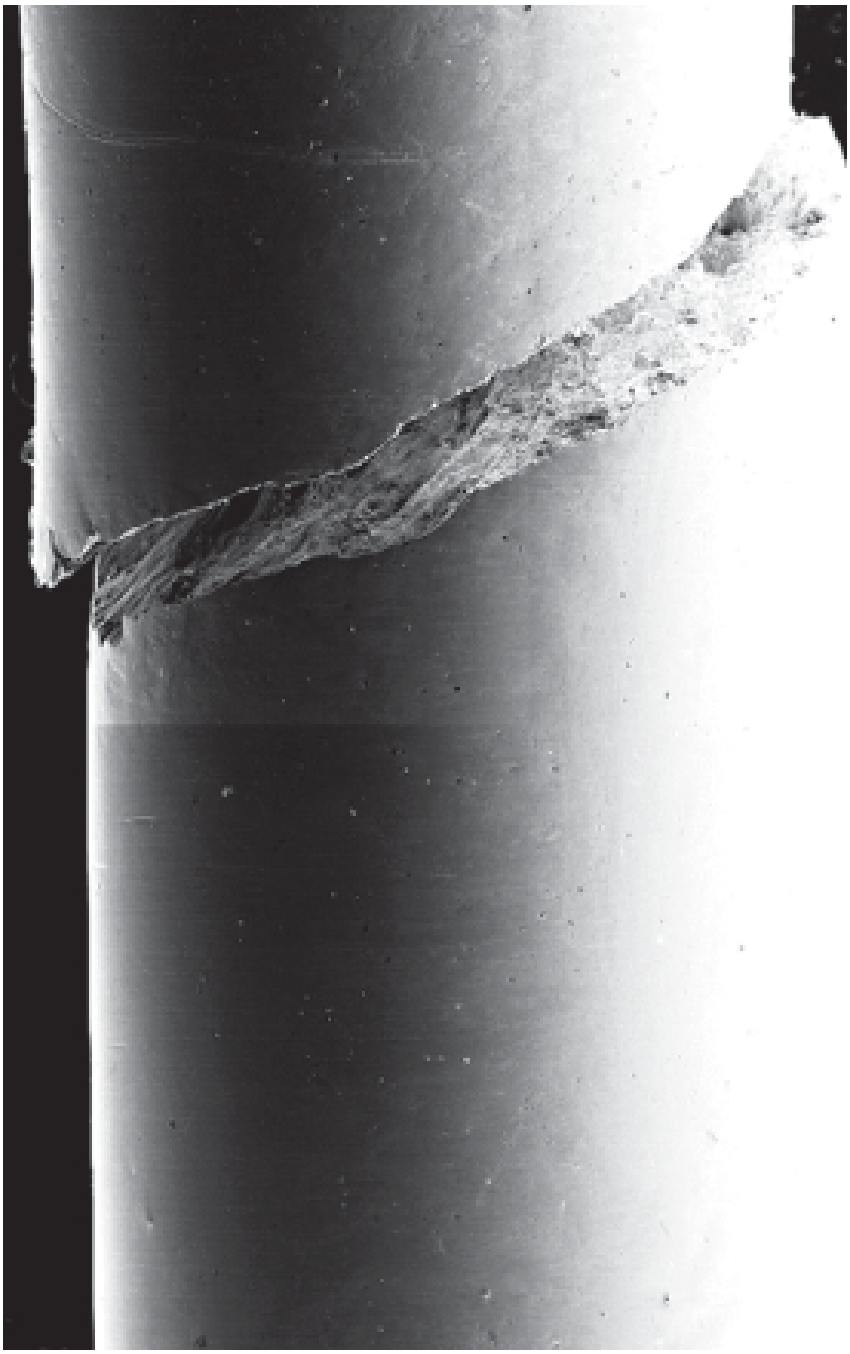

Fig. 6. Scanning electron micrograph of Vitreloy 1 metallic glass specimen after tension test.

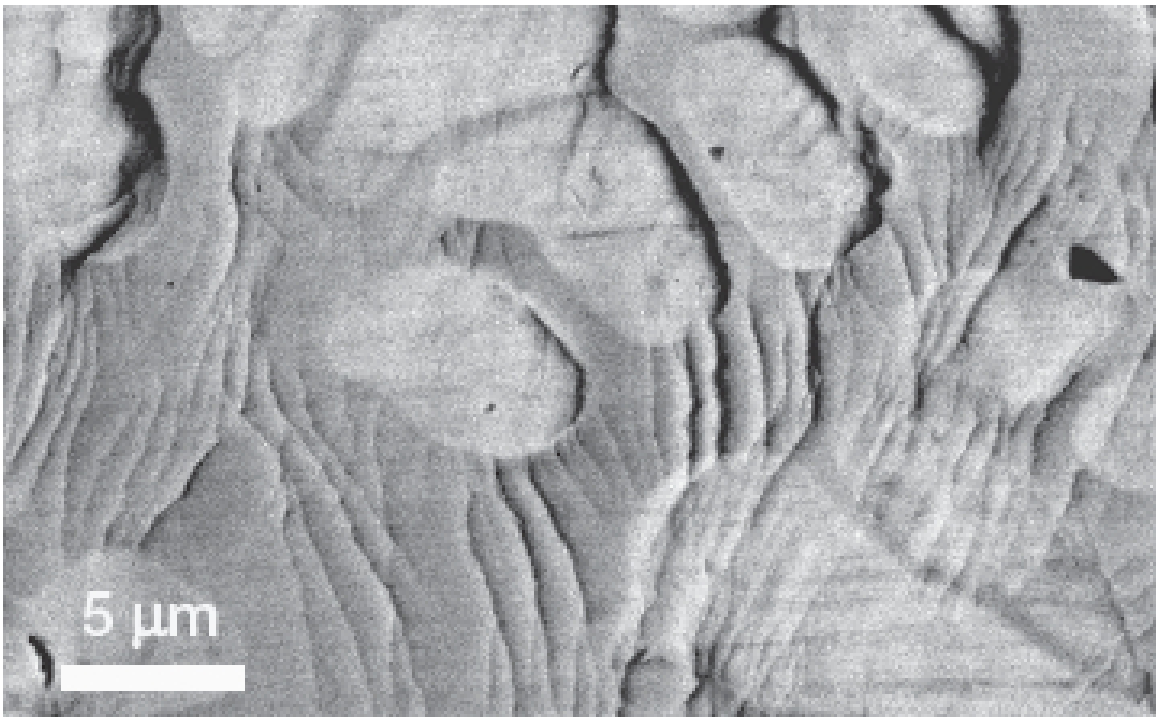

Fig. 7. High-magnification Scanning electron micrograph of metallic glass composite DH3 after tension test.

and 10 nm in diameter (called nanocrystals) homogenously dispersed throughout the volume. A transmission electron micrograph of the as-quenched specimen is shown in Fig. 8. The micrograph does not appear homogeneous but instead a nanocrystalline phase is spread throughout the material with grain diameters of 2 to 10 nm. Based on data from Differential Scanning Calorimetry (not shown), the volume fraction of the glassy phase is calculated to be about 96%, and the remaining 4% is crystalline. Upon analyzing data from X-ray diffraction of the as-quenched rod (not shown), the crystalline phase in the glassy matrix was determined to be CuZr, a direct nucleation from the atoms in the melt. The same information can be implied from the diffraction pattern shown as the inset in Fig. 8. The diffraction pattern shows wide, halo-like rings indicative of the amorphous phase with small dots characteristic of a crystalline phase. The 1.5 mm and 2.5 mm rods were subjected to an engineering stress-strain test and the results are seen in Fig. 9. The 1.5 mm rod yield strength was found to be 1680 MPa and the elongation upon fracture was 10.6%. The 1.5 mm rod with small volume of nanocrystals showed excellent strength with enhanced ductility. The 2.5 mm rod, estimated to be about half glassy and half nanocrystalline, showed very high elongation with lower yield strength but higher fracture strength. Clearly, engineering the microstructure of metallic glass can lead to specific materials behavior. The results show the importance of a dispersion of nanocrystals throughout a glassy amorphous structure.

High strength and reasonable ductility can both be achieved if a metallic glass contains particles of nanometer size. The nanocrystals interact with shear bands formed during deformation leading to more homogeneous strain in the material. Through this, a metallic glass can behave more like a polycrystalline material in terms of ductility while exhibiting higher strength than the polycrystal. However, it is important to note that the crystalline fraction of the composite must not be-

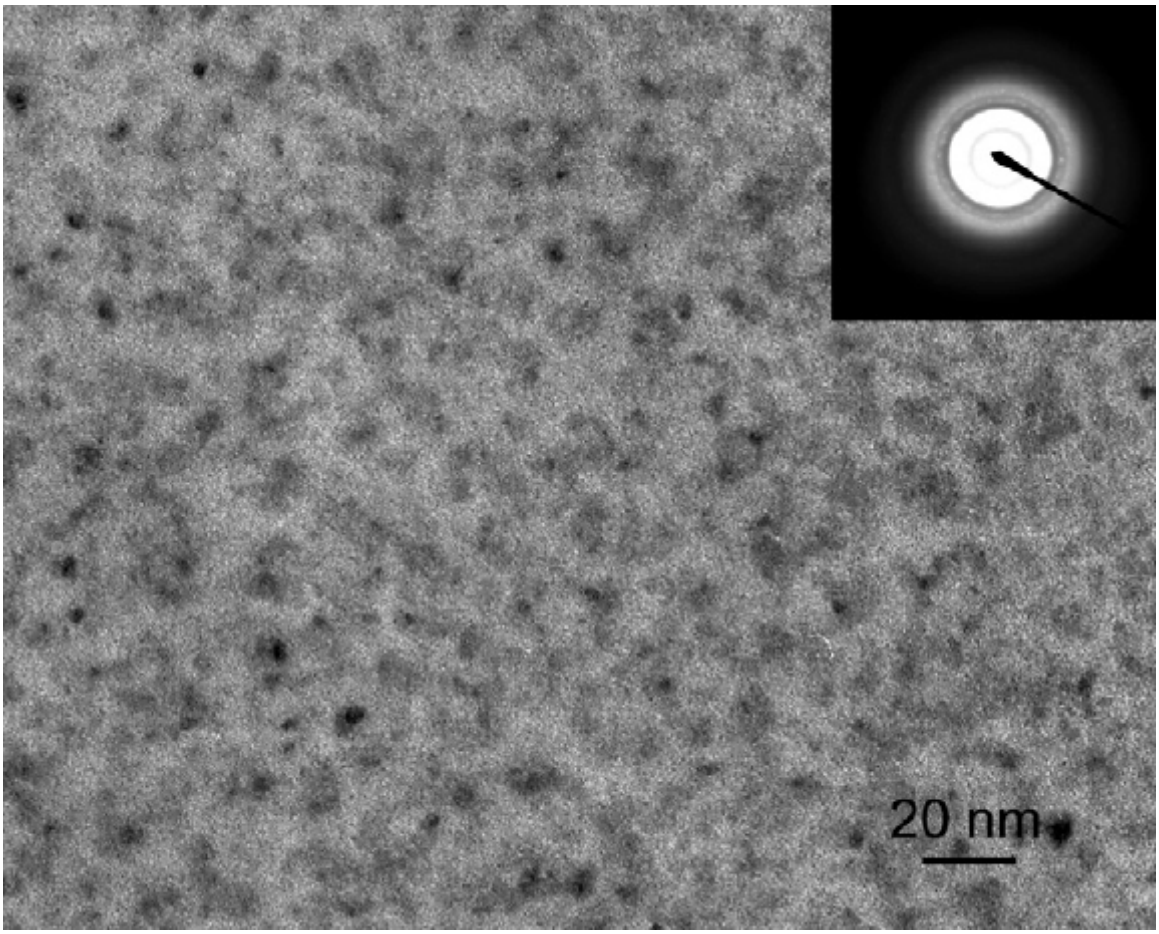

Fig. 8. Transmission electron micrograph of 1.5 mm diameter $Cu_{50}Zr_{45}Ti_5$ rod. Nanocrystals show as dark contrasts. Selected area electron diffraction pattern shown as inset.

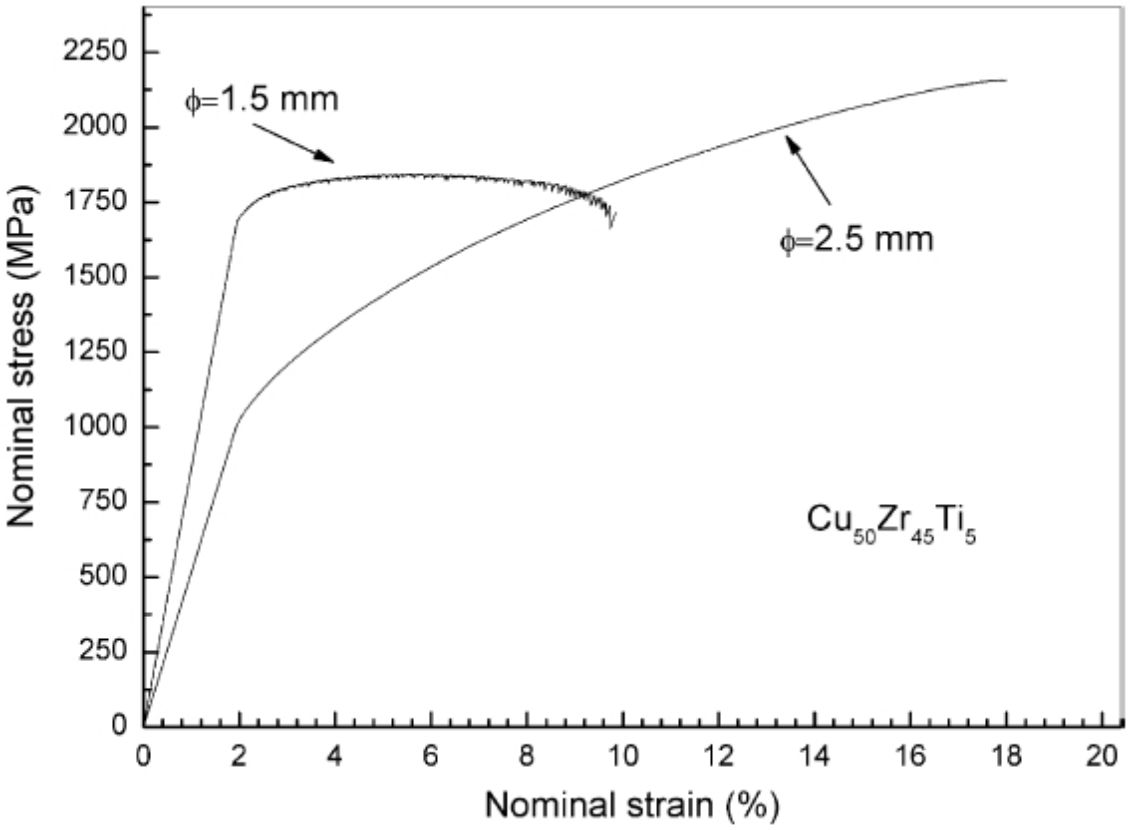

Fig. 9. Engineering stress-strain curves of 1.5 mm and 2.5 mm $Cu_{50}Zr_{45}Ti_5$ rods.

come too great or the system will become largely polycrystalline and the benefits of the amorphous phase will be lost. An example of this was seen in the work of Fan, Takeuchi, and Inoue [27]. In this work, bulk Zr-based metallic glass specimens were annealed to create nanostructure containing precipitated crystalline phases. Mechanical properties were measured with increasing volume fraction of nanocrystals. As seen in Fig. 10, the fracture strength (σ_f) and Young's modulus (E) increases with nanocrystal volume fraction (V_f) up to a point, about 30 - 40%, where a transition occurs, and the curve turns downward. A transition from ductile to brittle fracture mode accompanies the declining material properties. It is apparent that the mechanics of fracture changes once the volume fraction of nanocrystals rises past a certain point. That demonstrates that the nanocrystalization must be controlled, at least in some alloys, so that the benefits of the bulk amorphous nature are not lost.

Other methods exist for forming nanocrystals in metallic glasses, including nanoindentation [28], deformation [29], and bending [30]. The above methods of nanocrystal growth in metallic glasses vary in their effectiveness and one method does not apply to all metallic glasses. It would be desirable to develop a method that can form nanocrystals in any metallic glass. Irradiation of metallic glasses can add energy on an atom by atom basis instead of throughout the whole sample like heat treatments or deformation. Using irradiation, a specimen can achieve some small fraction of nanocrystallization while still remaining mostly amorphous. This finally brings us to the main effort of this dissertation. The goal is to use ion irradiation to form a small fraction of nanocrystals in metallic glass. Ion irradiation in materials is known to bring about phase changes [31] and there have been reports of inducing nanocrystallization in metallic glasses using electron irradiation [32, 33]. Therefore we can expect to see nanocrystal growth as a result of ion irradiation which will aid in future studies to create high strength metallic glasses with enhanced ductility.

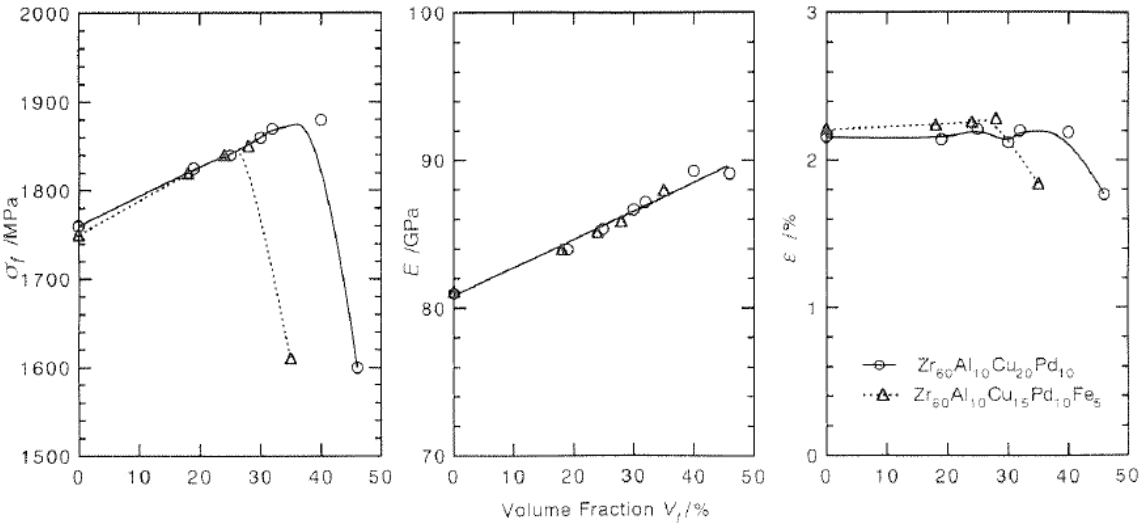

Fig. 10. Fracture strength (σ_f), Young's modulus (E), and elongation (ϵ) for Zr-based metallic glass alloys with increasing volume fraction of precipitated nanocrystalline phase.

Source: [27].

The benefits of ion irradiation over other materials modification techniques is that ion irradiation can manipulate materials on the atomic scale. When ions penetrate a material, the ions interact with individual atoms of the material depositing energy in very small volumes, so an ion can begin the nanocrystal formation process at the desired site. The field of ion irradiation of materials is well developed and the technology exists to use different ions and ion energies such that the energy deposition rate, or stopping power, can be predicted and controlled. Furthermore, the macroscopic size of the irradiation zone can be controlled using ion beam "sweeping" techniques so ion beam modification can occur in both large samples and small samples. For all these reasons, ion irradiation is a very powerful technique which, since it deals with atomic interactions, does not have limitations like other modification techniques and has the potential to work on any metallic glass.

This dissertation will further explore nanocrystal formation in metallic glasses by using a larger range of ion species and energies than ever before. The physics of ion-solid interactions will be discussed which will aid in the understanding of crystal nucleation and growth in an amorphous alloy, but first a discussion of the physics that make room temperature amorphous alloys possible is in order to examine how metallic glasses can be modified. The experiments and discussion in this dissertation link the physics of particle irradiation to nanocrystal formation which will benefit future research in the field.

CHAPTER II

STRUCTURE OF METALLIC GLASS

In order to understand the unique properties of metallic glass, an examination of the amorphous atomic structure is needed. This discussion will include topics regarding the production of metallic glass - an exercise in holding the atoms in place, and the diffusion of metallic glass - allowing the atoms to be mobile. Both mechanisms are important if an amorphous yet partially crystallized alloy is to be produced.

The atomic structure of metallic glass is amorphous - atoms are randomly arranged throughout the material so no long-range order exists, though studies have shown that short-range or nearest neighbor ordering exists [1, 34, 35]. Special considerations must be made to produce a room-temperature amorphous alloy. The atoms themselves do not wish to be random; they prefer to be organized by forming a crystalline structure. A glassy system is said to be metastable and the diffusion mechanisms that govern atomic movement need to be addressed in order to maintain the metastable state or to promote nanocrystallization.

The free energy of the system is minimized when the atoms have periodic structure. As a law of nature, the energy of the system will seek the lowest state, so at temperatures below a metal's or alloy's melting point, the material becomes solid and the atoms try to arrange themselves into some sort of structure. In the case of a metallic alloy, the formation of a glassy alloy is in competition with the formation of a crystalline alloy, commonly called an intermetallic. More specifically, competition exists between the driving force for crystallization (nature) and the low diffusivity that is built in to the system [36]. There are several crystal structures that an alloy may form depending on the temperature and the availability of the constituents. Several intermetallic phases exist for the Cu-Zr binary system [37], for

example, and are shown in Fig. 11. For a relatively simple system consisting of only two elements, several intermetallic compounds can exist, each with their own crystal structure (face-centered cubic, body-centered, etc), and the system gets much more complicated when the number of constituents is increased. Hence, most metallic glasses contain three or more elements. It is clear that there is a driving force to form ordered compounds in alloys which must be suppressed if the material is to be unordered at room temperature.

The arrangement of atoms in metallic glass is not unlike the arrangement in a liquid. In a liquid, the atoms have enough thermal energy to remain unbound. Hence metallic glasses are produced from a liquid mixture. The procedure to form metallic glass is similar to the formation of any metallic alloy. First, the desired proportions of elements are melted together to form a liquid solution. The melt is then cooled below the melting point to form a solid. To form a glass, it is critical at this point to cool the melt so that the atoms remain in the liquid state. In reality, when a melt is cooled, a finite amount of time is required to form ordered structures; the atoms need to go from random to ordered. If the energy of the system is removed before atoms have time to rearrange themselves, then they will be frozen in the amorphous state. Hence, metallic glass production always involves a rapid quenching mechanism to lower the temperature from the melting point to below the glass transition temperature in a sufficiently short amount of time. Rapid quenching effectively "freezes" the atoms in their random state and they remain so at room temperature with proper constituent selection.

The atomic makeup of metallic glasses can be chosen not only to achieve superior strength or hardness, but also to ensure that the cooling rate required is attainable and that the glass will remain stable. For instance, the first room temperature amorphous alloy was discovered by Klement et al. in 1960 [38]. The material was a Si-Au alloy

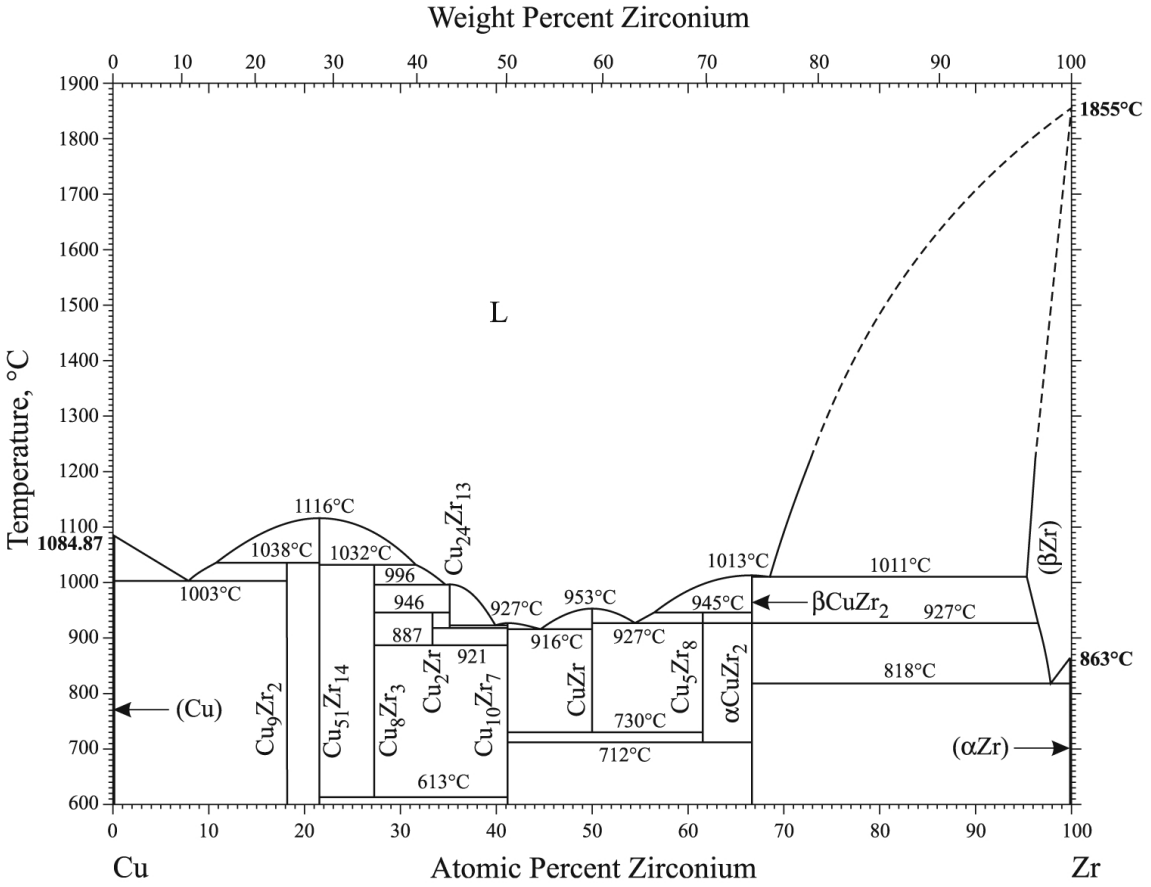

Fig. 11. Binary phase diagram of Cu-Zr system.

With kind permission from Springer Science+Business Media: Journal of Phase Equilibria and Diffusion, Cu-Zr (Copper-Zirconium), volume 29, 2008, page 204, H. Okamoto, figure 1.

and was shown to be amorphous based on X-ray diffraction. The alloy was not stable, however, and further examination as soon as 24 hours later showed complex crystal structures. This primitive, yet important study shows that elements must be chosen such that the diffusivity of atoms in the glass is very low. This leads to what is commonly referred to as Inoue's three empirical rules for stable metallic glasses [1]. The rules govern the selection of components for a metallic glass. The rules say that the constituent elements need to be 1) of more than three kinds, 2) have large atomic size mismatch greater than 12%, and 3) negative heats of mixing. Following these rules will lead to increased dense random packing and ultimately a more stable glass. The Si-Au alloy discussed above does not satisfy these rules and hence is unstable. For this reason, many metallic glasses contain usually four or five (or more) elements.

The critical cooling rate in a given metallic glass will vary depending on the composition and somewhat on the quenching technique. First, a discussion of the thermodynamics of the cooling process is given followed by apparatus used for rapid quenching. Studies involving Vitreloy 1, first processed in the early 1990's [14], will be examined as an example of atomic motion in metallic glasses because a great deal of data exists on the alloy and its low critical cooling rate allows for more thorough examination. As stated above, if the quenching process is not fast enough, crystallization of the liquid melt will occur instead of maintaining the liquid-like structure. By controlling the temperature of a liquid, it is possible to generate time-temperature-transformation (TTT) diagrams. Fig. 12 shows the TTT diagram for the metallic glass alloy Vitreloy 1 represented by data collected through two different cooling methods: electrostatic levitation [39] and processing in high-purity graphite crucibles [40] (the diagram in Fig. 12 is one of the first of its kind since early metallic glasses were too unstable). The symbols represent the time to onset of crystallization (defined as crystal volume fraction of 10^{-4}) at a given temperature. The plot shows a

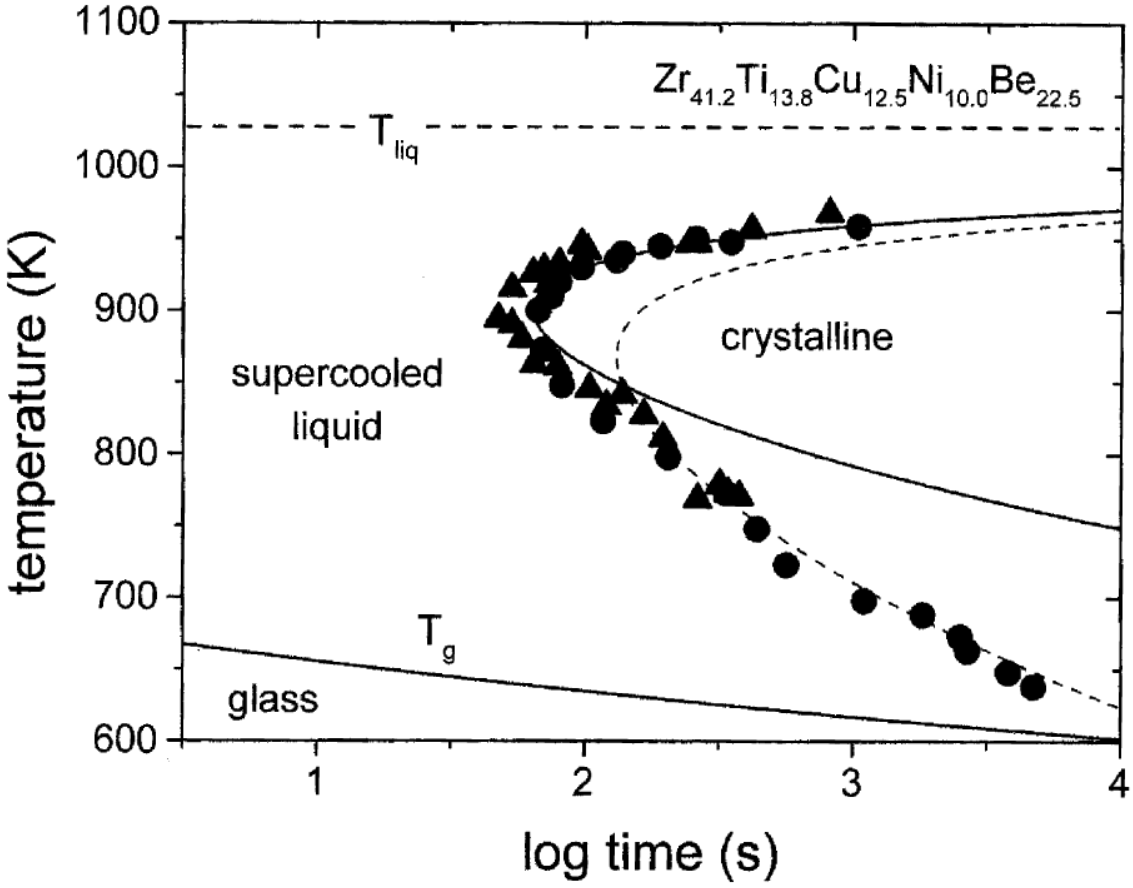

Fig. 12. Time-temperature-transition plot for crystallization of $Zr_{41.2}Ti_{13.8}Cu_{12.5}Ni_{10}Be_{22.5}$. Times are measured by electrostatic levitation (filled $\triangle$) and processing in high-purity carbon crucibles ($\bullet$). Fits to data are proportional to reciprocal of viscosity (solid line) and viscosity $\times$ $\exp(-1/T)$ (dotted line).

typical "C" or nose shape for metallic glasses. Also, the glass transition temperature is shown for given quench times. If a glass is to be fabricated, a time dependent temperature line, starting from the upper left, must be steep enough to reach the glassy region without going through the crystallization region. From this plot, the critical cooling rate was calculated to be about 1 K/s [40], which is several orders of magnitude lower than early metallic glasses [1, 41] including the first Au-Si alloy discussed above. The low critical cooling rate is owed to a very high viscosity for a metallic system.

The nose shape crystallization curve in Fig. 12 graphically shows there are competing factors in the crystallization process of metallic glass such as diffusion and the driving force for crystallization. The diffusion coefficient, which governs atomic mobility, is a function of several factors, including viscosity and temperature. In the TTT diagram, the crystallization time is predicted by calculating the diffusion coefficient by an inverse viscosity relationship (solid line) and Arrhenius-like viscosity $\times \exp(-Q/kT)$ relationship (dashed line). It seems the inverse viscosity fitting holds at high temperatures, while the Arrhenius-like fit holds at lower temperatures. A plot of the measured viscosity in Vitreloy 1 is shown in Fig 13. Note the increased viscosity as temperature decreases, indicating a resistance to movement at lower temperatures. Viscosity taken near the melting point, 1026 K, is 2.5 Pa-s and is much higher, two or three orders of magnitude higher, than other metals at their respective melting points, shown for comparison [40]. The fit through the data is based on the free volume model of glasses and will be discussed later.

Diffusion in metallic glasses is promoted by the preference of the atoms to be crystalline and not amorphous. To be more specific, the driving force can be approximated by the difference in Gibbs free energy between the supercooled liquid and crystalline states, ΔG. The temperature dependence of ΔG in several metallic

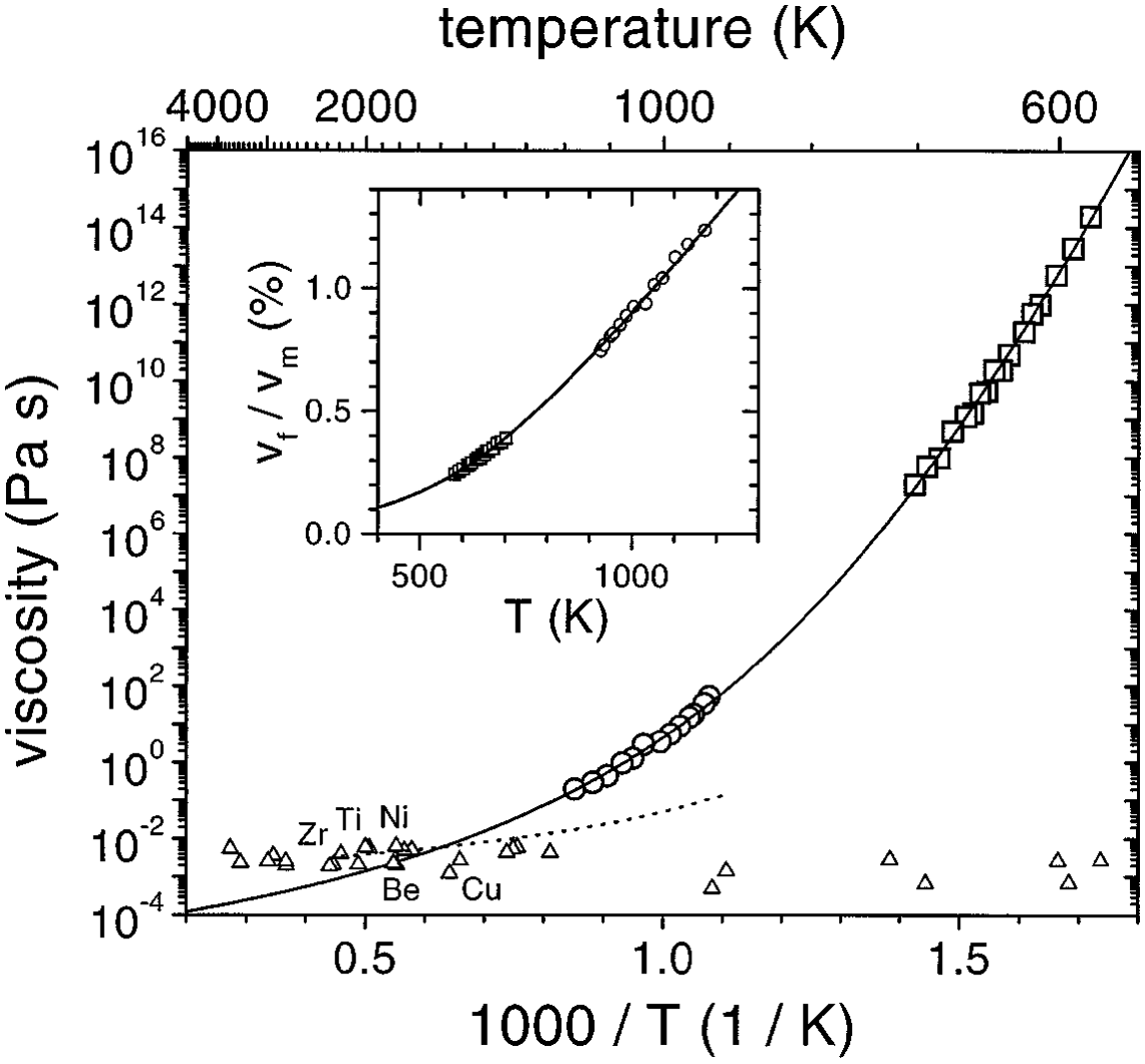

Fig. 13. Experimental viscosity measurements of Vitreloy 1 using beam bending (□) and concentric cylinder viscometry (○). Melt temperature of Vitreloy 1 is 1026 K. Several other melt viscosities are listed for comparison (△), which are, from right to left, Tl, Cd, Pb, Zn, Te, Sb, Mg, Ag, Ac, Au, Cu, Mn, Be, Ni, Co, Fe, Sc, Pd, V, Ti, Pt, Zr, Cr, Rh, B, Ru, Ir, Mo, Os, Re, and W. Dashed line represents extrapolation of Ni viscosity data. Solid line represents numerical fit to Vitreloy 1 viscosity data based on free-volume model. Inset is the free volume of Vitreloy 1.

glass systems is represented in Fig. 14 along with their respective critical cooling rates [36]. The temperature is normalized to the melting temperature of each system. Data was calculated by integrating the specific heat difference between supercooled liquid and crystalline phases taking latent fusion heat into account. The driving force ΔG increases as the temperature decreases, showing the difficulty in maintaining a room temperature amorphous alloy. Some systems have lower energies than others, but all share similar shapes. Notice in Fig. 14 that the critical cooling rate does not decrease with ΔG, though there is some dependence on the critical cooling rate with ΔG. Now we have seen the two competing factors at work in the metastability of metallic glasses. The driving force to crystallize, ΔG, increases as the temperature lowers, but viscosity, the resistance to movement, also increases as temperature lowers. If nanocrystallization is desired in a metallic glass, the resistance to movement must be locally decreased, or similarly, diffusion must be enhanced.

Using logical reasoning, the diffusional mechanisms in metallic glass make sense using Inoue's three empirical rules as a guide. Regarding the size mismatch rule, it is expected that diffusion would be hampered by atoms of different sizes. Smaller atoms can fill the vacancy-like empty regions between the larger atoms. This leads to a more densely packed structure which makes atomic movement much more difficult. Conversely, if the structure is less densely packed, atomic movement should be easier. Hence, the relative ease of diffusion in metallic glasses, or any randomly packed structure, should be governed by the availability of "free volume" present in the as-quenched structure.

This is the reasoning behind the free volume model proposed by Cohen and Turnbull [42] which explains atomic mobility in amorphous structures. The model was later adapted for metallic glasses by Spaepen [43]. Other models have been proposed, such as the "diffusion creep" model [44] but it seems to be inadequate to

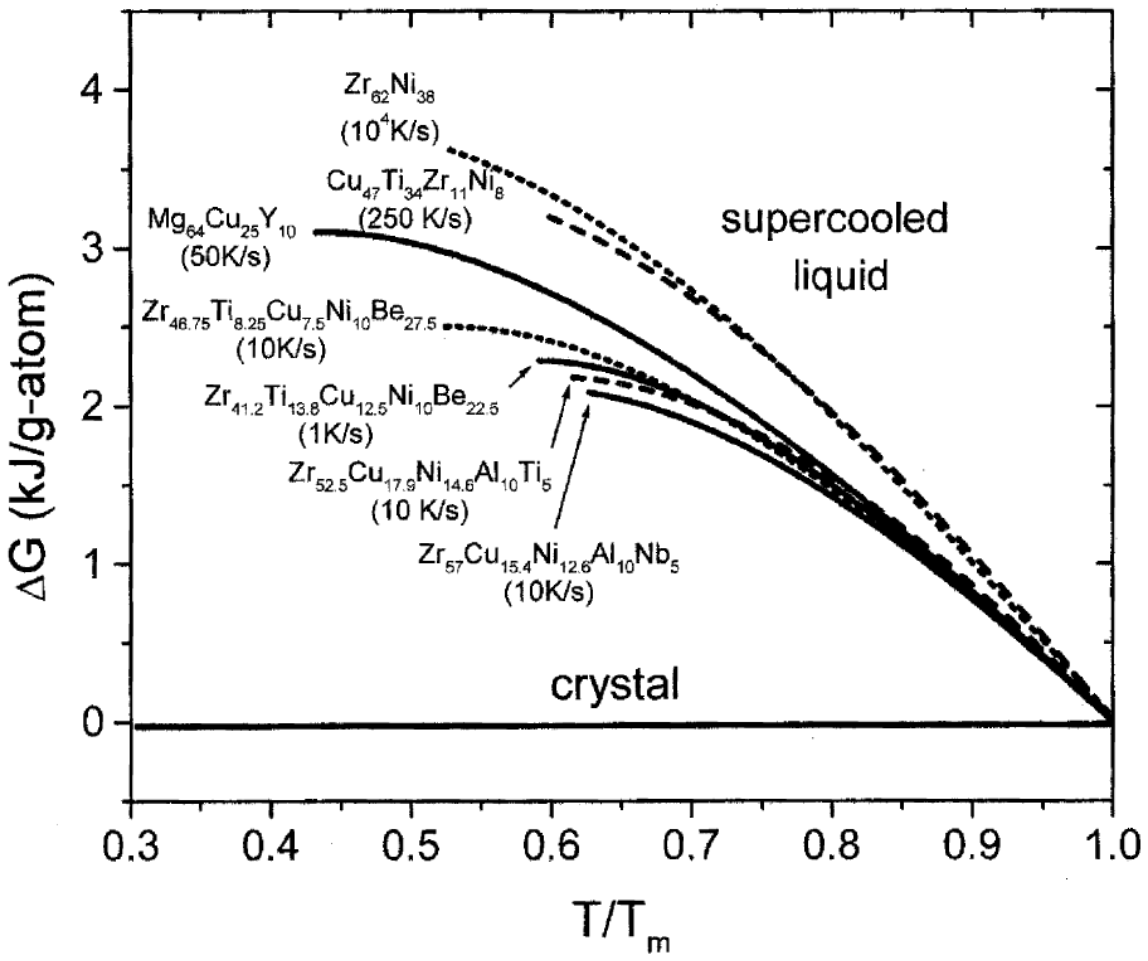

Fig. 14. Difference in Gibbs free energy between subcooled liquid and crystallized states (ΔG) for multiple metallic glass systems. Temperature range normalized to system melting temperature. Critical cooling rates given in parenthesis.

explain the data to which it applies [45]. The free volume model is consistent and based on physical interpretations of an amorphous structure.

In the free volume model proposed by Cohen and Turnbull [42], atomic diffusion and flow are based on atomistic jumping from one site to another. If an atom is to jump, it is reasonable to assume there must be a hole large enough to accommodate it. More specifically, there has to be enough free volume in the structure to allow the hard-sphere volume of a diffusing atom to move. Diffusion coefficients can be based on the probability of finding free volume near an atom that is large enough to contain it. An atom will be bound inside a "cage" defined by neighboring atoms. The free volume of an atom, v, is defined as the volume of the cage around an atom less the atom inside it. There exists a probability p of finding a free volume in a volume between v and $v + dv$ and is calculated to be

$$p(\nu) = \left(\frac{\gamma}{v_f}\right) exp\left(-\frac{\gamma v}{v_f}\right), \tag{2.1}$$

where γ is a numerical factor between 0.5 and 1 to correct for overlaps in free volume, and v_f is the average free volume per molecule. The definition of average free volume in a molecule, v_f, is

$$v_f = V_f/N, \tag{2.2}$$

where V_f is the total free volume and N is the number of atoms at some point in a material. Therefore, v_f is actually a function of position, $\vec{r}$, in the material, but the $\vec{r}$ notation will be dropped for brevity.

Atomic movement is based on finding a hole large enough to move, so there is a minimum critical volume, v^*, that must exist for diffusion. Therefore the total probability P of finding a hole large enough for movement is

$$P(v^*) = \int_{v^*}^{\infty} p(v)dv = \exp\left(-\frac{\gamma v^*}{v_f}\right). \tag{2.3}$$

Spaepen [43] proposed that if an atom is at rest with some local free energy minima, then it needs an activation energy ΔG^m to overcome the barrier and go a distance λ. If the diffusion is a random walk process in three dimensions, the diffusion coefficient is

$$D = \frac{1}{6}\Gamma\lambda^2, \tag{2.4}$$

where Γ is the jump frequency and λ is the jump distance. The jump frequency can be considered the product of two things: 1) the probability that an atom is on a potential jump site, which is deduced from the free volume available and 2) the number of jumps an atom at a jump site makes per second, similar to the atomic vibration frequency ν or Debye frequency. The diffusion coefficient in metallic glass is calculated to be

$$D = \frac{1}{6}\exp\left(-\frac{\gamma v^*}{v_f}\right)\exp\left(-\frac{\Delta G^m}{kT}\right)\nu\lambda^2. \tag{2.5}$$

The key thing in Eq. 2.5 is the $\exp(-v^*/v_f)$ dependency on the diffusion coefficient. Basically, if the free volume, v_f, is increased, there will be an exponential enhancement in diffusivity. For this study, particle irradiation will be used to increase free volume through energetic ion-target collisions.

If diffusivity is increased, atomic mobility can occur. In the presence of ion beam irradiation, additional atomic segregation can occur due to preferential energy transfer to target nuclei. Given sufficient atomic mobility at low temperatures, metallic glass should begin to crystallize because the driving force to crystallization still exists as the free energy of the amorphous state is higher than the crystalline state. If free volume enhancements occur in small areas, as is the case with particle irradiation, small pockets of crystallization can occur. It is this reasoning that is the motivation for using ion irradiation for creating nanocrystals in metallic glass.

If a metallic glass specimen is to be cooled rapidly, the quench rate must be

experienced throughout the entire bulk of the sample. Therefore the maximum quench rate for a given material will be based on the thermal conductivity of the melt, heat transfer between the melt and the cooling apparatus, and also the geometry of the sample. If the metallic glass system of interest has a high critical cooling rate, special care must be taken to achieve that cooling rate throughout the entire specimen. It is for this reason that early metallic glasses were very thin. The first Si-Au amorphous specimen was cast as a thin film [38]. This allows the heat to be dissipated quickly through the thin dimension of the sample and the critical cooling rate is maintained throughout. With the advance of multicomponent metallic glass systems, the critical cooling rate has decreased by orders of magnitude allowing thicker specimens to be created. See Fig. 15 for an illustration of the decreased critical cooling rate and the increased specimen thickness [1]. As critical cooling rates, R_c, of materials decrease, the material can be cast with thickness, $t_{\max}$, of over a millimeter. Now a class of "bulk" metallic glasses is set apart from "conventional" metallic glasses; the bulk glasses have thickness of at least a millimeter. Before the bulk glasses were produced, metallic glasses were often made into thin ribbons.

One technique used to make thin metallic glass ribbon, and the method used to produce ribbons for this dissertation, is called melt-spinning and is characterized by a large spinning wheel on which hot metallic liquid is cooled. This process was patented by Robert Pond in 1961, a Johns Hopkins professor, and is sometimes called the Pond Melt Spinning Process [46]. A schematic is shown in Fig. 16, taken from [47]. High-purity ingots of desired metals are usually melted in an inert atmosphere and then ejected by high pressure onto a continuously spinning chill block. The block is rapidly rotating, chilled, and highly thermally conductive. Ribbons produced by this technique and small and thin, typically a few millimeters wide and 20 microns thick [33], but can be very long, so the throughput is still high. The quench rate of

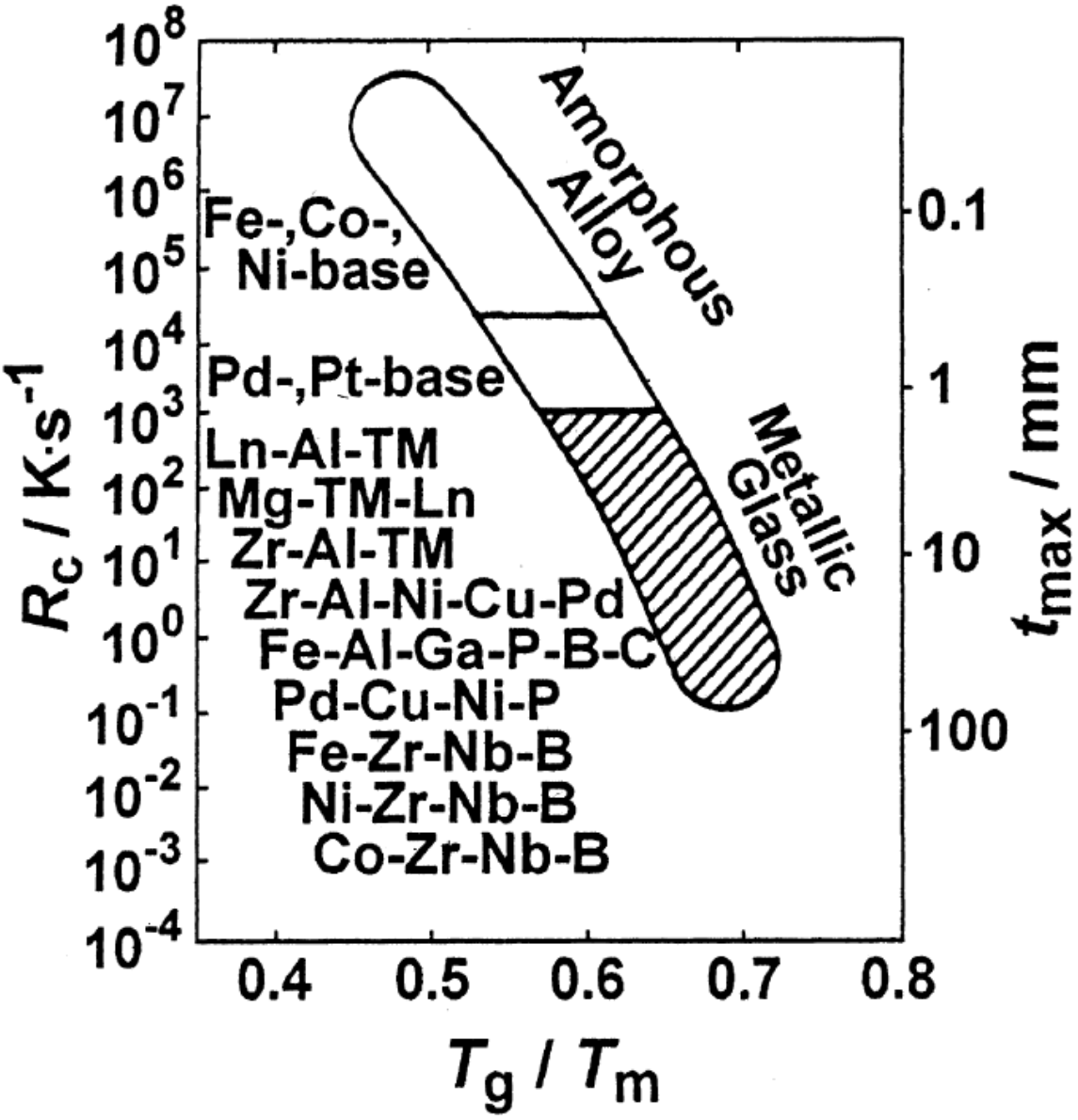

Fig. 15. Critical cooling rates and maximum specimen thickness for many metallic glasses plotted against reduced glass transition temperature.

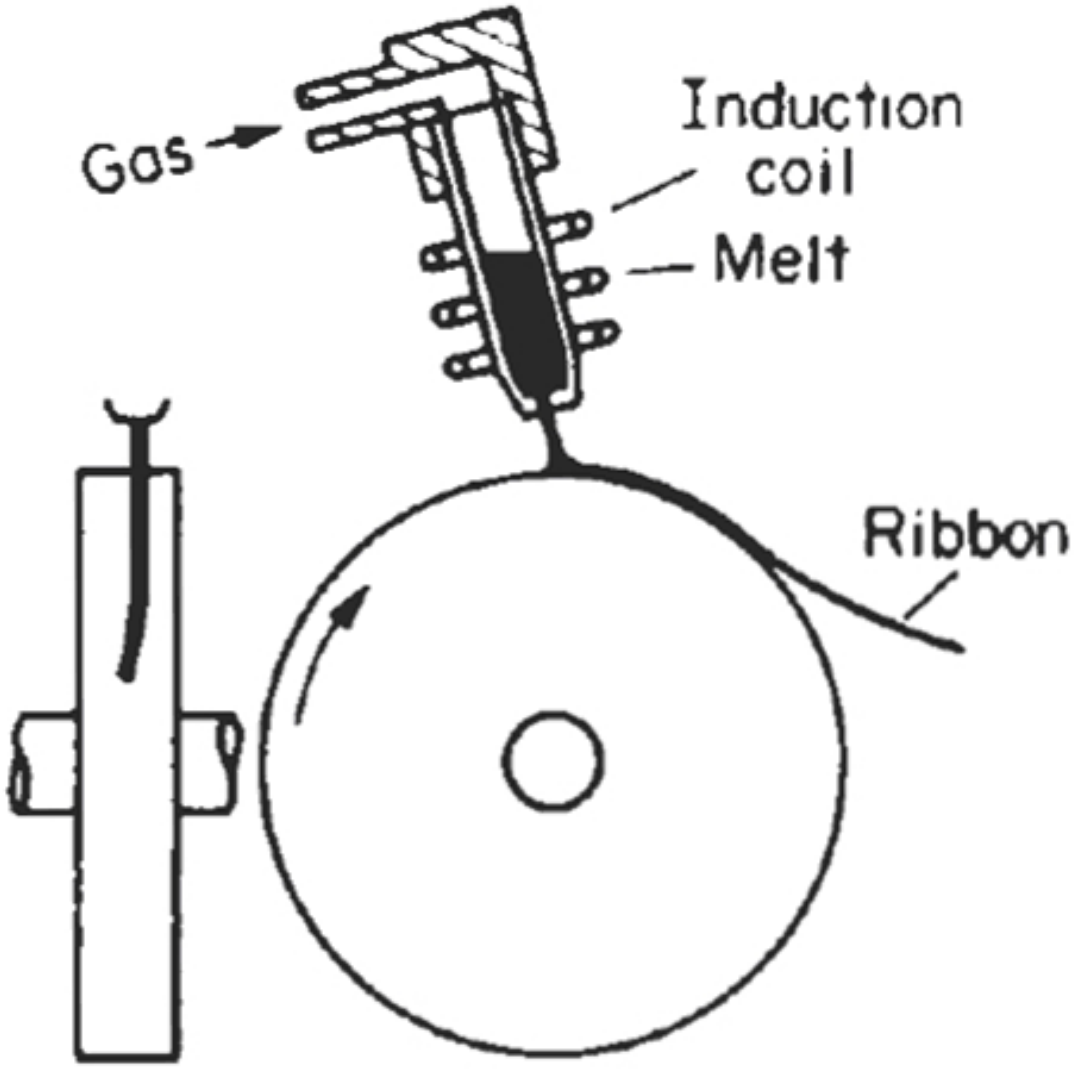

Fig. 16. Schematic representation of melt-spinning metallic glass production technique.

this technique has been measured using multiple metals was determined to be 10^6 K/s on average [46].

Experimentation in this dissertation will focus primarily on two different metallic glass systems: "MG1" - $Cu_{50}Zr_{45}Ti_5$ and "MG2" - $Zr_{55}Cu_{30}Al_{10}Ni_5$ (atomic percentages). Both metallic glasses were formed by melt spinning and in their unchanged, "as-spun" form are small ribbons about 1.5 mm across and about 20 microns thick. The radiation tolerance of the two materials will shown to be different, most likely owing to the fact that MG2 has a more complex structure with more elements and greater thermal stability. Also, the addition of minor elements in MG2 can lead to different nanocrystal sizes and densities in irradiated specimens. The physics of ion-solid interactions will be discussed in the next chapter and will show how the energy barrier to crystallization can be overcome in small volumes, resulting in nanocrystallized metallic glasses.

CHAPTER III

ION-SOLID INTERACTIONS

This chapter will discuss the physics of ion-solid interactions in order to explain how ion beam irradiation of metallic glasses enhances the free volume as discussed in the previous chapter. This is necessary because different ion irradiation conditions will result in different atomic displacement scenarios. The physics of ion-solid interactions must be known in order to estimate atomic displacements and predict free volume changes in the material.

The field of ion irradiation is very robust and many applications have been developed that involve the process. When ions are imbedded in a material, it is commonly called ion implantation. This can be used for a variety of applications that require small modification to the material, whether it be changes to the microstructure or composition. Semiconductor fabrication, for example, requires a small amount of dopant, commonly group III or V elements, to be implanted in Si to change the electrical properties. This can be done by ion implantation. Another field using ion irradiation is materials analysis. Passing high energy particles through a material can give some insight as to the composition and structure of a material. Transmission Electron Microscopy relies on this in order to "see" inside a thin membrane. Another application using ion beam analysis is Rutherford Backscattering Spectrometry. High energy, light ions are incident on a target and the backscatters are counted and analyzed, indicating the material's composition, damage, impurities, etc. The main application here though will be ion beam modification of materials. It is this method that is used to create nanocrystals in metallic glasses.

In typical ion irradiation applications, ions are accelerated through an electric potential to a certain kinetic energy and aimed at a target for a strict amount of

time. A typical ion irradiation device consists of an ion source, acceleration column, mass separator magnet, and a target chamber. Commonly, electrostatic or magnetic "lenses" are used to focus the beam to a desired size and beam sweepers are used to automatically move the beam over a large area. A schematic of such an irradiation system can be seen in Fig. 17 from [48]. When the beam reaches the target chamber, it is comprised of roughly parallel streams of ions of the same species and same speed. Beam intensity is usually measured in units of amperes per square centimeter (A/cm^2). Typical beam intensities range from 10^{-6} – 10^{-4} A/cm^2. Not shown in the figure is a system of pumps that maintain a near-vacuum inside the system to minimize collisions before reaching a target.

Instead of selecting the speed of the ions as they traverse the irradiation system, it is typically easier and more beneficial to select the kinetic energy, commonly referred to as just energy, of the ions. The ion charge state and accelerating column potential are selected to achieve desired ion energy. The typical unit of ion energy is the electron-volt (eV), defined as the kinetic energy achieved when a particle with the charge of one electron is accelerated through a potential of one volt. The SI unit of charge is the coulomb (C) and the charge of an electron is 1.602×10^{-19} C. The SI unit of energy is not the electron-volt but the Joule (J) and in the same manner can be described as a coulomb-volt. Therefore a conversion exists between the two units of energy: 1 eV = 1.602×10^{-19} J. The velocity, v, of the ion can be determined from the kinetic energy, E, simply by $E = \frac{1}{2}mv^2$, where m is the mass of the ion. Ion energy is commonly much greater than an eV so the kilo-electron-volt (1 keV = 10^3 eV) and mega-electron-volt (1 MeV = 10^6 eV) are often used. For example, a particle can be accelerated to 1 MeV by passing an ion with the change of one electron through a potential of 1 megavolt. Notice the mass is not used in the previous calculation, so multiple ion species can be accelerated to the same energy with the same setup.

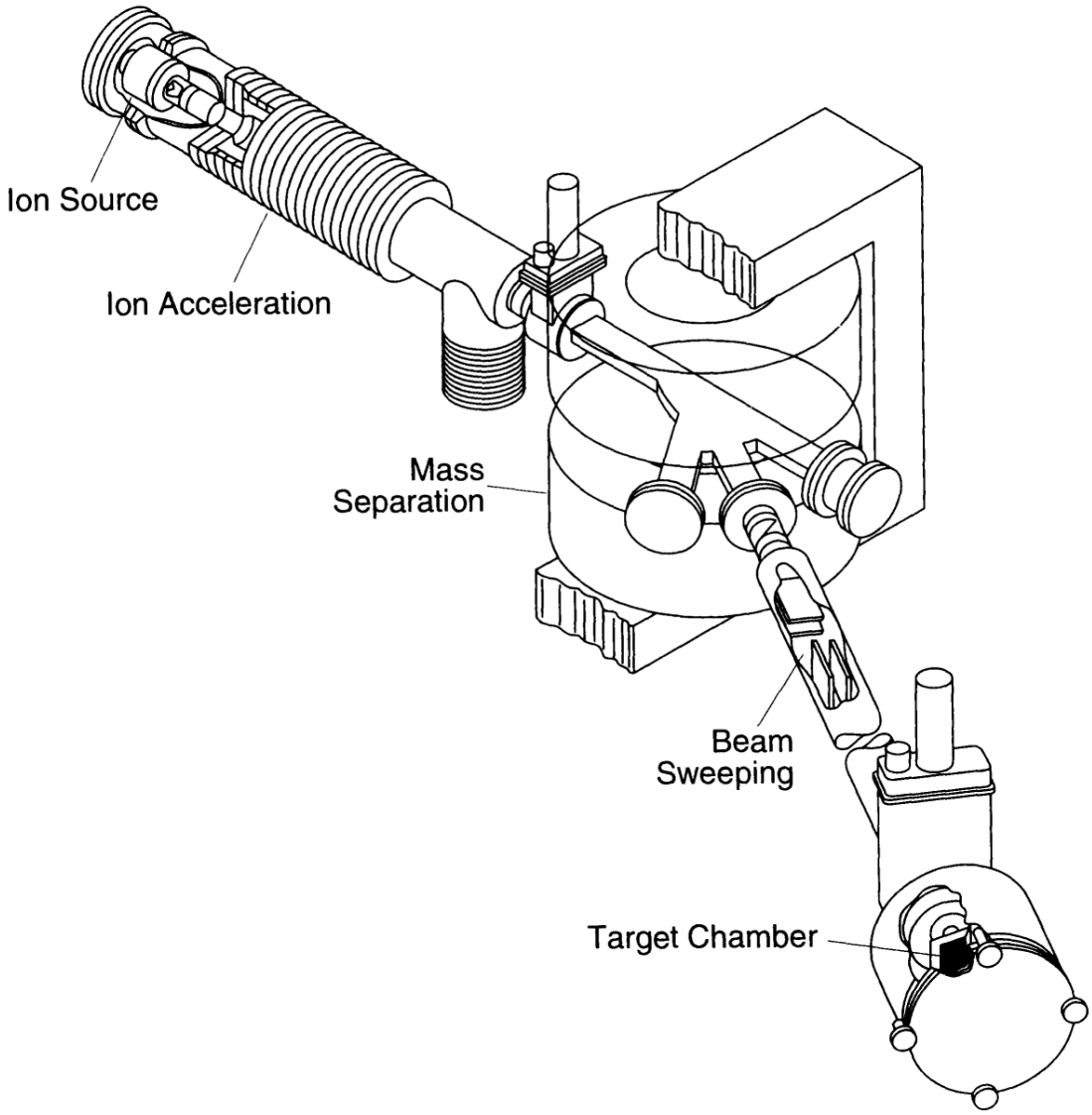

Fig. 17. Schematic of typical ion irradiation system components.

The quantity of ions implanted into a sample is typically called dose or fluence and is normalized per unit area. The term 'fluence' will primarily used in this paper in order to avoid confusion with the term 'dose' commonly used in nuclear engineering to describe the energy deposited per unit mass. Fluence is defined as the number of ions per square centimeter implanted in the sample and is commonly measured as the time-integrated beam intensity or time-integrated flux. The flux is a derivative of beam intensity using the conversion from amperes to ions per second: 1 A = 1 C/s = $(1.602 \times 10^{-19} \times n)^{-1}$ ion/s, where n is the charge state of the ion. As an example, if the beam intensity is 10^{-6} A/cm^2, and the ion is doubly charged, the flux is roughly 3.1×10^{12} ion/cm^2 – s and a 1 minute irradiation would result in a specimen fluence of about 1.9×10^{14} ion/cm^2. Typical implantation values can range form $10^{14} - 10^{17}$ ion/cm^2.

When an energetic ion enters a target material of many atoms, it starts slowing down through collisions with target atoms - a process known as stopping. Stopping can be characterized by two interactions: interactions with target electrons and interactions with target nuclei, respectively called electronic stopping and nuclear stopping. The contribution from each stopping process is a function of collision parameters such as the mass of projectile and target atom, atomic number (or charge) of projectile and target atom, and ion velocity. Nuclear stopping is dominant at low projectile speeds and electronic stopping dominates at high velocities. This relationship is depicted in Fig. 18. The actual values for the respective stopping powers depend on the parameters of the collision and have been extensively studied and tabulated [49]. The nuclear stopping process is the dominant process for atomic displacement in a material and each individual stopping process will be discussed later.

In a single ion's track through a material, target atoms create obstacles and several collisions take place. The distances between collisions as well as the energy

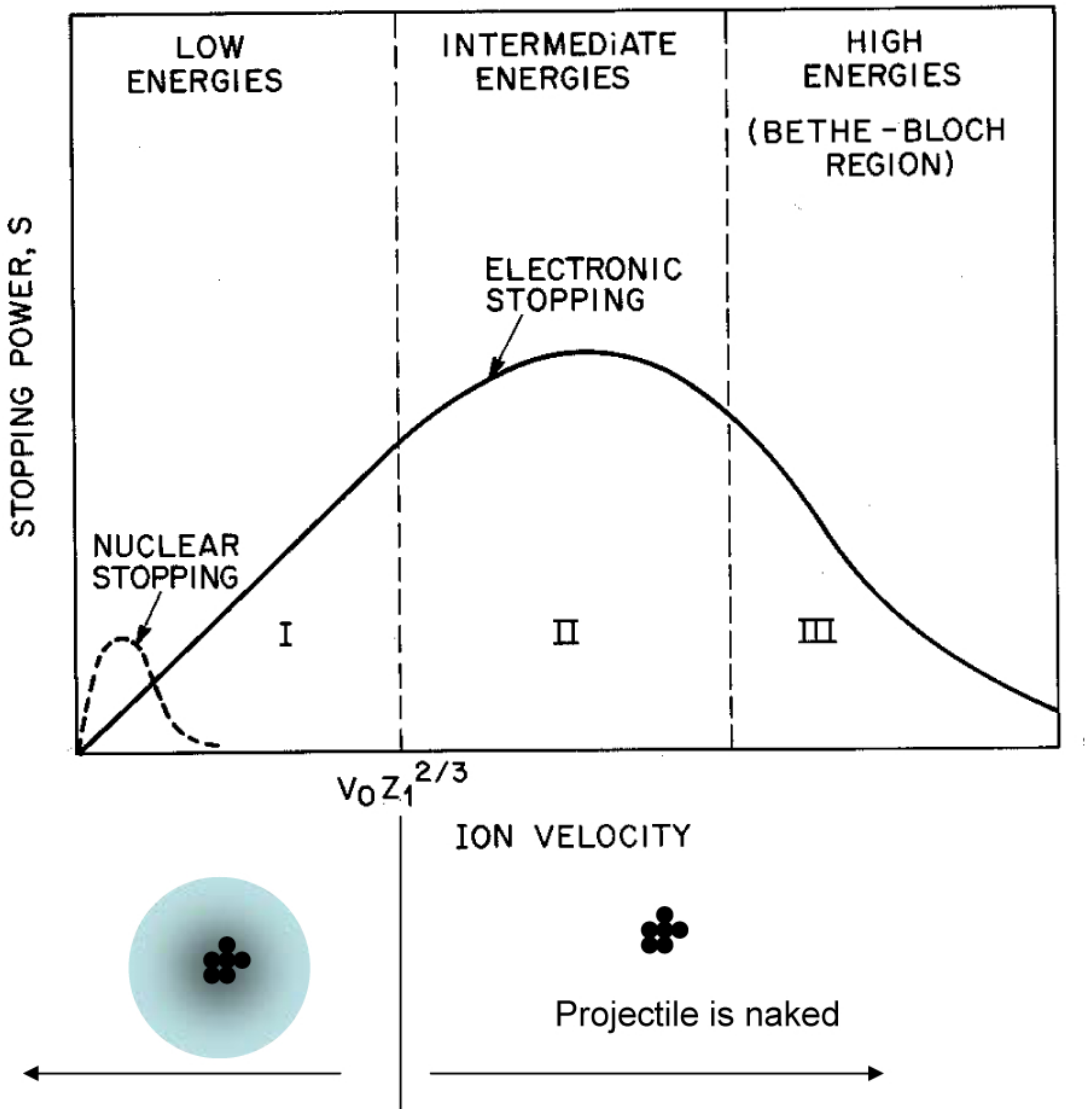

Fig. 18. Relative contributions of electronic and nuclear stopping powers plotted against ion velocity. Above a threshold velocity $v \approx v_0 Z_1^{2/3}$, where v_0 is Bohr's velocity and Z_1 is the atomic number of the projectile, the projectile is stripped of electrons. Below the threshold velocity, the projectile retains part or all of its electrons.

lost in a collision are random processes. Therefore, when crystallography is not an issue, the ion travels in a tortuous path and the ion track length is not always the same. Instead, the perpendicular distance from the target surface is measured and used as the definition for the projected range, R_p, of the ion. The distribution of R_p after several ion tracks is known as the range distribution and, for moderate ion energies, has a Gaussian shape. Therefore another term, called range straggling, dR_p, is often used to characterize the spread in the range distribution. The range and straggling depend on the many parameters in the stopping process, as described above. The projected range of ions in a material can range from angstroms for low energy ions, and millimeters for high energy, light ions. As an example of varying parameters in ion irradiation, Fig. 19 shows the difference in range distribution profiles when an incident ion mass, M_1 is (a) less than target atoms ($M_1 < M_2$) and (b) greater than target atoms ($M_1 > M_2$) [48]. The ranges, straggling, and overall shapes of the curves are different for the two cases. The physics of stopping has been studied well enough that the range and straggling of ions in matter can be very well predicted for most ions and target materials. The range of ions in solids will be very important later because the range of ions gives an approximation of the depth of atomic displacements and nanocrystal formation.

It is customary to divide energy loss along an ion's track into two components: electronic stopping and nuclear stopping. Electronic stopping deals with interactions between the electrons of ion and target material and is typically considered to be inelastic. Nuclear stopping involves energy transfer from a projectile to a target atom as a whole and is considered to be elastic. Nuclear stopping usually involves discrete, sizeable energy losses through large deflection angles while electronic stopping is a more continuous process involving many small energy losses per interaction with negligible deflection. Electronic and nuclear stopping are conveniently divided between

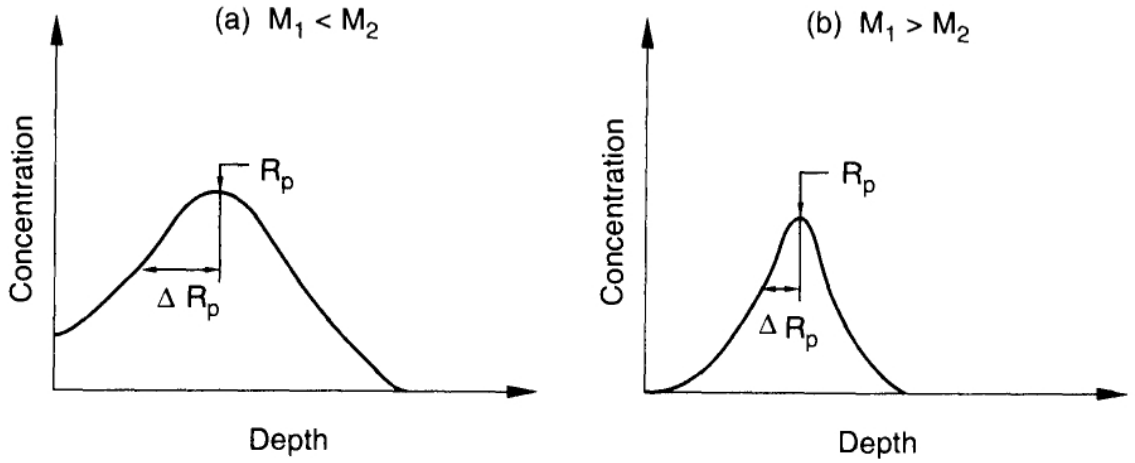

Fig. 19. Histograms representing the mean projected range, R_p, of an ion in a material, and the range straggling, dR_p, about the mean for two different scenarios, (a) projectile mass less than target atom mass ($M_1 < M_2$) and (b) projectile mass greater than target atom mass $M_1 > M_2$).

inelastic and elastic collisions, respectively, and while this is not exact, it provides a good approximation.

Ion stopping is a function of many parameters, including ion velocity, ion mass, ion charge, and target material. Ions are said to slow down through many collisions resulting in a net energy loss per length traveled. The energy loss per unit length is typically called stopping power and is denoted as

$$\frac{dE}{dx} = \left.\frac{dE}{dx}\right|_n + \left.\frac{dE}{dx}\right|_e , \tag{3.1}$$

where the stopping power, dE/dx, has been broken up into its nuclear and electronic components, respectively. Note that dE/dx is a negative quantity, since energy is lost by the ion, and the negative sign is commonly omitted. A typical unit for stopping power is electron-volts per angstrom (eV/A). While stopping powers are known to vary when an ion track is parallel to a target's crystal planes, this difference will not be considered because the target material being dealt with here is amorphous and does not contain crystal planes. The physical processes of stopping need to be discussed because the ion-beam modification of a material is dictated by the energy transfer process between target atoms and the projectile.

At high ion velocities, electronic stopping becomes dominant, as demonstrated in Fig. 18. In this mode, an ion loses energy through inelastic collisions with electrons primarily through target electron excitation and ionization. At sufficiently high velocities, the ion becomes completely stripped of its electrons and can be viewed as a single moving point charge moving at speeds greater than the mean orbital velocities of the target atoms. Therefore the velocity at which an ion becomes stripped of its electrons is proportional to the Bohr velocity, the velocity of an innermost electron of a hydrogen atom, which is about 2.2×10^6 m/s, or approximately 1% the speed of light. For light ions (H, He), Bohr suggested the effective ion charge fraction is

equal to $v/v_0 Z^{2/3}$, where v and Z are the velocity and atomic number, respectively, of the projectile. If the effective ion charge reaches approximately 1, then the ion is fully stripped, and if 0, the ion carries all its atoms and is neutralized. Therefore, $v_0 Z^{2/3}$ is the approximate velocity at which an ion is stripped of its electrons and used as a guide to separate different electronic stopping regimes. For heavy ions, the effective ion charge has been experimentally determined to follow the expression $1-\exp\left(-0.92v/\left(v_0 Z^{2/3}\right)\right)$. For light ions, He for example, the ion can become stripped at reasonable energies, approximately 250 keV, but for heavy ions, much more energy is needed. For instance, a Cu ion needs upwards of 2 GeV of kinetic energy to become fully stripped (more specifically, an effective ion charge fraction greater than $(Z-1)/Z$, where less than 1 electron remains). The stopping power is calculated as the energy transferred to an electron as the projectile passes. The interactions are regarded as purely coulombic. The maximum energy transfer in this case would be if the projectile collides with the electron head-on, but the minimum energy transfer depends on the energy levels of the orbital electrons in the target material. It is clear from the mechanism described above that the high-speed electronic stopping process, while very effective at high energies, is not responsible for target atom displacement.

As an ion slows, it starts to pick up electrons and becomes partially neutralized. At the velocity $v < v_0 Z^{2/3}$, the ion is traveling slower than most electrons of the target material, but not all. The loss mechanism for electronic stopping in this regime is not well-defined as is the high-velocity case, and multiple models have been proposed. One model, proposed by Firsov [50] states that if the projectile picks up an electron, then momentum is transferred to the electron in order to accelerate it to velocity v, thereby adding to the stopping process by taking energy away from the projectile. In fact, when the projectile comes close enough to a target atom, a short-term quasi-molecule is formed and electrons are shared. This idea is depicted in Fig. 20, showing the

projectile moving in the x direction with velocity v and separated in the y direction by a distance b, the impact parameter. The two zones of the quasi-molecule are called the P-zone (for the projectile) and T-zone (for the target material) and are separated by the Firsov plane. The energy transfer process in Firsov model involves determining the energy needed to pick up the electrons from target atoms by moving through the Firsov plane. This process again only involves the electrons of the target material and does not contribute to target atomic displacement.

The nuclear stopping process is the last stopping process to discuss. At low ion velocities, collisions between projectile ions and target atoms involve the deflection of the atom as a whole, not the individual electrons as described by the electronic stopping process. The collisions are considered to be elastic and a discrete energy loss process takes place in the form of a two-body problem; the distance between collisions is great and the projectile deflection angle is often very large. In this form of a binary collision, depicted in Fig. 21, the target atom is practically at rest and the fast-moving projectile can impart enough energy to eject the target atom as a whole from its location. In reality, at such low energies, the energy transferred is a result of the coulumbic force between two nuclei as they come into near proximity of each other, so a more accurate depiction of collision trajectories is presented in Fig. 22. The particles are spaced by the impact parameter, b, and the only force that exists between the two is from the coulumbic potential acting along r, the separation distance between the two masses. Solving for the final parameters after the collision usually involves a transformation to the center-of-mass coordinate system. However, the maximum energy transfer from projectile to target atom, E_{max}, can be easily calculated by assuming a head-on collision with $b = 0$ and $\theta = 180°$:

$$E_{max} = \frac{4m_1m_2}{(m_1^2 + m_2^2)}E, \tag{3.2}$$

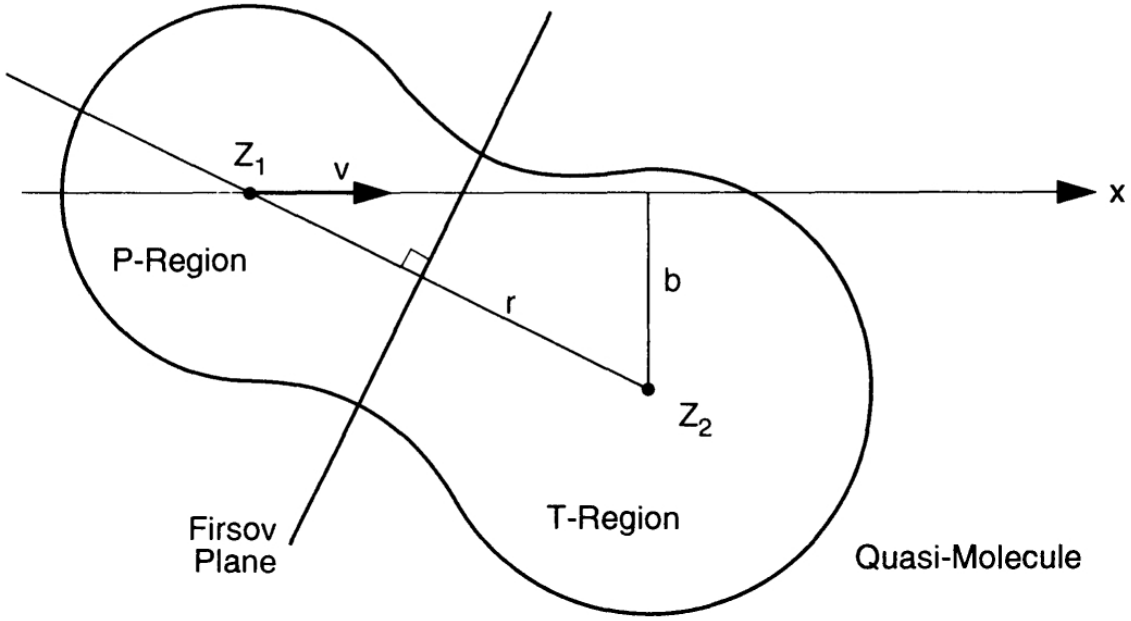

Fig. 20. Quasi-molecule proposed by Firsov when projectile ion and target atom come in close proximity.

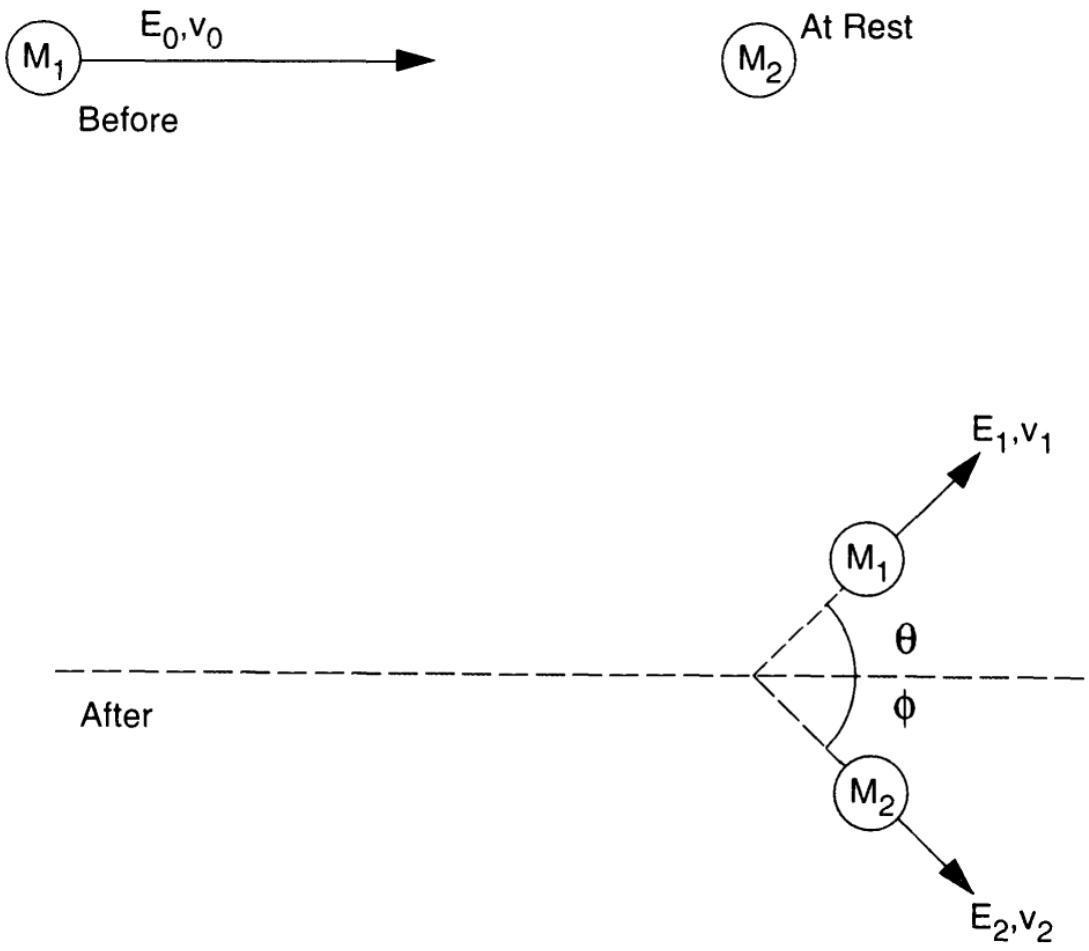

Fig. 21. Schematic of two-body elastic scattering problem as used to describe the nuclear stopping process. Subscripts 1 and 2 represent projectile and target atom, respectively. Before collision, projectile has energy E and velocity v, and imparts some energy and momentum to the target atom through an elastic collision, which scatters the particles at different angles θ and ϕ, respectively.

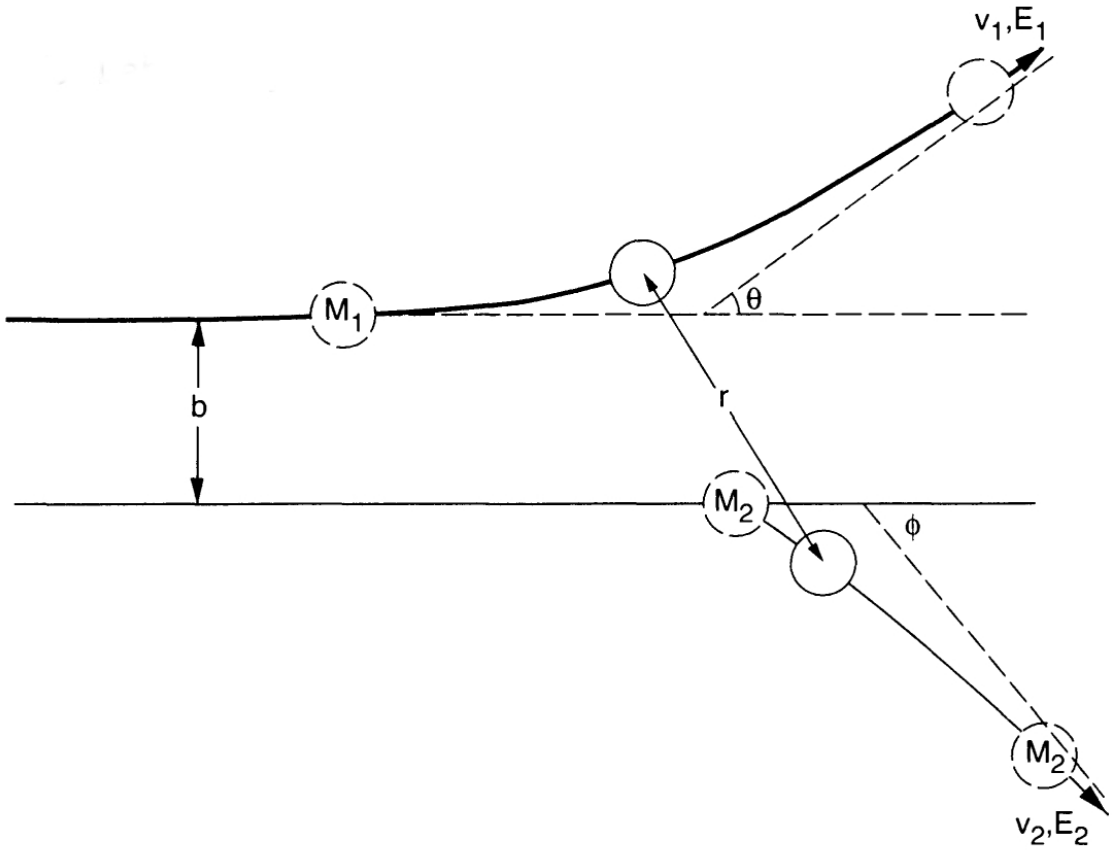

Fig. 22. Collision trajectories for elastic ion-target interaction with impact parameter b and spacing r.

where E is the energy of the projectile and m_1 and m_2 are the masses of the projectile and target atoms, respectively. It is clear that the nuclear stopping process is the primary mechanism causing atomic displacements.

A minimum amount of energy must be imparted to the target atom to displace it from its resting location because the target atom is bound to the atoms around it and sits in a potential well. The depth of the potential well is called the displacement energy. The arrangement of atoms in a solid represents some local minima of free energy and any deviation from such an arrangement will require an addition of energy. Therefore if an atom is to be displaced from its site, it will require an addition of some threshold energy to become mobile. If the energy transferred to the target atom in a collision is less than the displacement energy, the target atom will undergo vibrations without leaving its site and quickly dissipate the energy through neighboring atoms. If the transferred energy is larger than the displacement energy, then the atom is free to leave the site. An atom that leaves its site is called a primary knock-on atom (PKA) and may go on to displace other atoms from their respective sites. Such subsequent displacements are called a damage cascade and may involve a few to hundreds of atoms. The displacement energy in a material is largely a function of direction. This is especially true in a metallic glass where the interatomic spacings are different in practically every direction since the atoms are arranged randomly. The displacement energy will also vary from one type of metallic glass to the next because the atomic spacings will be different due to different atomic size ratios and varying degrees of packing.

A simple theory was proposed by Kinchin and Pease [51] which estimates the average number of displaced atoms as a function of a PKA with energy T. The original model neglected crystal structure for simplicity and assumed the arrangement of atoms in the solid was random. This assumption was made to use a single value

for the displacement energy, E_d, which is averaged over the range of possible values in the solid. In this model, an atom is displaced if it receives energy $T > E_d$. The target atom then becomes mobile and is considered a PKA and is free to create more displacements. The atom cannot become mobile if $T < E_d$. If the PKA has energy $E_d < T < 2E_d$, the atom can only cause one more displacement since it has insufficient energy to create two displacements. There exists some cutoff $T = E_c$ because at high T, electronic stopping is dominant, and no significant atomic collisions occur until T is lowered to E_c. For the energy range $2E_d < T < E_c$, it can be shown that the average recoil energy produced by PKA with energy T, is $T/2$. Since E_d is the minimum energy needed to produce a displacement, the average number of displacements created by PKA with energy T is $(T/2)/E_d$, or $T/(2E_d)$. The Kinchin and Pease model can be summed up as:

$$\text{average number of displacements} = \begin{cases} 0, & T < E_d \\ 1, & E_d < T < 2E_d \\ \dfrac{T}{2E_d}, & 2E_d < T < E_c \\ \dfrac{E_c}{2E_d}, & T \geq E_c \end{cases} \tag{3.3}$$

The damage cascade created from primary and secondary knock-ons can create a significant amount of displaced atoms. In some cases, the cascade is considered a spike - a highly dense cascade in a limited volume in which the atoms are temporarily in motion. Brinkman [52] suggested that if the average distance between collisions is on the order of the average atomic spacing in a material, then a PKA can develop a highly damaged region by displacing nearly every atom along its path, like the cascade depicted in Fig. 23. This would create a region of vacancies or free volume surrounded by the target material and displaced atoms. This damaged region was

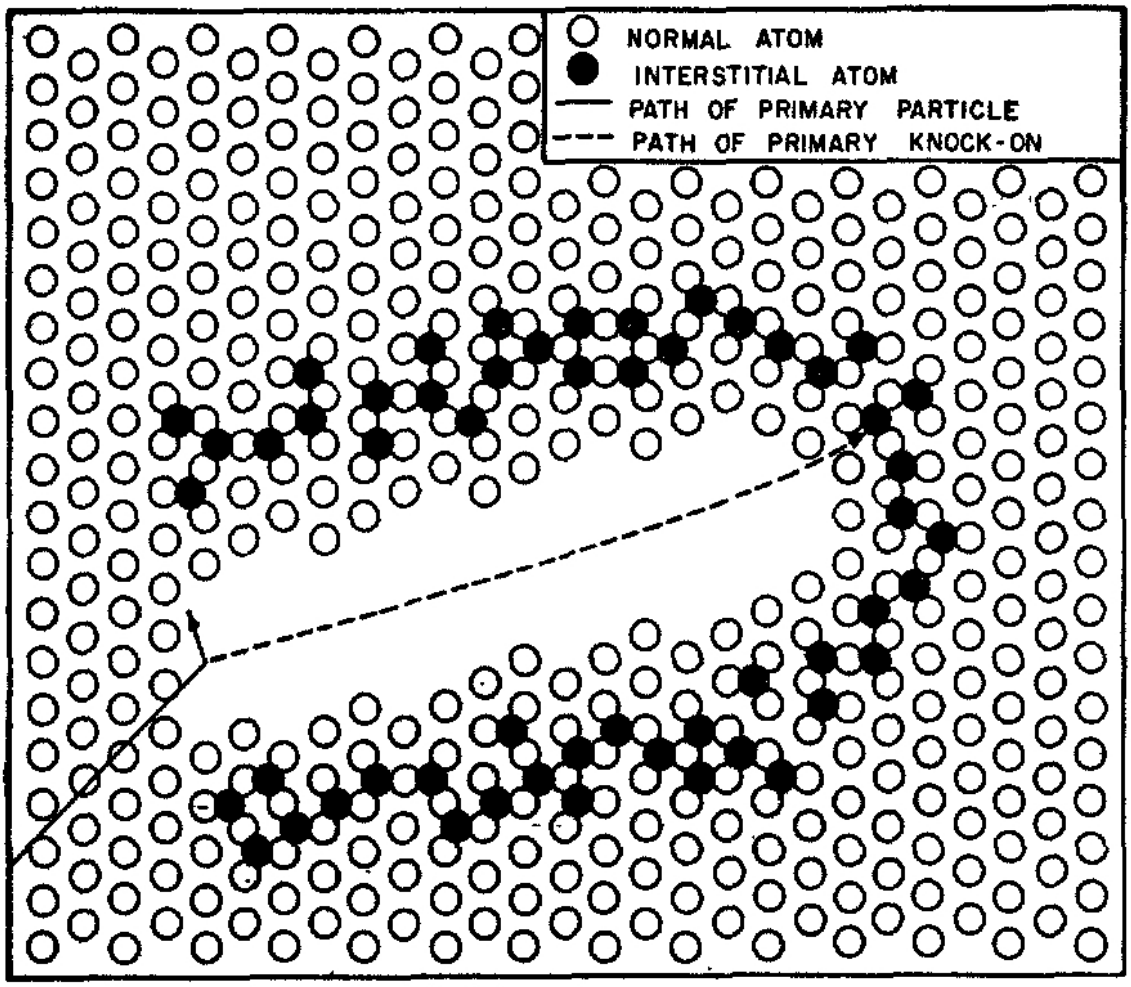

Fig. 23. Displacement cascade caused by primary knock-on atom in which the average distance between displacements is on the order of the atomic spacing.

referred to as a displacement spike since of the density of displacements is in a limited volume.

Another characteristic of the displacement cascade is the thermal spike. As atoms come to rest and no longer retain enough energy to cause further displacements, they dissipate their energy through vibrations and share such energy with neighboring atoms. The vibrational energy of the atoms gives an impression of localized heating and which is the reasoning behind the term thermal spike. The cascade temperature can reach several thousand degrees Kelvin for reasonable implantation conditions. The quench rate for such localized heating is very fast - on the order of picoseconds [48].

We now have a picture of how irradiation of metallic glasses leads to diffusivity enhancement and eventually crystallization. Particle irradiation can cause regions of displaced atoms, leaving behind regions of free volume. An enhancement in free volume leads to a diffusivity increase in metallic glasses that can give rise to atomic mobility near the displacement cascade leading to eventual crystallization. The amount of free volume enhancement will depend on the damage cascade size, therefore the nanocrystal sizes produced by particle irradiation should depend on the energy and mass of projectiles. Hence the mass-dependent study performed for this dissertation. Normally this creation of displacements and resulting vacancies is considered "damage" in a crystalline material. The free volume and atomic mixing of a displacement cascade, as shown in Fig. 23 for a crystalline structure, can be very important for the diffusion of atoms and local composition fluctuation.

CHAPTER IV

ELECTRON IRRADIATED MG1 AND MG2*

Ribbon samples of $Zr_{55}Cu_{30}Al_{10}Ni_5$ and $Cu_{50}Zr_{45}Ti_5$ metallic glasses, with a thickness of 20 μm and a width of 1.5 mm, were prepared by rapid solidification of metallic liquid on a rotating copper roller. Transmission electron microscopy (TEM) and high-resolution TEM were performed using a JEOL 2010 microscope equipped with a Gatan SC1000 ORIUS CCD camera, operated at 200 kV. The TEM specimens were prepared by electropolishing at 243 K using a twin jet thinning electropolisher with a solution of 25% nitric acid and 75% methanol. Differential scanning calorimetry (DSC) measurements were performed under a purified argon atmosphere in a TA Instruments DSC-Q1000 calorimeter with a finned air-cooling system.

Fig. 24 compares DSC curves for as-spun $Zr_{55}Cu_{30}Al_{10}Ni_5$ and $Cu_{50}Zr_{45}Ti_5$ metallic glasses. DSC was performed at a heating rate of 0.33 K/s. Glass transition temperatures were estimated to be 687 K for $Cu_{50}Zr_{45}Ti_5$ and 697 K for $Zr_{55}Cu_{30}Al_{10}Ni_5$. These temperatures correspond to the transition from glassy to supercooled liquid. At higher temperatures, the crystallization process starts involving nucleation and growth of crystalline phases. Fig. 24 shows that the onset temperatures of the first-step crystallization are different for each MG. The crystallization temperature is around 722 K for $Cu_{50}Zr_{45}Ti_5$ and is 762 K for $Zr_{55}Cu_{30}Al_{10}Ni_5$. Thus, these two metallic glasses have different widths of the supercooled liquid region, which is a gauge to evaluate the thermal stability against crystallization [1]. A wider supercooled liquid region for the metallic glass $Zr_{55}Cu_{30}Al_{10}Ni_5$ indicates greater thermal

*Reprinted with permission from "Electron irradiation-induced structural transformation in metallic glasses" by E. G. Fu, J. Carter, M. Martin, G. Xie, X. Zhang, Y. Q. Wang, R. Littleton, and L. Shao, 2009. *Scripta Materialia*, vol. 61, pp. 40-43. doi:10.1016/j.scriptamat.2009.03.001

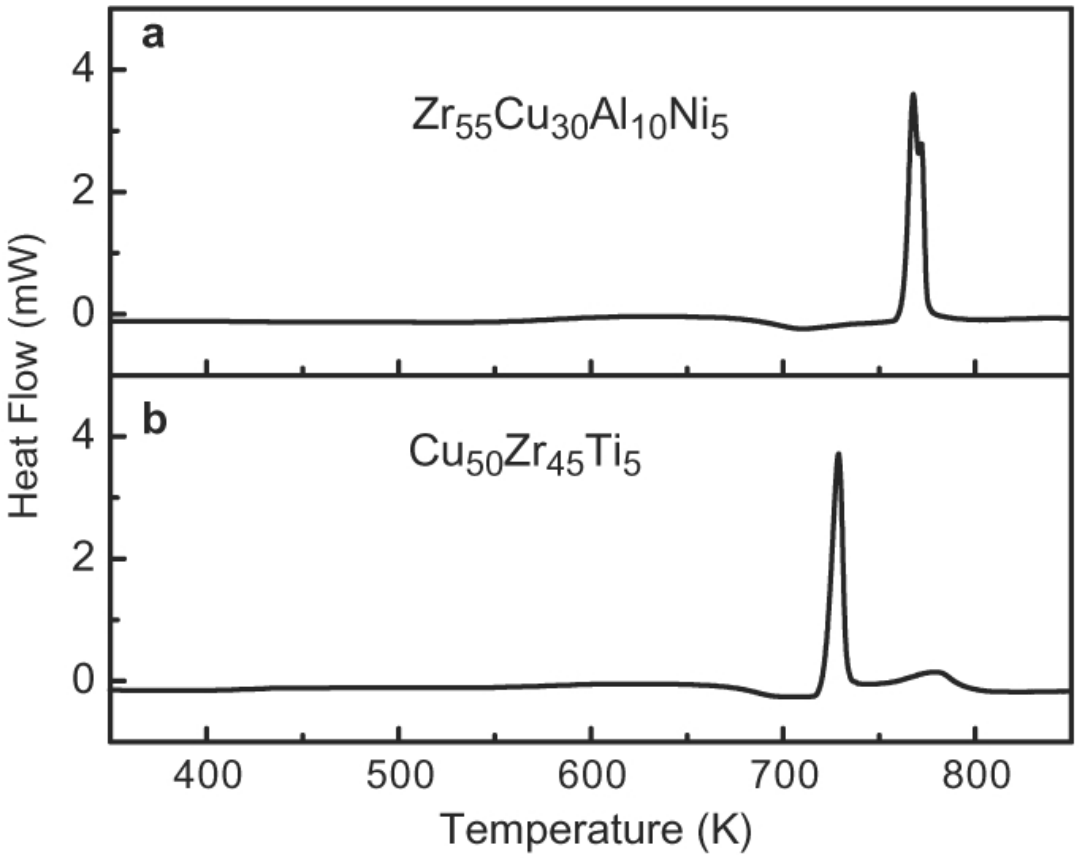

Fig. 24. DSC traces of the as-spun metallic glasses before electron irradiation: (a) $Zr_{55}Cu_{30}Al_{10}Ni_5$; (b) $Cu_{50}Zr_{45}Ti_5$.

stability against crystallization compared to metallic glass $Cu_{50}Zr_{45}Ti_5$.

Figs. 25 and 26 compare TEM micrographs for metallic glass $Zr_{55}Cu_{30}Al_{10}Ni_5$ and $Cu_{50}Zr_{45}Ti_5$, respectively, subjected to 200 keV electron irradiation to different fluences. Insets are the selected area diffraction (SAD) patterns for the corresponding TEM images. Fig. 25(a-c) corresponds to $Zr_{55}Cu_{30}Al_{10}Ni_5$ after electron irradiation to $t = 0$, 15 and 30 min, respectively. The value t refers to the elapsed time after TEM characterization/electron irradiation started. Each image was taken within a few seconds. The specimen was continuously irradiated between each imaging. The electron beam was about 150 nm in diameter and the current density was around 11 A/cm^2. Therefore, the specimens shown in Fig. 25(a-c) were irradiated to an electron fluence of 0, 4.4×10^{26} and 8.7×10^{26} electrons/m^2, respectively. In $Zr_{55}Cu_{30}Al_{10}Ni_5$ specimens irradiated at all three fluences, no crystalline phases were detected. SAD patterns in Fig. 25(a-c) show large diffuse halo rings. This suggests that $Zr_{55}Cu_{30}Al_{10}Ni_5$ retains its glassy structure during electron irradiation.

Fig. 26(a-c) shows microstructural changes of $Cu_{50}Zr_{45}Ti_5$ under electron irradiation of fluences of 0, 4.4×10^{26} and 8.7×10^{26} electrons/m^2, respectively. In Fig. 26(a), both the TEM image and the SAD pattern suggest the sample is in a glassy phase. After electron irradiation to a fluence of 4.4×10^{26} electrons/m^2, the SAD pattern in Fig. 26(b) begins to show white diffraction dots, indicating the nucleation of nanocrystals. However, at this stage the size of the nanocrystals is very small, below the detection limit of TEM. After electron irradiation to a fluence of 8.7×10^{26} electrons/m^2, the SAD pattern in Fig. 26(c) clearly shows sharp diffraction spots and discontinuous diffraction rings. Nanocrystal formation is immediately apparent in the corresponding high-resolution TEM image. The typical size of the formed nanocrystals is around 10 nm.

Fig. 27(a) shows the fast Fourier transform (FFT) pattern from the selected

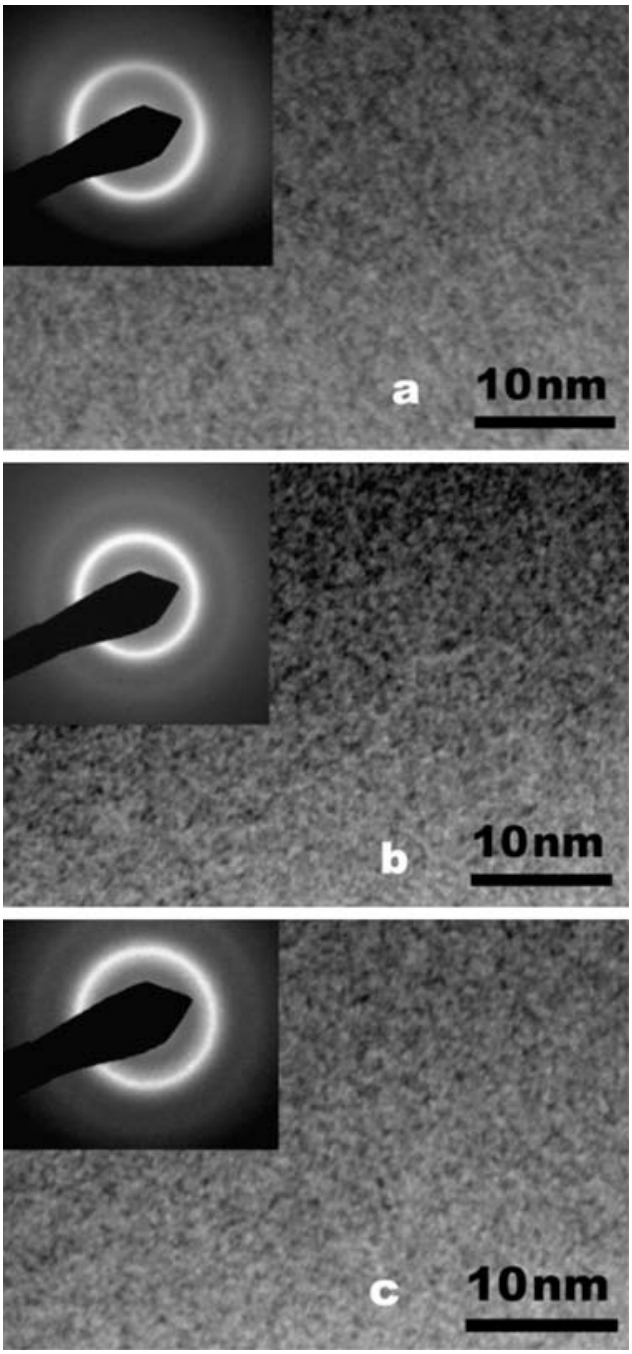

Fig. 25. TEM micrographs of $Zr_{55}Cu_{30}Al_{10}Ni_5$ under 200 keV electron irradiation for (a) 0 min, (b) 15 min, and (c) 30 min.

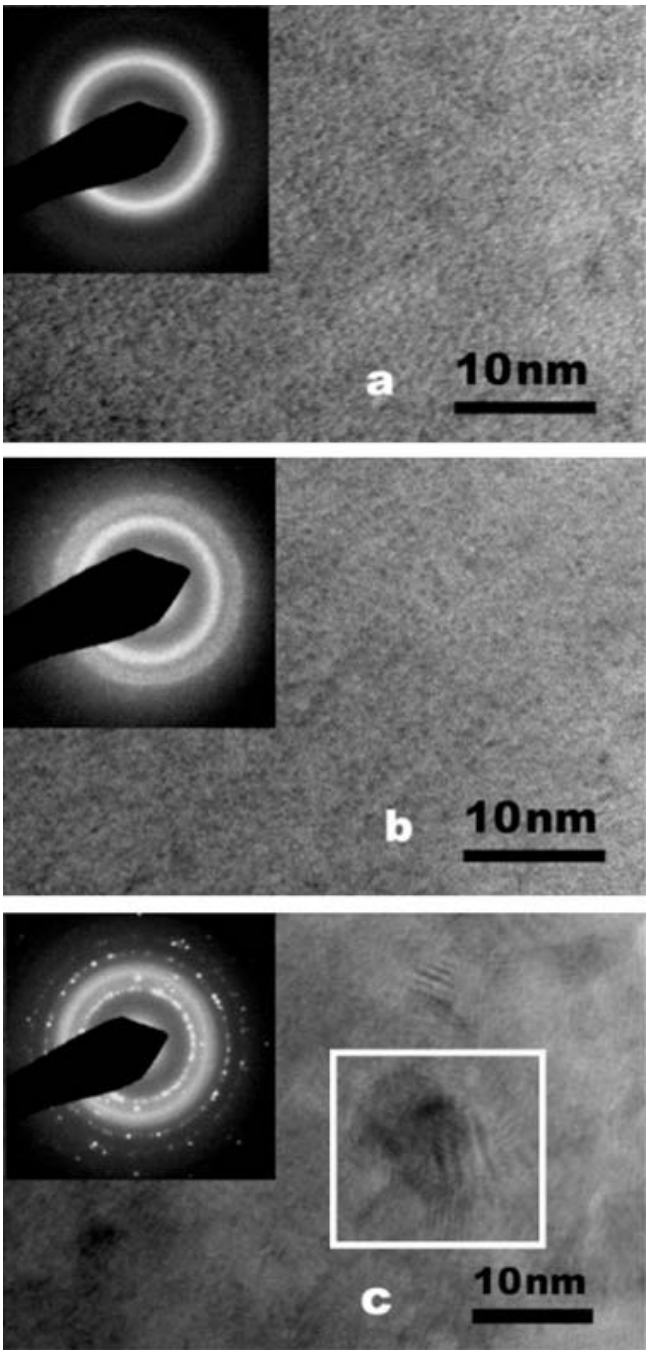

Fig. 26. TEM micrographs of $Cu_{50}Zr_{45}Ti_5$ under 200 keV electron irradiation for (a) 0 min, (b) 15 min, and (c) 30 min.

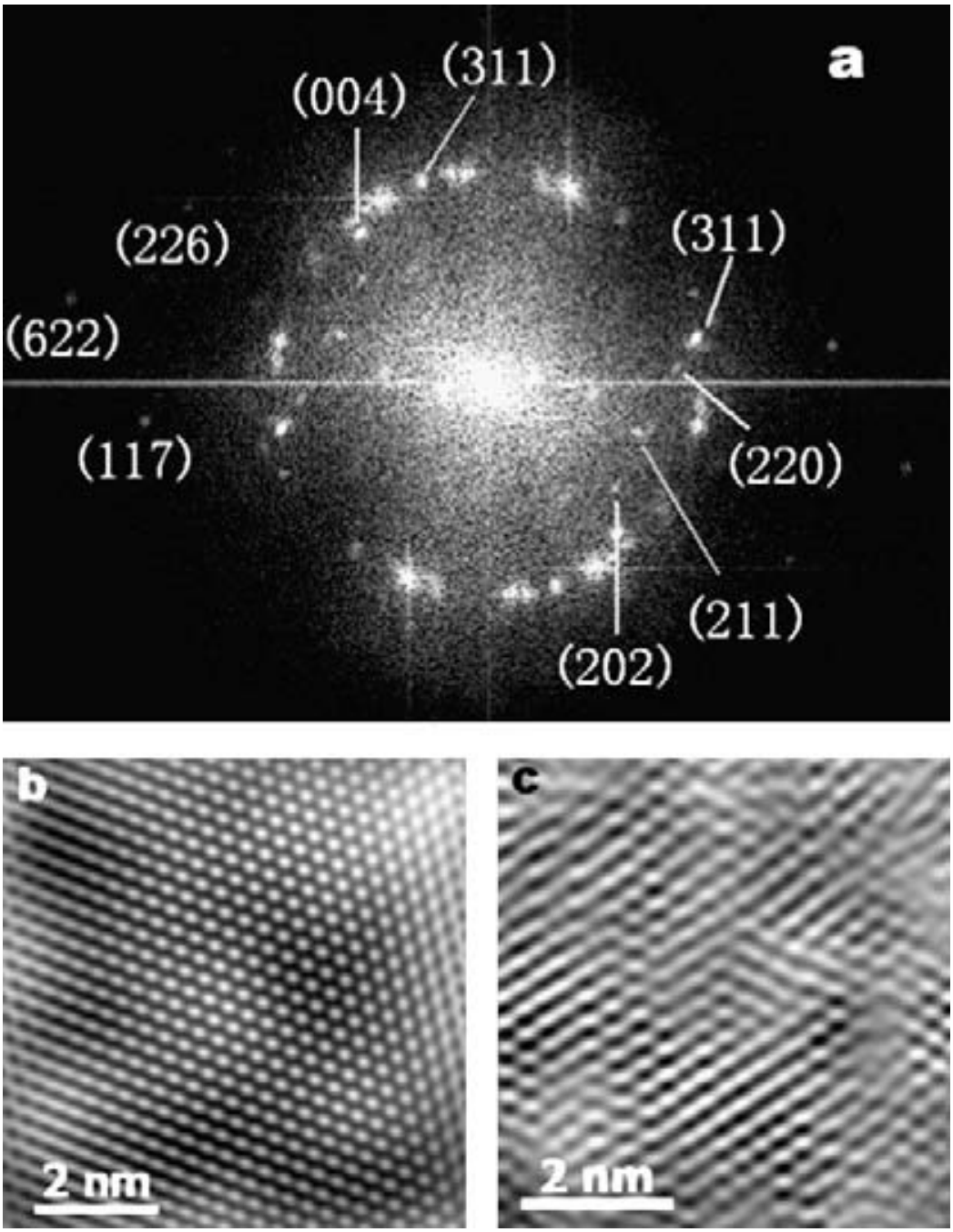

Fig. 27. (a) FFT pattern of electron irradiated $Cu_{50}Zr_{45}Ti_5$ in the area marked in Fig. 26(c); (b) inverse FFT of a defect-free region; (c) inverse FFT of a region forming dislocations.

area (marked by the box in Fig. 26(c)). Indexing of the FFT pattern indicates the phase of nanocrystals to be predominantly $Cu_{10}Zr_7$; other minor phases are difficult to identify unambiguously from FFT. Fig. 27(b) is an inverse FFT of a selected area in which a perfect nanocrystal is formed. In many other regions, defects such as dislocations are found to form in nanocrystals, as shown in a representative example in Fig. 27(c). Dislocations were counted using inverse FFT at different orientations (not shown here), which provided a dislocation density of 5×10^{17} m^{-2}.

The maximum recoil energy received by a target atom under a head-on collision can be calculated by [48]:

$$E_{max} = \frac{4m_e M E}{(m_e + M)^2}, \tag{4.1}$$

where E is the electron energy, m_e is the electron mass and M is the target atom's mass. The lightest target atom will gain the highest knock-on energy. The maximum transferred energies are 9.1 eV for Ti and 16.2 eV for Al. Both energies are less than the displacement energies of their crystalline elemental materials ($E_d \approx 20$ eV for Ti and $E_d \approx 17$ eV for Al) [48]. However, Bellini et al. [53] has pointed out that the local displacement energy in glass is inversely correlated with the amount of free volume (FV), making it lower than that in the corresponding crystalline compound. Once atoms are displaced, vacancy-like defects are created, leading to the introduction of additional excessive FV and open space for atomic migration. Molecular dynamics simulation revealed that removing atoms from the structure result in a transient high-mobility region around the defects and a low mobility region, enabling the excessive FV to spread out over the whole sample over a longer time [54]. The diffusivity extracted from the simulation can be described by [54]:

$$D = D_0 \exp\left(V_f / V_0\right), \tag{4.2}$$

where V_0 is some activation volume, and V_f is the excess free volume introduced by removing atoms.

Based on the FV approaches originally introduced by Cohen and Turnbull [42] and later by Spaepen [43], it is expected that enhanced atomic mobility will lead to increased short-range order and subsequent nucleation. Therefore, irradiation-induced crystallization can occur at low temperature. However, due to the preferred displacements of light atoms by knock-on collisions, the irradiation enhanced displacement flux might be species dependent and the crystallization sequence could be different than thermal annealing.

It can be concluded that the electron-beam heating is negligible in this study. The temperature rise during electron irradiation can be estimated by [55]:

$$\Delta T = \frac{I}{\pi k e}\left(\frac{dE}{dx}\right)\ln\frac{R}{r_0}, \tag{4.3}$$

where k is the thermal conductivity (k = 9 W/mK for $Cu_{50}Zr_{45}Ti_5$ and 5 W/mK for $Zr_{55}Cu_{30}Al_{10}Ni_5$), R (= 1.5 mm) is the TEM specimen radius, r_0 (= 150 nm) is the electron-beam radius, I (= 12 nA) is the beam current and dE/dx is the stopping power of electrons, which can be calculated by [56]:

$$\frac{dE}{dx}(\text{keV/cm}) = -7.85\times10^4\frac{Z\rho}{AE}\ln\left(\frac{1.166E}{J}\right), \tag{4.4}$$

$$J(\text{keV}) = \left(9.76Z + 58.5Z^{-0.19}\right)\times10^{-3}, \tag{4.5}$$

where Z is the averaged atomic number, ρ is the density (ρ = 7.23 g/cm^3 for $Cu_{50}Zr_{45}Ti_5$ and 6.83 g/cm^3 for $Zr_{55}Cu_{30}Al_{10}Ni_5$), A is the atomic weight (g/mol) and E is beam energy. The calculated stopping powers are 1.01 eV/nm for $Cu_{50}Zr_{45}Ti_5$ and 1.08 eV/nm for $Zr_{55}Cu_{30}Al_{10}Ni_5$. Substituting the values into Eqns. 4.4 - 4.5 gives a temperature rise of 4.6 K for $Cu_{50}Zr_{45}Ti_5$ and 7.6 K for $Zr_{55}Cu_{30}Al_{10}Ni_5$. The

electron-beam heating during irradiation is therefore negligible.

Formation of stable crystalline phases requires correlated atomic movements and rearrangements. Thus, crystallization is difficult if the nucleating phase has a complicated structure. Previous studies have shown that annealing of $Cu_{50}Zr_{45}Ti_5$ results in formation of the crystalline $Cu_{10}Zr_7$ phase. On the other hand, products of crystallized $Zr_{55}Cu_{30}Al_{10}Ni_5$ are very complicated. XRD analysis of annealed $Zr_{55}Cu_{30}Al_{10}Ni_5$ has identified tetragonal Zr_2Ni and $(Al_{1.7}Ni_{0.3})Zr$ intermetallic compounds, as well as several other unidentified phases [53]. Formation of multiple phases is believed to be the reason for the high stability of $Zr_{55}Cu_{30}Al_{10}Ni_5$ glass. Electron irradiation under the current conditions seems to be insufficient in overcoming the activation energy barrier to form multiple crystalline phases in amorphous $Zr_{55}Cu_{30}Al_{10}Ni_5$ glass.

After crystallization, continued irradiation will create defects in the newly formed nanocrystal, which results in an increase in free energy (~5 eV for a Frenkel pair in face-centered cubic metal) [48]. Defects can also form in the as-grown nanocrystals without irradiation. If the free energy reaches a critical value, amorphization is possible [48]. The critical point defect concentration for this is estimated to be around 1% (atomic percentage) in metals [48], which is achievable under high fluence electron irradiation. However, the high free energy can be relieved through the formation of dislocations [20], which greatly lowers the maximum defect concentration in the system.

The stability of $Cu_{50}Zr_{45}Ti_5$ under electron irradiation has been previously studied by Xie et al. [33]. The crystalline phase was found to be monoclinic CuZr, rather than $Cu_{10}Zr_7$ phases identified in this study. In both studies, a number of weak unidentified phases are present, and coexistence of several phases is suggested. Formation of dominant phases might be sensitive to electron flux. In this study, the

electron flux is 6.9×10^{23} electrons/m^2 – s, which is around one order of magnitude larger than the flux used in previous studies (8×10^{22} electrons/m^2 – s).

Previous studies have suggested that the activation energy for nucleation is larger than the activation energy for crystal growth in amorphous alloys [57, 58]. This has been used to explain the difference in shear-band-formation-induced nanocrystallization [58]. This study suggests that the activation energy for crystallization in $Zr_{55}Cu_{30}Al_{10}Ni_5$ is higher than that in $Cu_{50}Zr_{45}Ti_5$. However, once nucleation sites are introduced, these two glasses could have very different growth behaviors. In a separate study, we have observed nanocrystal formation in both metallic glasses after high-energy Cu ion irradiation. Interestingly, once nucleation is initialized, crystal growth in $Zr_{55}Cu_{30}Al_{10}Ni_5$ is faster than that in $Cu_{50}Zr_{45}Ti_5$, which suggests that the activation energy for crystal growth in $Zr_{55}Cu_{30}Al_{10}Ni_5$ is comparable to, if not less than, that in $Cu_{50}Zr_{45}Ti_5$.

This study shows that a material's intrinsic property, i.e. width of the supercooled liquid region, affects its crystallization under electron irradiation. Thus it seems meaningful to carry out a comparison study in crystallization of amorphous alloys having different supercooled liquid widths under other conditions, including bending and deformation. A difference in their crystallization behavior might be observed.

From the viewpoint of application, electron irradiation can be used to modify bulk glass since high-energy electrons can penetrate through a large thickness. The technique has certain advantages over other techniques, such as shear-band-formation-induced nanocrystallization, since the latter phenomenon occurs after structural failure.

In summary, we have shown that $Zr_{55}Cu_{30}Al_{10}Ni_5$ has greater stability against crystallization than $Cu_{50}Zr_{45}Ti_5$ under electron irradiation. Irradiation with 200 keV

electrons to a fluence of 8.7×10^{26} electrons/m^2 results in the formation of $Cu_{10}Zr_7$ nanocrystals in $Cu_{50}Zr_{45}Ti_5$ metallic glass, but no crystallization is detected in $Zr_{55}Cu_{30}Al_{10}Ni_5$ metallic glass. Electron-beam heating is negligible. Furthermore, high-density dislocations are observed in crystalline $Cu_{10}Zr_7$ phases. This suggests that point defects in the system are highly mobile. Nucleation of dislocations is believed to be the mechanism to avoid the reamorphization of the formed crystalline phase.

CHAPTER V

HELIUM IRRADIATED MG1*

Our study began with preparing a $Cu_{50}Zr_{45}Ti_5$ alloy by melting mixtures of pure Cu, Zr and Ti in an argon atmosphere [33]. Ribbon-shaped samples, 1.5 mm in width and about 20 μm thick, were obtained by rapid solidification of the melt on a single copper roller at a peripheral velocity of 42 m/s in an argon atmosphere. The sample was cut into pieces and irradiated at room temperature with 140 keV He ions to a fluence of 1.7×10^{17} ions/cm^2. Implantation of He atoms was motivated by the need to form high strength porous materials with enhanced mechanical properties and reduced density. We selected 140 keV as the implantation energy primarily due to feasibility of the accelerator instruments. The homemade accelerator was optimized for this energy. Beam heating was measured to be less than 50 °C. Nanoindentation tests were performed on both specimens (as-spun and irradiated) in order to obtain the distribution of hardness as a function of depth. Due to the thickness and curvature of the specimens, it was necessary to mount the specimens onto a microscope slide using superglue to ensure proper measurements. Due to the limitation of the maximum penetration depth in the nanoindentation tests, microindentation tests were also performed using a Fischerscope HM2000 with a Vicker's indenter. Irradiation induced hardness changes were extracted by comparing data before and after ion irradiation. Depth dependent hardness changes were discussed and compared with stopping powers of He ions, obtained by using the Stopping and Range of Ions in

---

*Reprinted with permission from "Effects of ion irradiation in metallic glasses" by J. Carter, E. G. Fu, G. Bassiri, B. M. Dvorak, N. D. Theodore, G. Xie, D. A. Lucca, M. Martin, M. Hollander, X. Zhang, and L. Shao, 2009. *Nuclear Instruments and Methods in Physics Research B*, vol. 267, pp. 1518-1521. Copyright 2009 by Elsevier. doi:10.1016/j.nimb.2009.01.081

Matter (SRIM) code [49]. High resolution transmission electron microscopy (TEM) was performed to characterize the samples.

The values for hardness as a function of contact depth for both as-spun and irradiated specimens are shown in Fig. 28. A set of five loads were initially utilized in order to determine the distribution of hardness. In order to obtain the greatest possible depth profile, an additional load was added (10,000 μN). Each data point in Fig. 28 represents the average hardness value for five indentation measurements at each load and the error bars represent the maximum and minimum values obtained. As shown in Fig. 28, there are no significant hardness changes from the surface up to 250 nm.

Fig. 29 shows the hardness in both the as-spun and irradiated metallic glass samples obtained by using microindentation. At a depth of around 600 nm, the hardness increases from 9 GPa (as-spun) to 12 GPa in the irradiated samples. The hardness change becomes much smaller at depths beyond 1000 nm. Different from the nanoindentation tests, which give more reliable data in the near surface region, hardness data obtained by microindentation is not reliable for depths shallower than ~200 nm. Hardness changes observed at a depth of approximately 600 nm, as shown in Fig. 29, indicate a significant mechanical property change in the ion irradiated metallic glasses.

Fig. 30 shows the hardness changes extracted from the data in Fig. 29. Hardness enhancement in the irradiated sample reaches a peak at a depth of around 600 nm. The trend of the curve from 300 to 600 nm suggests that hardness enhancement is negligible for shallow depths (< 300 nm). This observation is consistent with the data obtained by nanoindentation.

It is well known that the contribution to ion stopping in solids originates from two different mechanisms - nuclear and electronic stopping [48]. In nuclear stopping, ions

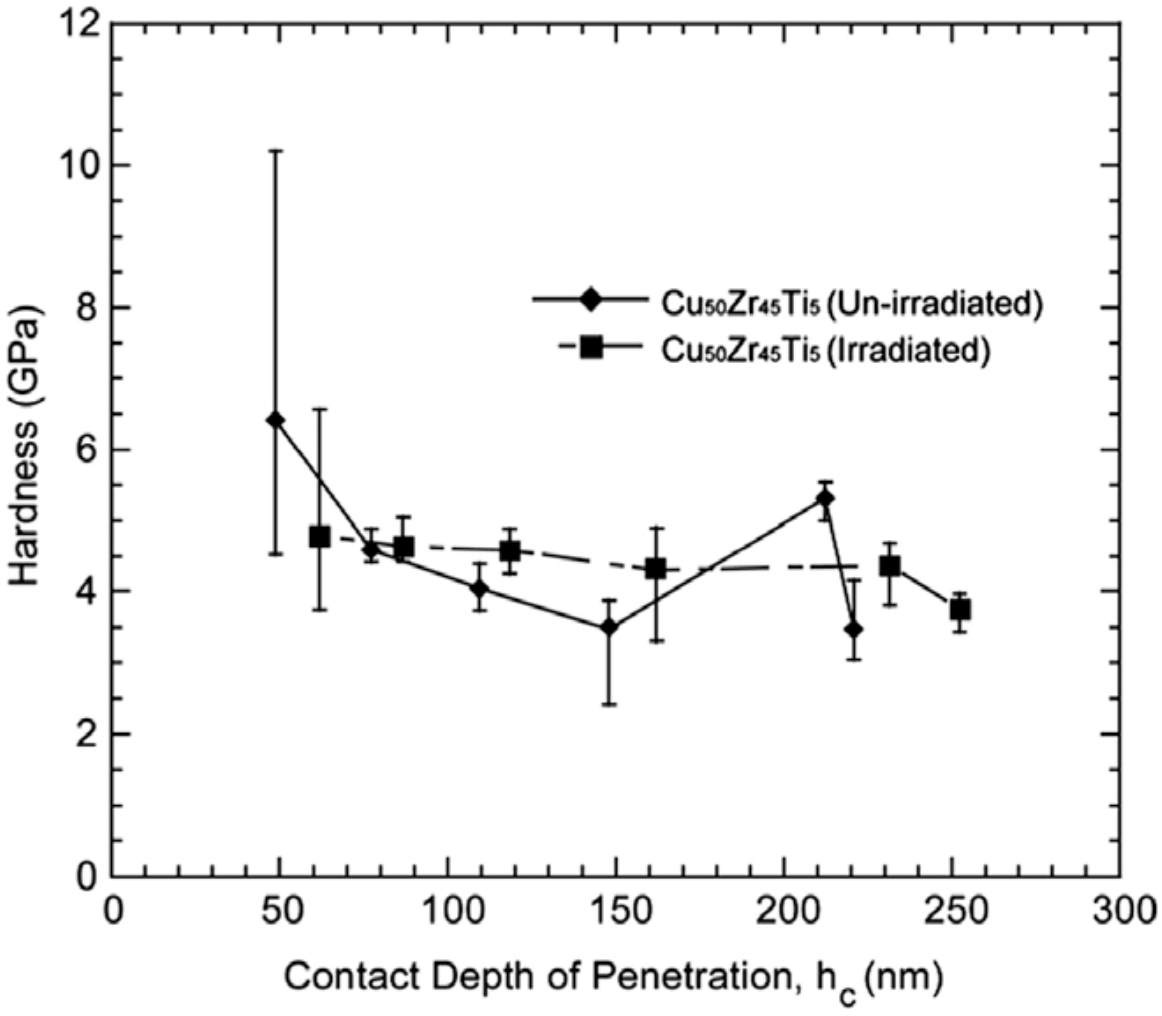

Fig. 28. Plot of indentation hardness of unirradiated and irradiated $Cu_{50}Zr_{45}Ti_5$ metallic glass samples versus contact depth obtained from nanoindentation.

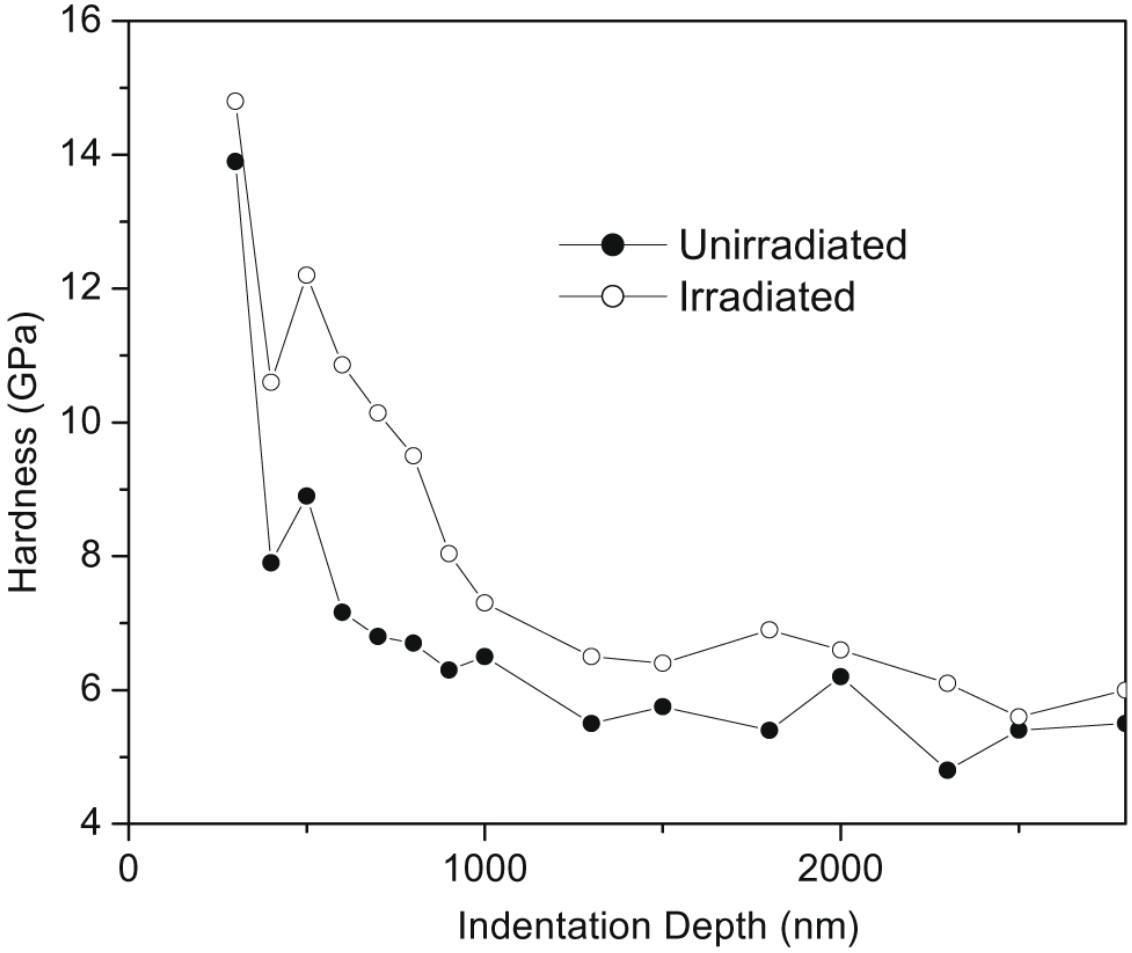

Fig. 29. Plot of indentation hardness of unirradiated and irradiated $Cu_{50}Zr_{45}Ti_5$ metallic glass samples versus indentation depth obtained from microindentation.

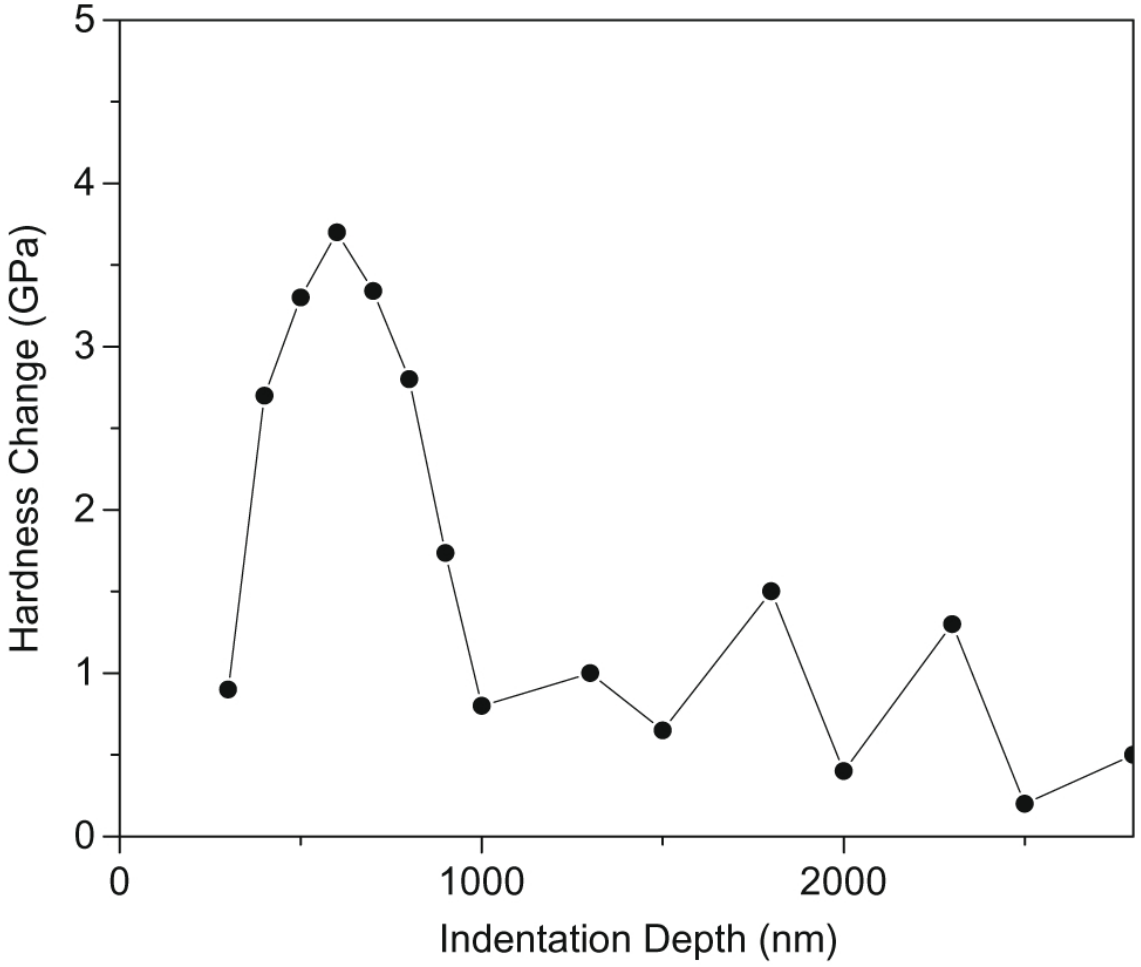

Fig. 30. Hardness change between unirradiated and irradiated metallic glass. The data is calculated based on Fig. 29.

lose energy by ion-target nuclear collisions; in electronic stopping, ions lose energy by collision with target electrons. The relative importance of these two stopping mechanisms depends on the velocity and charge state of the ions. Fig. 31 compares electronic and nuclear stopping powers of He ions in the sample. SRIM does not directly provide stopping powers as a function of depth. We first used SRIM to calculate stopping powers as a function of energy. Then the energy was converted into the corresponding depth for 140 keV He ions. As shown in Fig. 31, electronic stopping decreases with increasing depth, while nuclear stopping peaks at a depth of ~600 nm, which corresponds to the projected range of 140 keV He ions in this metallic glass. Our study suggests that the hardness enhancement is due to either the nuclear stopping process or implanted He atoms, and the electronic stopping process is not playing a dominant role in the mechanical property changes.

Fig. 32 shows a dark-field TEM image of the unirradiated metallic glass. No nanocrystalline particles are observed. The selected area diffraction (SAD) pattern further confirms its amorphous phase. In comparison, Fig. 33 shows a bright-field TEM of the irradiated sample. The bright spots (as indicated by arrows) correspond to helium bubbles and/or voids formed in the sample. It is difficult to distinguish one from the other since both types of defects are open volume defects. Such defects are frequently observed in gas-atom-irradiated alloys [20]. The half width of 140 keV He implant distribution is around 100 nm. If all implanted He atoms are retained at the end of their ranges, the He concentration near the peak region is estimated to be around 6×10^{21}atoms/cm^3. Circles in Fig. 33 refer to typical nanocrystalline particles. The crystallites have irregular shapes and sizes ranging from a few nanometers up to 100 nm. Nanocrystal formation is further confirmed by the SAD pattern (the inset in Fig. 33) and dark-field TEM (not shown here).

Limited studies have shown that the dispersion of nanocrystals in an amorphous

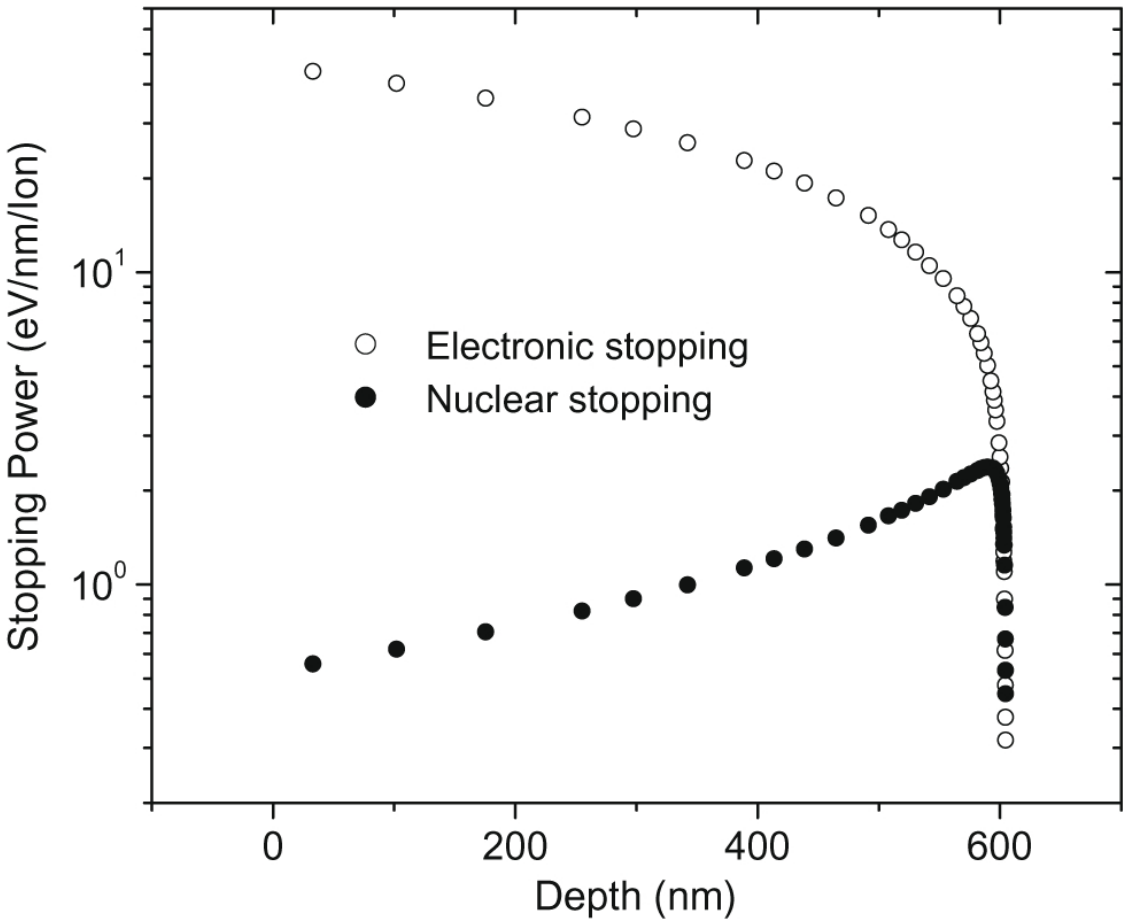

Fig. 31. A comparison of nuclear stopping and electronic stopping as a function of penetration depth in $Cu_{50}Zr_{45}Ti_5$ metallic glass for 140 keV He ions. The data is calculated using SRIM code.

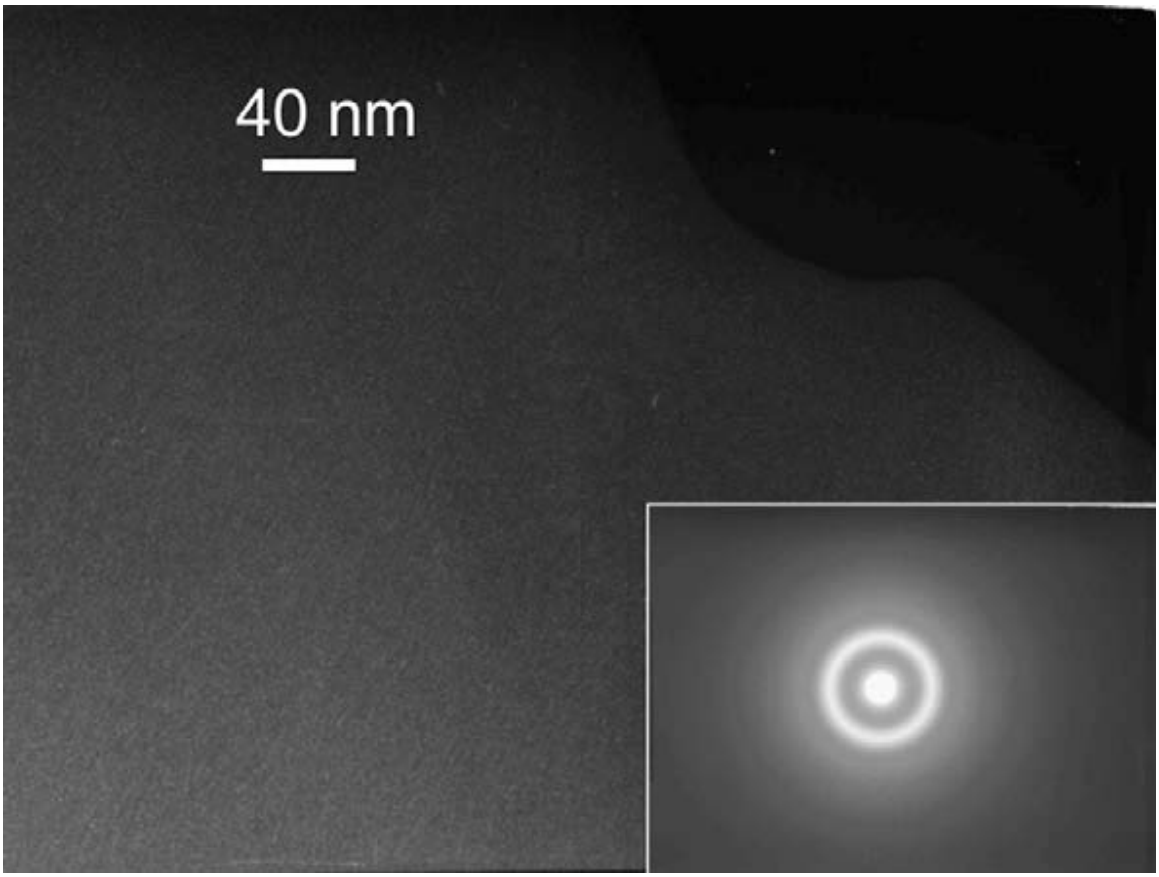

Fig. 32. Dark-field TEM image of the unirradiated metallic glass. The inset represents the corresponding selected area diffraction pattern.

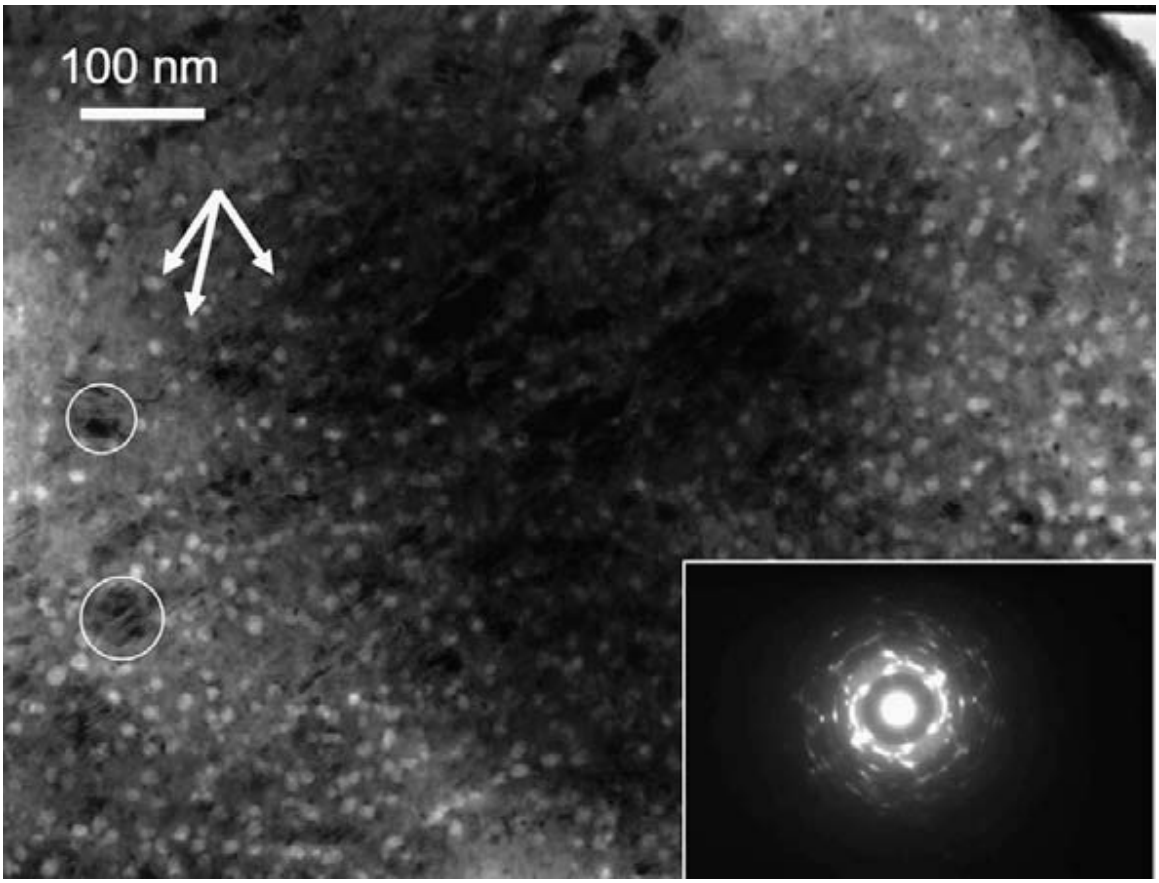

Fig. 33. Bright-field TEM image of irradiated metallic glass. The inset represents the corresponding selected area diffraction pattern.

matrix can lead to dispersion strengthening of the materials [59, 60]. Therefore, it is expected that the yield strength will increase as a function of the volume fraction of nanocrystals [61]. We hypothesize that nanocrystal formation is related to damage cascade formation. Development of the damage cascade is a very complicated process. Basically, after the initial damage cascade and associated thermal spike formation, the core of the cascade forms a "liquid-like" hot zone. The zone is virtually cooled to an ambient temperature after a "quenching" process. During quenching, energy is dissipated via lattice vibrations [48]. Damage cascade formation may involve phase separation and asymmetric diffusion between different elements. Significant energy deposition associated with the formation of a melting zone is equivalent to localized high temperature heating. This local heating can cause chemical decomposition and periodic composition fluctuations which give rise to nanocrystal formation. However, it is worthy to point out that the cooling rate after thermal spike is certainly faster than cooling rate of the initial quench. Even if the material has localized melting, it does not necessarily lead to nanocrystal formation. It is possible that nanocrystal formation is due to enhanced mobility of atoms under irradiation. The mechanisms are not clear at this stage.

Gas atom implantation, such as the He implantation used in this study, could be used for development of porous high strength alloy coatings. A conclusive explanation of the mechanisms responsible for hardness changes is difficult in the case of gas atom implantation since such hardness changes can be influenced by both nanocrystal formation and bubble formation. In order to know their relative contributions, self ion irradiation into metallic glass is necessary.

We have studied ion irradiation induced hardness changes in a $Cu_{50}Zr_{45}Ti_5$ metallic glass alloy. After 140 keV He ion irradiation to a fluence of 1.7×10^{17}ions/cm^2, a maximum in hardness enhancement occurs at a depth close to the maximum nu-

clear stopping and projected range of the implants. TEM studies have identified nanocrystals formed in the irradiated metallic glasses.

CHAPTER VI

HELIUM IRRADIATED MG2

This study began by preparing metallic glass ribbon samples with composition $Zr_{55}Cu_{30}Al_{10}Ni_5$ (atomic percentages). Samples were prepared by rapid solidification of molten Zr, Cu, Al, and Ni in an argon atmosphere. Rapid solidification was achieved by applying the mixture to a single copper roller moving at a peripheral velocity of 42 m/s [33]. The result was long ribbons about 1.5 mm wide and 20 μm in thickness. The ribbons were then exposed to 140 keV He ions to a fluence of 4×10^{17} ions/cm^2 at room temperature. Average beam current was about 1 μA/cm^2. Selection of 140 keV was primarily due to feasibility with accelerator equipment since the homemade accelerator was optimized for this energy. He ions were used with the intention of creating a low-density, porous material. Beam heating of sample was measure to be less than 50 °C. Samples were prepared for Transmission Electron Spectroscopy (TEM) by mechanical thinning and then ion milling in a Fischione Model 1010 Ion Mill. Samples were thinned down to thickness of about a micron and then ion milled until thin enough for proper TEM characterization. Ion milling was done with 2 keV Ar ions and liquid nitrogen cooling below -100 °C. Low energy ions at low temperatures maintained the sample microstructure throughout the milling process while the sample was continuously rotated to achieve uniform thinning. TEM characterization was performed by using a JEOL 2010 microscope equipped with a Gatan SC1000 ORIUS CCD camera. Specimens were observed with low electron flux because previous studies have shown that long exposure to TEM analyzing beam can induce nanocrystallization [62].

A bright-field (BF) TEM micrograph of an unirradiated specimen is shown in Fig. 34. The unirradiated specimen contains no composition contrast or ordered

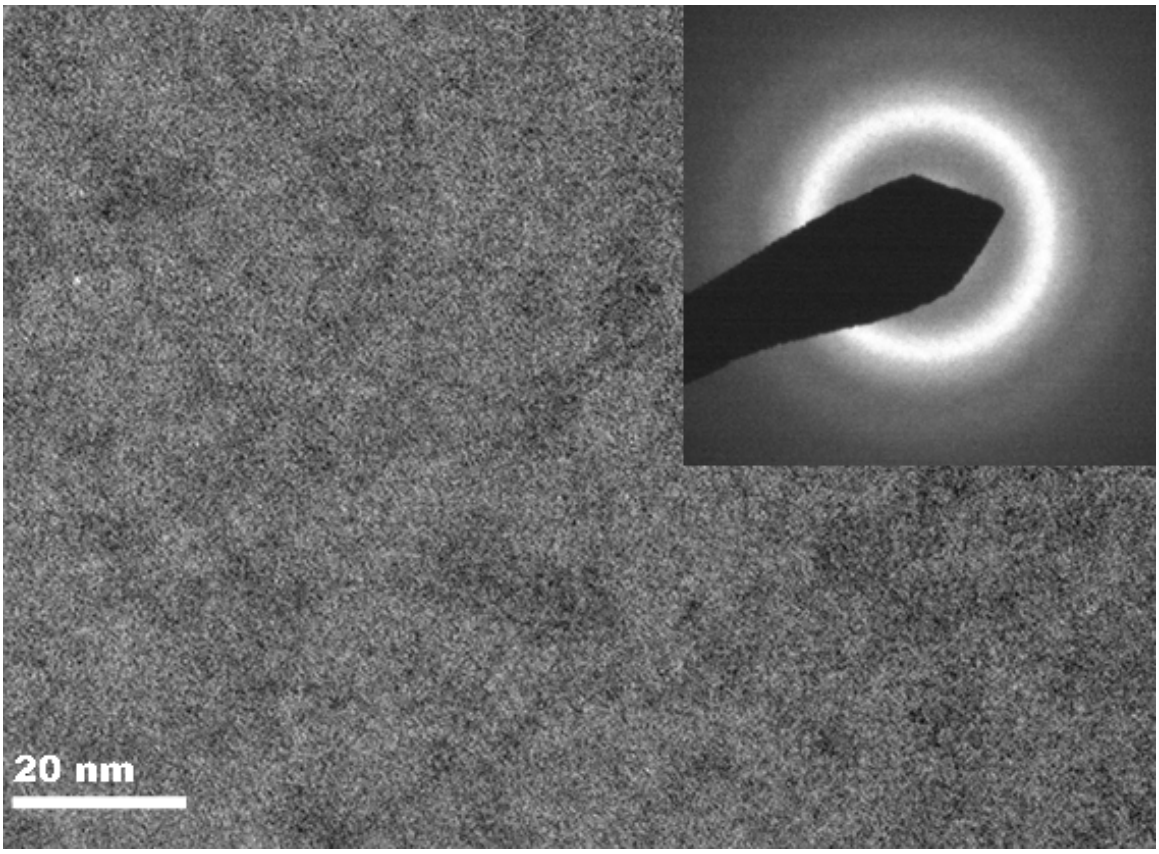

Fig. 34. Bright-field TEM micrograph of unirradiated metallic glass specimen $Zr_{55}Cu_{30}Al_{10}Ni_5$ prepared by ion milling at low temperature. Selected area diffraction pattern of the specimen is shown as an inset.

structure; only a random pattern showing the random nature of the microstructure. The selected area diffraction pattern (SAD) is shown as an inset to Fig. 34. The SAD shows only a halo-like ring with no bright spots. The SAD verifies the amorphous nature of the microstructure. Checking the structure of the unirradiated specimens allows for verification of the amorphous state prior to irradiation and shows that proper ion milling conditions have been achieved. Differential Scanning Calorimetry (DSC) was performed on the unirradiated specimen (not shown) revealing typical annealing behavior of a glassy metal with a glass transition temperature of 697 K and first-step crystallization at 762 K [62].

Bright-field and dark-field (DF) TEM micrographs of He irradiated specimens are shown in Figs. 35(a) and 35(b), respectively. Fig. 35(a) reveals drastic microstructure modification due to ion irradiation. Bright-field images reveal nanocrystals, precipitations, and bubbles. Nanocrystal formation is verified by SAD as seen as inset in Fig. 35(a). Nanocrystals can also be seen in DF image shown in Fig. 35(b) as bright spots. Comparing BF and DF images reveals that the large grey contrasts seen in the BF are not seen in the DF. We conclude they are precipitations brought about by ion irradiation but not crystalline since they do not show on DF image. The DF image shows nanocrystal size ranging from 1 nm to 20 nm. Closer inspection of DF micrograph reveals numerous small crystals, 1-2 nm in diameter, throughout the material, and also many nanocrystals with diameters greater than 10 nm. Confirmation of bubbles in BF image is demonstrated by Figs. 36(a) and 36(b), which are under-focused and over-focused BF micrographs, respectively. In under-focused images, bubbles will show as dark spots and in over-focused images, bubbles will show as white spots with fringes, which is exactly what we see here.

The calculated lattice spacings (d-spacings) extracted from SAD are shown in Table I along with d-spacings and planar indicies for $Cu_{10}Zr_7$, $CuZr_2$, and $NiZr_2$

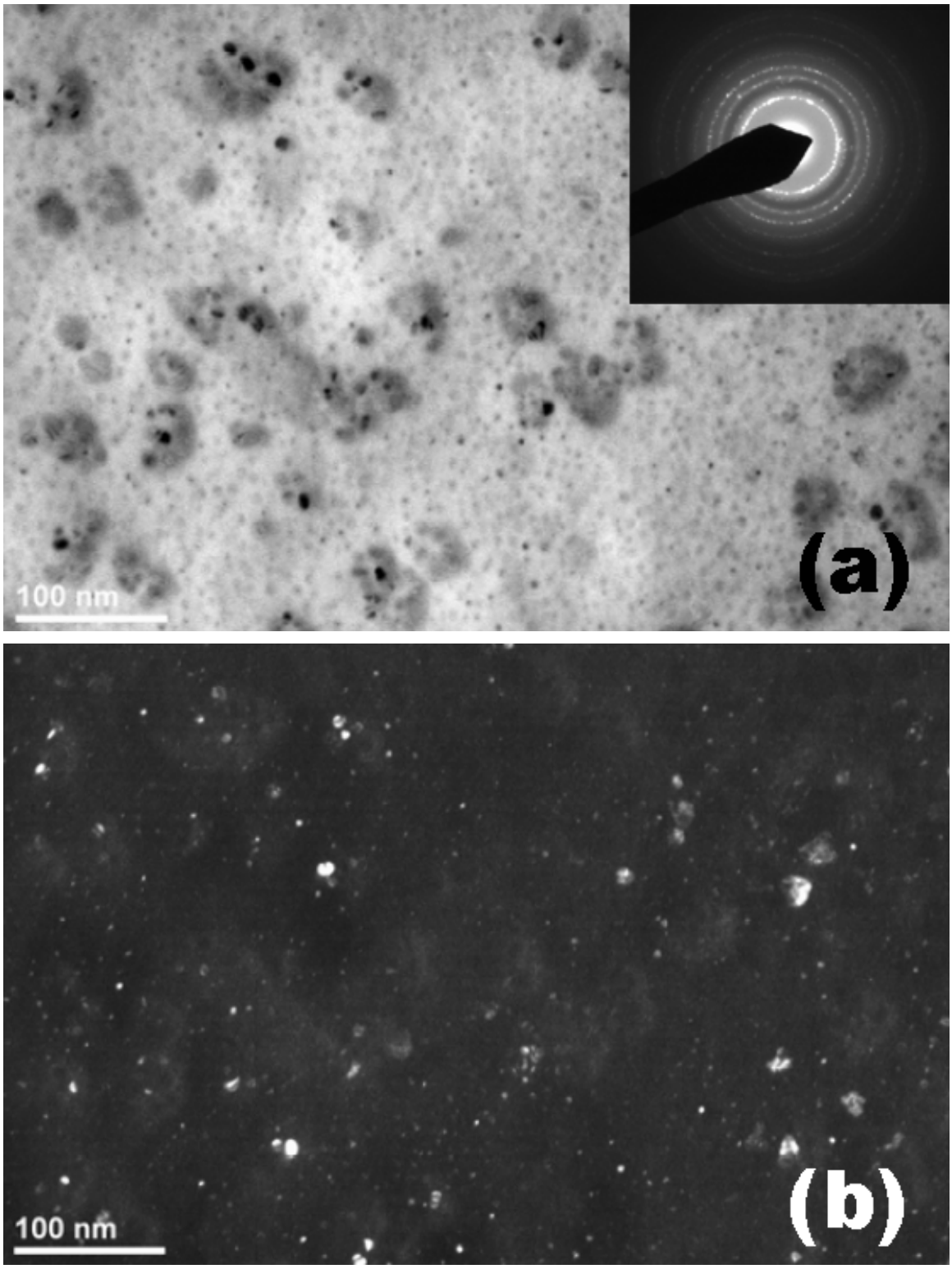

Fig. 35. TEM micrographs of 140 keV He irradiated $Zr_{55}Cu_{30}Al_{10}Ni_5$ as seen in (a) bright field, with diffraction pattern as inset, and (b) dark field.

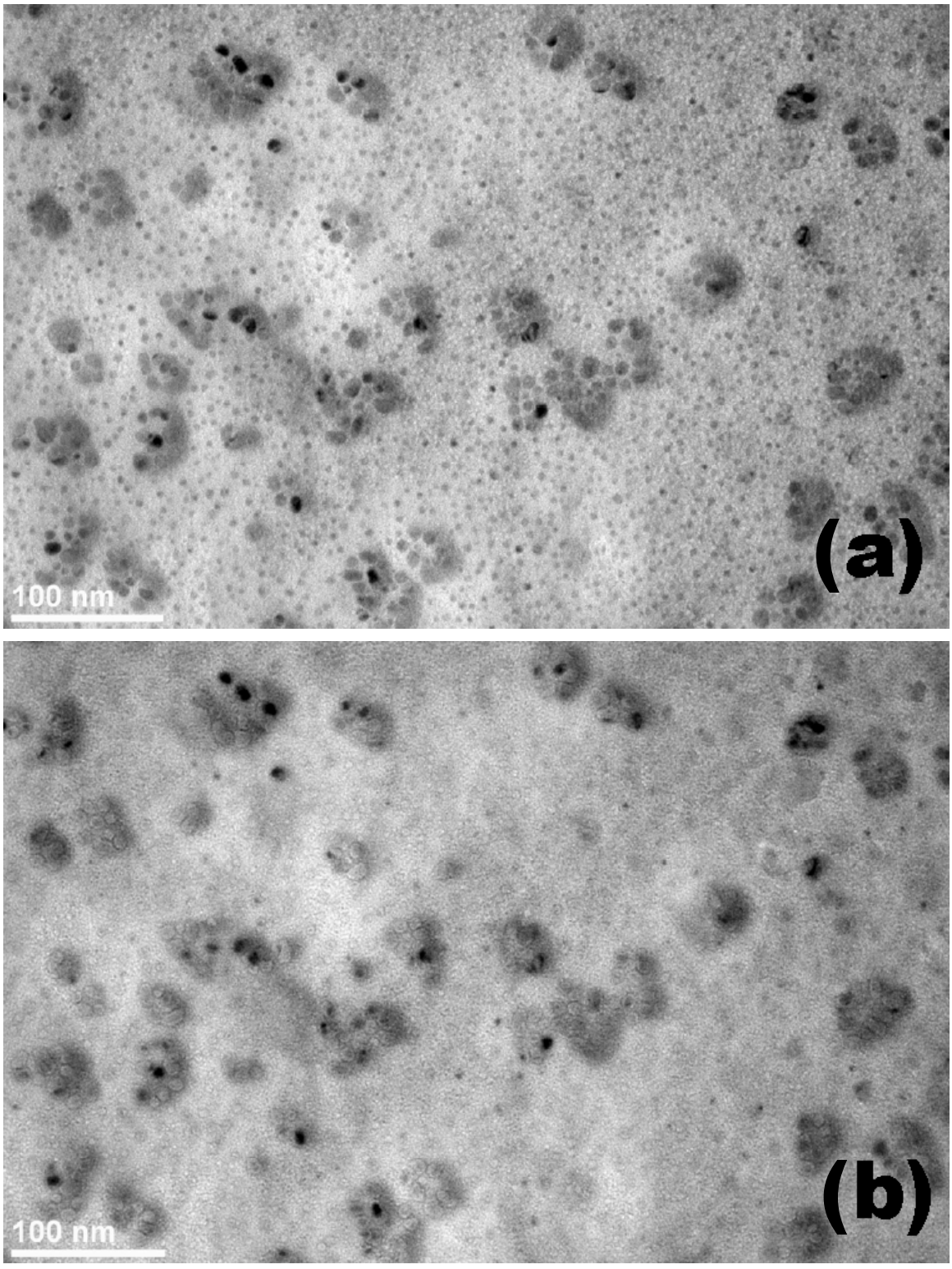

Fig. 36. Bright-field TEM micrographs of 140 keV He irradiated $Zr_{55}Cu_{30}Al_{10}Ni_5$ specimens. Images are shown as (a) under-focused and (b) over-focused to show bubbles.

intermetallics [63, 64, 65]. The calculated d-spacing of 3.1735 Å can be exclusively assigned to the (004) lattice plane in $Cu_{10}Zr_7$, along with 2.6213 Å, 1.9233 Å, and others. This verifies that the $Cu_{10}Zr_7$ phase exists in the irradiated glass. Likewise the values 2.782 Å and 2.269 Å can be assigned to the (004) plane in $CuZr_2$, among others, verifying the $CuZr_2$ phase in the irradiated specimen. However, one cannot rule out the $NiZr_2$ phase since it lattice spacings are so similar to values seen in both $Cu_{10}Zr_7$ and $CuZr_2$. This shows that $Zr_{55}Cu_{30}Al_{10}Ni_5$ metallic glass contains a mixture of $Cu_{10}Zr_7$ and $CuZr_2$ phases after irradiation with the possibility of a $NiZr_2$ phase.

Annealing studies on $Zr_{55}Cu_{30}Al_{10}Ni_5$ have shown that $Cu_{10}Zr_7$ and $CuZr_2$ crystal structures can nucleate in the glass [66], and that $NiZr_2$ can form in $Zr_{52}Ti_5Cu_{18}Ni_{15}Al_{10}$ metallic glass [67], a composition similar to the one in this study. It is also worth noting that the $CuZr_2$ phase was seen in electron irradiation experiment in a similar Zr-Cu based metallic glasses [68]. These studies point to the co-existence of both $CuZr_2$ and $NiZr_2$ in the irradiated glass. Noting the similar electronegativity of Ni and Cu (1.8 and 1.9) and similar atomic radius (0.125 nm and 0.128 nm) as well as the similar stochiometry of both $CuZr_2$ and $NiZr_2$, it may be feasible for mutual solubility of $CuZr_2$ and $NiZr_2$. Futhermore, a single phase structure given by $(Ni_x, Cu_{1-x})\,Zr_2$ may have formed. This type of substitutional structure can be seen in other alloy systems such as Fe-Cr-Ni-Zr [69, 70].

As discussed earlier, the nanocrystal sizes seen in DF images show a bimodal distribution. One mode exists in the range of 1-2 nanometers, while the other group has a range of 10-20 nanometers. Chemical analysis of the crystals was not performed in this experiment but it is unlikely that the large diameter mode contains any Ni since the glass contains only 5% Ni ($Zr_{55}Cu_{30}Al_{10}Ni_5$). The large crystals likely contain $Cu_{10}Zr_7$ and the small crystals are probably $NiZr_2$ or the substiutional $(Ni_x, Cu_{1-x})\,Zr_2$

Table I. Calculated d-spacings extracted from SAD in Fig. 35(a) of He irradiated $Zr_{55}Cu_{30}Al_{10}Ni_5$. Shown for comparison are standard d-spacings for $Cu_{10}Zr_7$, $CuZr_2$, and $NiZr_2$ phases and their respective planar indices. Values are in angstroms.

Experimental data	$Cu_{10}Zr_7$ standard d-spacing/orientation	$CuZr_2$ standard d-spacing/orientation	$NiZr_2$ standard d-spacing/orientation
3.170	3.1735/(004)		
2.887	2.8803/(311)		2.812/(331)
2.783		2.782/(004)	
2.699	2.6213/(204)		
2.249		2.269/(110)	
2.221	2.2333/(411)		
1.937	1.9233/(315)		
1.664	1.6491/(440)		
1.608	1.5976/(422)	1.607/(200)	1.594/(731)
1.382	1.3987/(346)	1.393/(204)	
1.374	1.3779/(119)		
1.287	1.2873/(517)		1.233/(933)
1.185		1.191/(118)	1.187/(951)
1.131		1.158/(109)	

structure.

The addition of nanocrystals or composite materials into metallic glasses has been shown to increase ductility while maintaining good strength [1, 24, 26, 71]. Given the distribution of nanocrystal sizes found in these irradiated glasses, ie, the bimodal size distribution, it may be possible to control the nanocrystal sizes in other irradiated specimens. With addition of minor elements, it may be possible to control nanocrystal size. With more elements, crystallization of major elements due to irradiation may be lessened since there would be fewer atoms available in the vicinity of the crystal to bond with. On the other hand, crystallization of minor elements would be hampered from the beginning since there would be fewer atoms with which to bond. This would be useful because the nanocrystal volume fraction needs to be controlled if the benefits of having nanocrystals dispersed in an amorphous matrix are to be maintained [1]. Perhaps the control of nanocrystal growth could lead to a more radiation tolerant material since the nanocrystal size would be limited by component selection.

In summary, we investigated microstructural change of $Zr_{55}Cu_{30}Al_{10}Ni_5$ in presence of 140 keV He ions to a fluence of 4×10^{17} ions/cm^2. TEM characterization of irradiated specimens revealed nanocrystals and segregations. The lattice spacings of the crystalline structures were analyzed by use of the diffraction pattern and standard spacing data. The $Cu_{10}Zr_7$ and $CuZr_2$ phases were identified and mixed with the amorphous phase. Possibly a $NiZr_2$ phase was also formed but it was unable to be distinctly indentified because its lattice spacings are so similar to $Cu_{10}Zr_7$ and $NiZr_2$. Because of the similarities between $CuZr_2$ and $NiZr_2$, we suggested the possibility of forming a substitutional $(Ni_x, Cu_{1-x})\,Zr_2$ phase in the irradiated material. Sizes of the nanocrystals represented a bimodal distribution with a large majority of crystals with 1-2 nm diameters and another majority of crystals with 10-20 nm diameters. It was suggested that the small diameter crystals are either the $NiZr_2$ phase

or $(Ni_x, Cu_{1-x})\,Zr_2$ phase because the relative abundance of Ni is so small (5%) in $Zr_{55}Cu_{30}Al_{10}Ni_5$. The large crystals are probably $Cu_{10}Zr_7$ or $CuZr_2$ due to large relative abundance of both elements.

CHAPTER VII

COPPER IRRADIATED MG1*

Our studies began with preparing $Cu_{50}Zr_{45}Ti_5$ metallic glass ribbon samples by rapid solidification. Samples were measured to be 20 μm in thickness and 1.5 mm in width. As-spun samples were irradiated with 1 MeV Cu ions to a total fluence of 1×10^{16} ions/cm^2 at room temperature using a NEC 1.7 MeV tandem accelerator. The beam current was controlled to be ~100 nA/cm^2 and the beam heating on the irradiated samples was measured to be less than 50 °C. The projected range of 1 MeV Cu in the glass is around 460 nm [49]. Samples were characterized using Bruker-AXS D8 VARIO high-resolution X-ray diffractometer. Transmission electron microscopy (TEM) and high-resolution TEM were performed by using a JEOL 2010 microscope equipped with Gatan SC1000 ORIUS CCD camera, operated at 200 kV. TEM specimens were prepared on a Fischione 1010 ion mill using 2 keV Ar ions while the sample was cooled by a liquid nitrogen cooling system. The specimens were slowly rotated during thinning to avoid inhomogeneous etching. Our recent studies have shown that the above specimen preparation procedure can avoid ion-milling-induced microstructural changes [62].

Fig. 37 shows X-ray diffraction (XRD) spectra of the as-spun and irradiated ribbon $Cu_{50}Zr_{45}Ti_5$ glasses. For the as-spun sample (gray color) a broad peak is presented, which is typical for the glassy state. For the irradiated sample (dark color), the XRD spectrum shows sharp peaks and suggests the presence of crystalline phases. Several diffraction peaks corresponding to crystallographic planes from $Cu_{10}Zr_7$ and

---

*Reprinted with permission from "Effects of Cu ion irradiation in $Cu_{50}Zr_{45}Ti_5$ metallic glass" by J. Carter, E. G. Fu, M. Martin, G. Xie, X. Zhang, Y. Q. Wang, D. Wijesundera, X. M. Wang, W. K. Chu, and L. Shao, 2009. *Scripta Materialia*, vol. 61, pp. 265-268. Copyright 2009 by Elsevier. doi:10.1016/j.scriptamat.2009.03.060

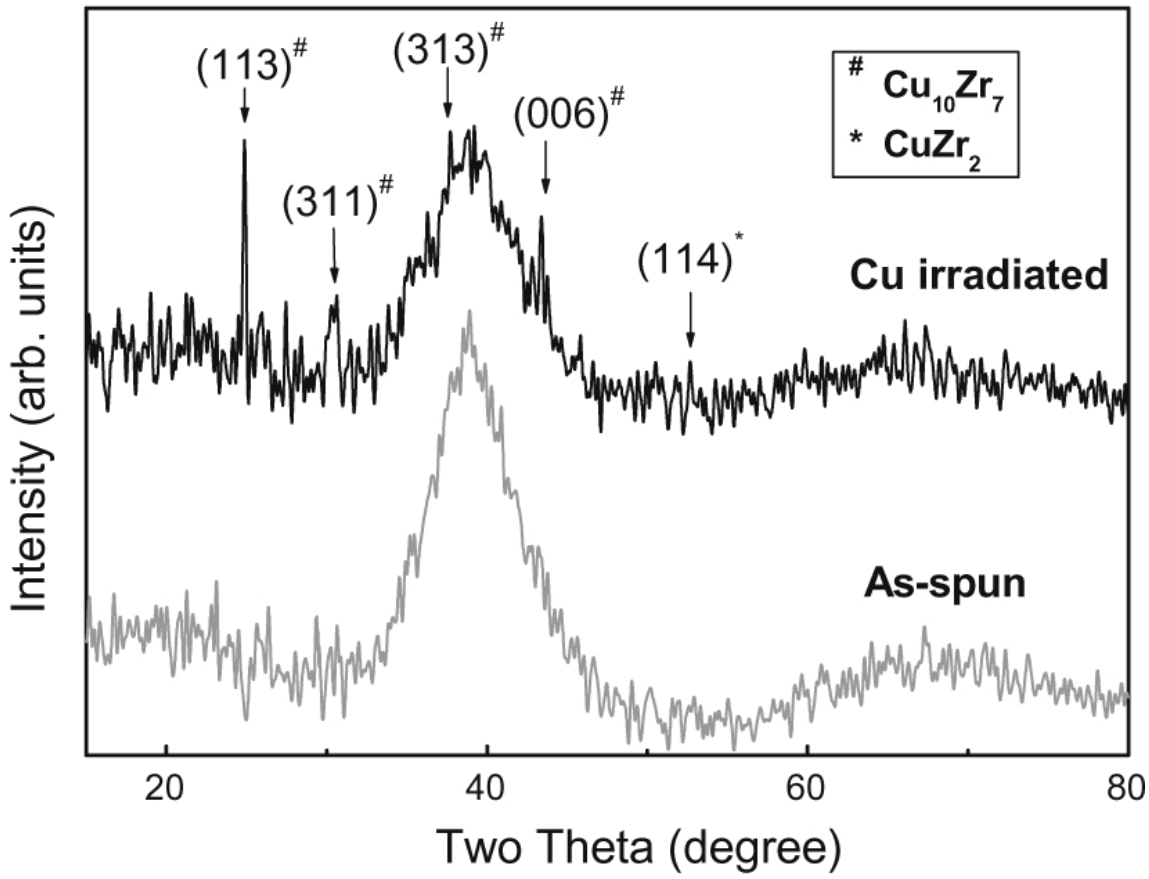

Fig. 37. XRD patterns of as-spun and Cu ion irradiated $Cu_{50}Zr_{45}Ti_5$ metallic glass. Diffraction peaks from crystalline $Cu_{10}Zr_7$ (#) and $CuZr_2$ (*) phases are marked.

$CuZr_2$ phases are marked in Fig. 37. However, TEM characterization is needed for more conclusive determination of crystalline phases since both spectra in Fig. 37 are noisy due to relatively low detection limits of XRD.

Fig. 38(a) shows a typical bright-field TEM micrograph from the Cu-irradiated sample. Precipitation and dark particles are presented. The corresponding SAD pattern shows white diffraction dots and sharp rings, indicating long-range order and the nucleation of nanocrystals. For comparison, Fig. 38(b) shows a typical dark-field TEM micrograph obtained from the same sample. It reveals the presence of nanocrystalline particles. Systematic comparison between a series of bright-field and dark-field micrographs suggests that the dark particles observed in bright-field TEM micrographs are indeed nanocrystals.

Fig. 39 plots the size distribution of nanocrystals. Nanocrystal diameters range mostly from 2 to 14 nm, with a typical size of 6 nm, though crystal diameters of ~100 nm are seen in some portions of the irradiated specimens (see figure on page 132). The inset in Fig. 39 is a high-resolution TEM micrograph of the Cu-irradiated sample. Crystalline structures inside nanoparticles are clearly visible. As we will discuss below, these nanocrystals are either $Cu_{10}Zr_7$ (primary) or $CuZr_2$ phases.

Fig. 40 shows the enlarged SAD pattern obtained from the Cu-irradiated sample. The interplanar distances calculated from the SAD pattern were compared with those from database [63, 64] and are summarized in Table II. The system was calibrated using single crystal Si (100). The extracted d-spacing values suggest the formation of $Cu_{10}Zr_7$ (primary) and $CuZr_2$ (minor) phases. Crystallographic planes from these two phases are labeled in the SAD pattern. The body-centered cubic CuZr phase with d-spacings of 2.307, 1.883, 1.631, 1.459, 1.332 and 1.153 Å, and others, could not be identified [72]. Our particular interest in CuZr phase is due to the reason that this phase is expected to form at a temperature comparable to thermal spikes [72].

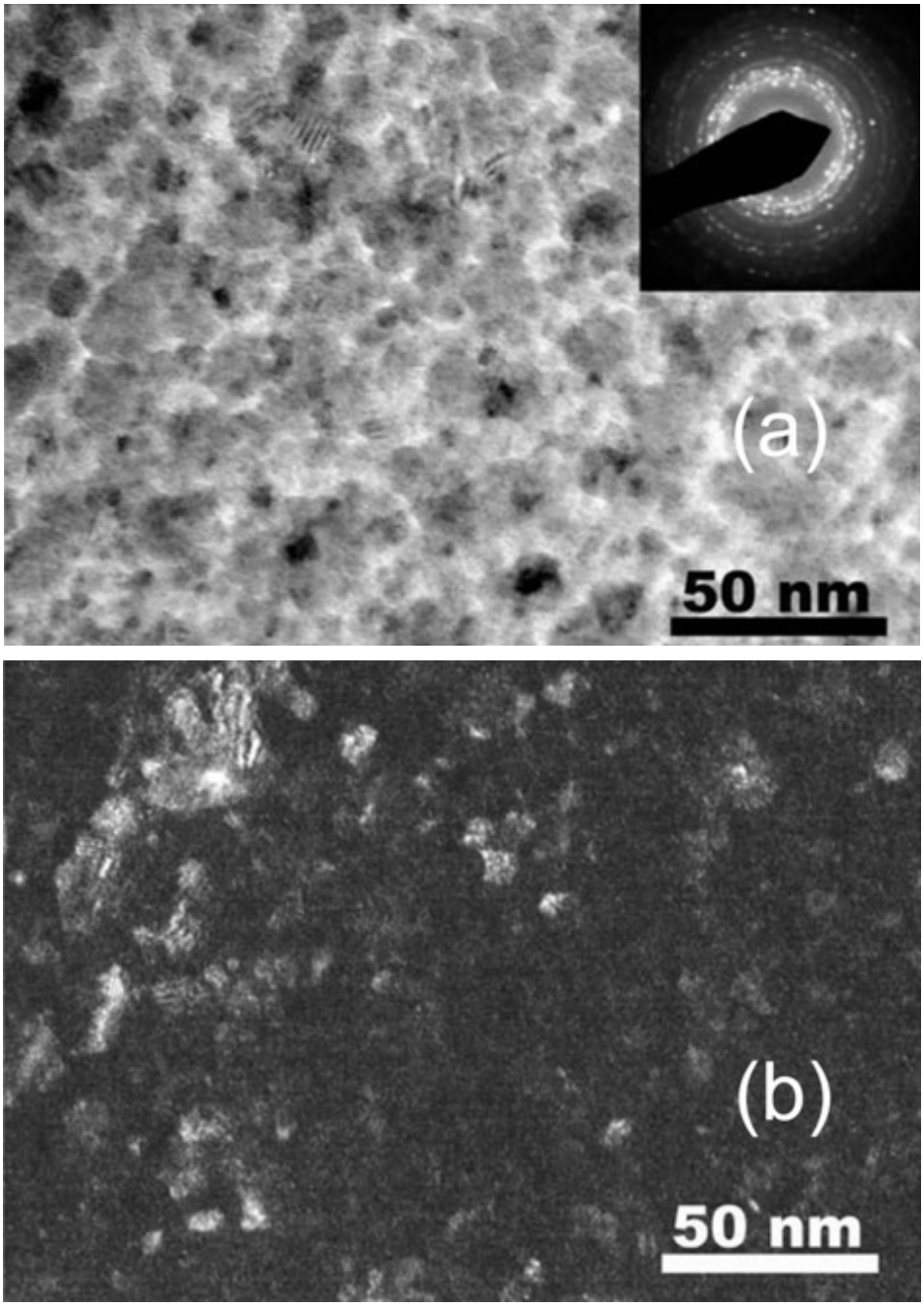

Fig. 38. (a) Bright-field TEM micrograph and the corresponding SAD pattern inset of Cu-ion-irradiated $Cu_{50}Zr_{45}Ti_5$ glass specimen, and (b) dark-field TEM micrograph of the same sample.

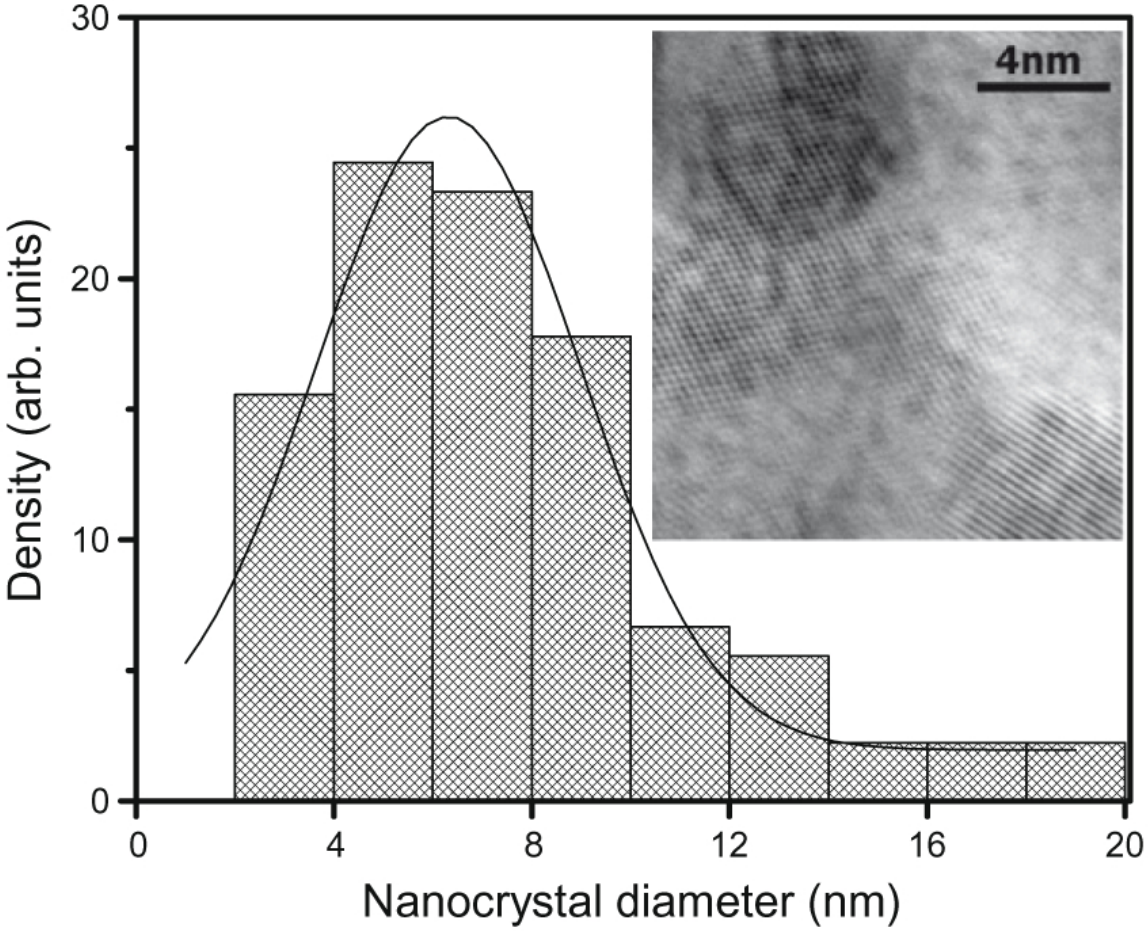

Fig. 39. Size distribution of nanocrystals in Cu ion irradiated $Cu_{50}Zr_{45}Ti_5$ estimated from TEM micrographs. The inset is a high-resolution TEM micrograph.

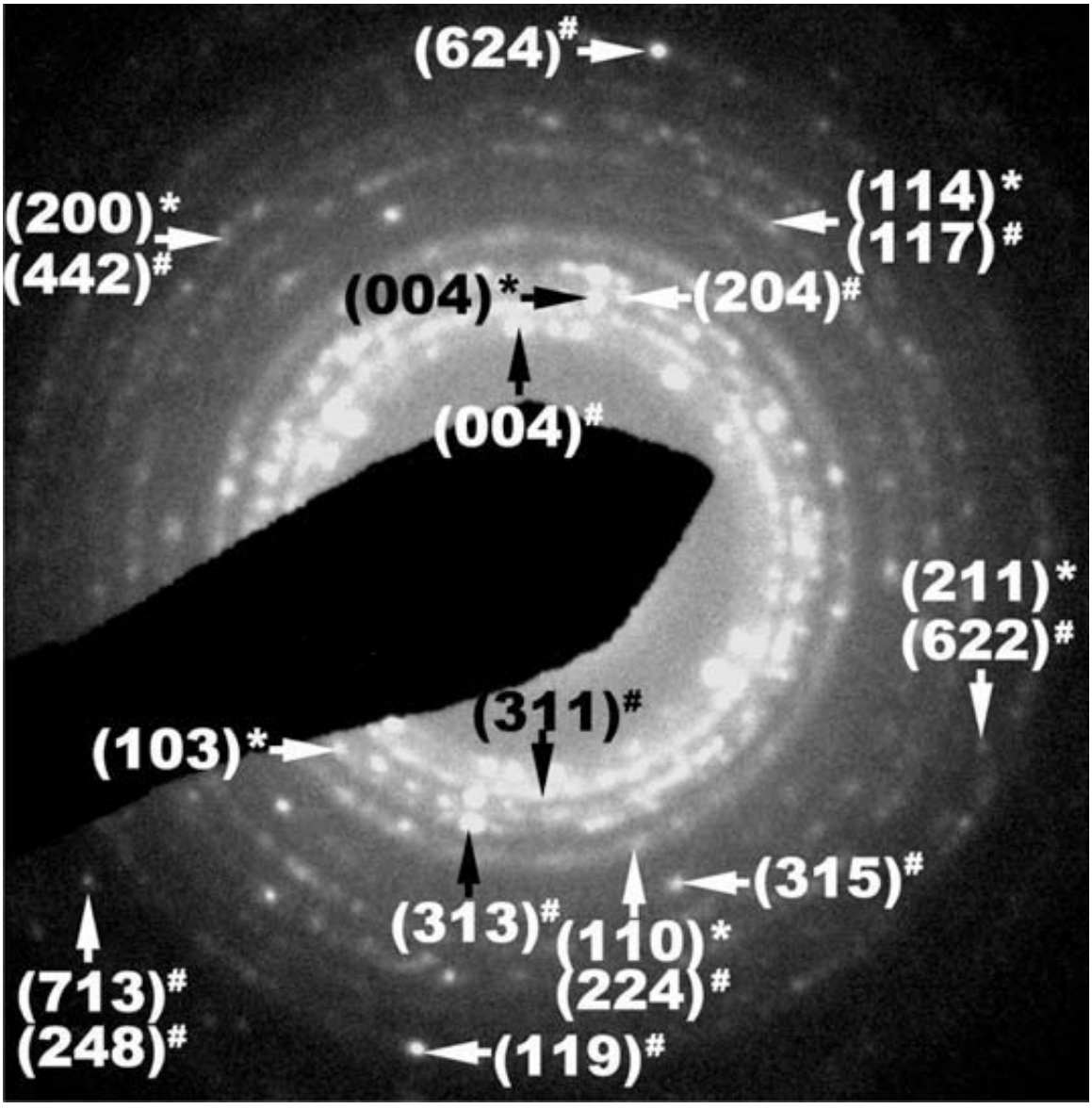

Fig. 40. The SAD pattern of Cu ion irradiated $Cu_{50}Zr_{45}Ti_5$ glass. The Miller indicies correspond to crystalline $Cu_{10}Zr_7$ (#) and $CuZr_2$ (*) phases.

Table II. Calculated d-spacings extracted from SAD in Fig. 40 of Cu irradiated $Cu_{50}Zr_{45}Ti_5$. Shown for comparison are standard d-spacings for $Cu_{10}Zr_7$ and $CuZr_2$ phases and their respective planar indices. Values are in angstroms.

Experimental data	$Cu_{10}Zr_7$ standard d-spacing/orientation	$CuZr_2$ standard d-spacing/orientation
3.178	3.1735/(004)	
2.889	2.8803/(311)	
2.755		2.782/(004)
2.642	2.6213/(204)	
2.463		2.429/(103)
2.416	2.4201/(313)	
2.252	2.2873/(224)	2.269/(110)
1.933	1.9233/(315)	
1.759	1.7461/(117)	1.761/(114)
1.603	1.5976/(422)	1.607/(200)
1.433	1.4377/(662)	1.429/(211)
1.372	1.3779/(119)	
1.260	1.2623/(248)	
1.116		1.117/(010)
1.035		1.030/(303)

Structures of $Cu_{10}Zr_7$, $CuZr_2$, and CuZr crystals are very different. $Cu_{10}Zr_7$ has a complex unit cell containing 68 atoms over nine inequivalent sites [73]. $CuZr_2$ has an $MoSi_2$-type structure with a tetragonal cell containing six atoms [37]. As the simplest structure, CuZr has a CsCl-type structure, but it is metastable at low temperature. Stable CuZr phase forms only at a temperature > 985 K [72]. In one previous study, an initially amorphous Zr_xCu_{1-x} alloy was continuously heated from low temperature to high temperature. $Cu_{10}Zr_7$ and $CuZr_2$ phases are observed but no CuZr phase can be identified [74]. In another study, if a liquid melt of Zr-Cu-Al was cooled from high temperature to low temperature, CuZr phase was observed in the region with a high cooling rate, while in the region with a low cooling rate $Cu_{10}Zr_7$ and $CuZr_2$ phases were identified [75]. Therefore, a metastable CuZr phase will form if cooling is fast. Otherwise, it will decompose into more stable $Cu_{10}Zr_7$ and $CuZr_2$ phases.

The damage cascades caused by ion irradiation will typically last for a period of 10^{-13} s. After that, a localized melting zone due to thermal spike formation is left. The highly localized heating typically lasts for a period of 10^{-12} s. Considering the critical cooling rates to form MG for Cu-Zr alloys in the range of $4.3 \times 10^2 - 3.6 \times 10^4$ K/s and, for Cu-Zr-Ti alloys, $6 \times 10^3 - 1.4 \times 10^4$ K/s [76], the quenching rate of a thermal spike is much faster than the critical cooling rate. This fact leads to the following two possibilities: (i) if damage cascades do not cause decomposition, MG in the cascade core region will keep its original composition and ultra fast quenching of a thermal spike will not lead to nanocrystal formation; (ii) if CuZr phase actually forms in the thermal spike region, the ultrafast quenching of the thermal spike should keep metastable CuZr phase (or at least part of it) at ambient temperature, according to Ref. [74]. Based on the above discussion and the fact that no CuZr phase is observed after Cu irradiation, we hypothesized that CuZr phase does not form in the damage cascade region.

Early studies by Meldrum et al. [77] have shed light into the complexity of irradiation-induced crystallization. These authors reported evidence of a transient liquid-like phase caused by displacement cascades in solids. Under high-temperature irradiation, new crystalline phases were formed in zircon. Such phases were not observed under low-temperature irradiation. The difference was explained as due to different quenching rates: a high quenching rate occurs at low ambient temperature and does not allow sufficient time for nucleation of a new phase [77]. A similar mechanism might apply in the present study, even though the materials are different.

The present study suggests that the quenching rate of thermal spike is so high that it becomes difficult to achieve short-range order in the damage cascade region. In order to form a nucleation site, the magnitude of the necessary diffusion coefficient within the displacement cascade region can be estimated by $D = x^2/t$. If $x \approx 1$ nm and $t \approx 1$ ps, then $D = 1 \times 10^{-6}$ m^2/s. It is unlikely that the atomic diffusivity of $Cu_{50}Zr_{45}Ti_5$ at thermal spike temperatures can be that high, considering groups of atoms need to jump collectively [78]. Recently, self-diffusion in a binary $Cu_{33}Zr_{67}$ glass has been modeled by molecular dynamics simulation [79]. It shows that, at a melting temperature of 2000 K, Cu diffusivity is 4×10^{-9} m^2/s, which is a few orders of magnitude lower than the above-estimated diffusivity to form the necessary solute segregation. Although $Cu_{33}Zr_{67}$ is different from the $Cu_{50}Zr_{45}Ti_5$ studied here, both materials have similar packing density and nearest atomic distance, and their self-diffusion coefficients should be comparable.

Recently, the mechanism of shear-band-formation-induced nanocrystallization has been investigated [58]. The phenomenon is different from what happens in ion irradiation. The amount of energy deposited by shear band formation is much larger, the energy dissipation takes longer and the region being heated is wider [58]. Thus, nanocrystals can be formed in the vicinity of the shear bands. As discussed in the

preceding paragraphs, fast quenching of the thermal spike in ion irradiated samples makes correlated atomic movements difficult. Rather than directly causing phase transformation, quenching spreads excessive free volume over a large region. This enhances atomic mobility and leads to increased short-range order and subsequent nucleation at longer times.

For applications, ion irradiation can be used as a method to improve materials' mechanical properties. Since irradiation temperature, implanted ion species, ion energy, ion flux, and fluence can be well controlled, the technique can achieve adjustable nanocrystallization and increase both hardness and ductility of MGs with high repeatability. In addition, ion implantation of impurities into MG can increase thermodynamic stabilities. One previous study has shown that implantation of Co into ZrCuNiAl alloy can lower its glass transition temperature and enlarge the supercooled liquid range [80]. Introducing impurities is expected to also increase nucleation sites. Since the activation energy for nucleation is usually larger than the activation energy for crystal growth in metallic glasses [57], a technique combining ion implantation to introduce nucleation sites and annealing to induce nanocrystal growth might achieve optimized nanocrystallization at low temperatures. However, ion implantation is a surface modification technique. The structural changes are limited by ions' penetration depth. Thus, the technique is useful to improve surface properties but has its limitation to improve MG's machinability.

In summary, 1 MeV Cu ion irradiation of $Cu_{50}Zr_{45}Ti_5$ metallic glass was found to induce nanocrystalline $Cu_{10}Zr_7$ and $CuZr_2$ phases. However, the CuZr phase, a decomposition product expected with high-temperature annealing, is not observed after ion irradiation. The study suggests that nanocrystal formation is due to enhanced atomic mobility caused by the introduction of excessive free volume brought on by ion irradiation. It seems unlikely that the decomposition is due to a localized

structural transformation in the damage cascade and thermal spike region.

CHAPTER VIII

COPPER IRRADIATED MG2*

The $Zr_{55}Cu_{30}Al_{10}Ni_5$ metallic glass ribbon samples used in this study were prepared by rapid solidification and are approximately 20 μm thick and 1.5 mm wide. The 1 MeV Cu ion irradiation was performed to a fluence of 1×10^{16} ions/cm^2 using a NEC 1.7 MeV tandem accelerator. The beam flux was 6.3×10^{10} ions/cm^2 – s and the sample's temperature rise during ion irradiation is measured to be less than 50°C. No annealing was performed after irradiation. The samples were characterized before and after irradiation by X-ray diffraction (XRD), transmission electron microscopy (TEM), and high resolution transmission electron microscopy (HRTEM). XRD analysis used a Bruker-AXS D8 VARIO high resolution X-ray diffractometer. The TEM and HRTEM were performed using a 200 kV JEOL 2010 microscope equipped with Gatan SC1000 ORIUS CCD camera. TEM specimen preparation was done on a Fischione 1010 ion mill using 2 keV Ar ions and sample cooling with a liquid nitrogen cooling system. The specimens were slowly rotated during thinning to avoid inhomogeneous etching. Furthermore, each TEM image was taken with minimal electron irradiation. Our recent studies have shown that the above specimen preparation procedure is necessary to avoid ion milling and electron irradiation induced microstructural changes [62].

Fig. 41 shows a bright-field TEM micrograph and corresponding selected area diffraction (SAD) pattern from the as-spun $Zr_{55}Cu_{30}Al_{10}Ni_5$ ribbon. No trace of crystalline phases and precipitations are found. The SAD pattern has wide halo rings

*Reprinted with permission from "Ion irradiation induced nanocrystal formation in amorphous $Zr_{55}Cu_{30}Al_{10}Ni_5$ alloy" by J. Carter, E. G. Fu, M. Martin, G. Xie, X. Zhang, Y. Q. Wang, D. Wijesundera, X. M. Wang, W. K. Chu, S. M. McDeavitt, and L. Shao, 2009. *Nuclear Instruments and Methods in Physics Research B.* Copyright 2009 by Elsevier. doi:10.1016/j.nimb.2009.05.068

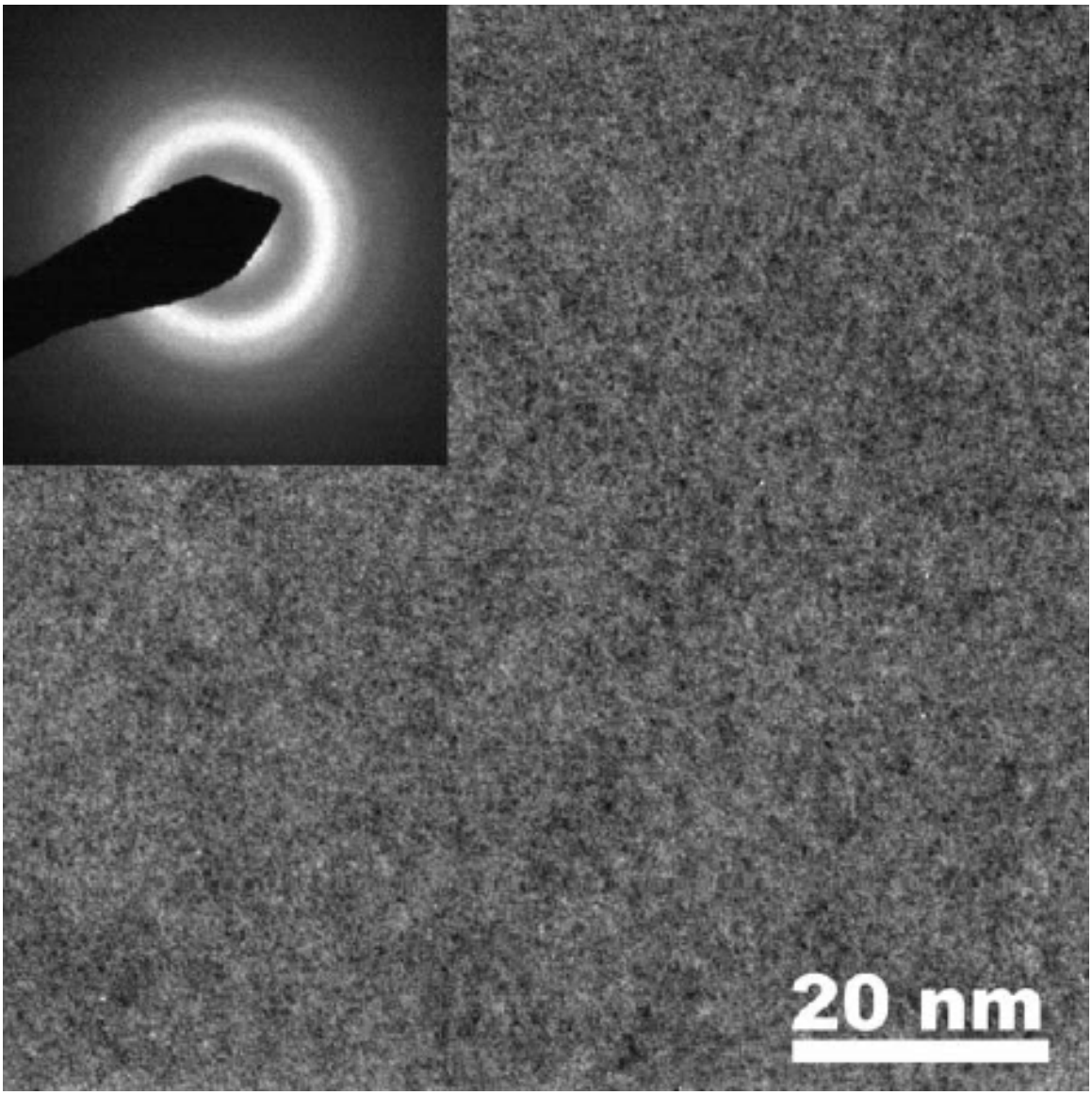

Fig. 41. Bright-field TEM micrograph of as-spun $Zr_{55}Cu_{30}Al_{10}Ni_5$ glass and the corresponding SAD pattern.

without spots, which is a typical characteristic of amorphous material. Differential scanning calorimetry measurements (not shown here) on the as-spun sample also reveal a typical annealing behavior of MG with glass transition at 697 K and first-step crystallization at 762 K.

Fig. 42 shows XRD spectra of the as-spun and irradiated ribbon $Zr_{55}Cu_{30}Al_{10}Ni_5$ glasses. The as-spun sample shows a broad peak and confirms its glassy state. After ion irradiation, this broad peak becomes narrower and the peak shifts and splits as it becomes more defined, which suggests the development of a more ordered structures. The XRD spectrum from the irradiated sample clearly shows sharp diffraction peaks superimposed on the broad amorphous peak. This suggests the existence of crystalline phases. As marked in Fig. 42, the sharpest peaks can be assigned to $Cu_{10}Zr_7$ and $NiZr_2$ phases. Further determination of crystalline phases by using TEM will be discussed later.

Figs. 43(a) and 43(b) show bright-field and dark-field TEM images, respectively, from the sample after 1 MeV Cu ion irradiation (fluence = 1×10^{16} ions/cm^2). The prominent features observed in these images represent a dispersion of small crystalline particles, which is a dramatic contrast to the featureless amorphous alloy shown in Fig. 41. In Fig. 43(a), small particles with a typical size of 5-10 nm and large particles with a typical size of 50-100 nm are observed. In the corresponding dark-field TEM image in Fig. 43(b), both small and large particles show crystallinity.

Fig. 44 is a high resolution TEM image from the irradiated sample, revealing the nanocrystal formations in the glassy matrix in greater detail. It is important to note that no preferential crystalline orientations are observed. The inset shows an inverse fast Fourier transform (FFT) of the image from the region marked by dashed lines. The ordered crystalline structure is clearly visible. Fig. 45 shows an enlarged selected area diffraction (SAD) pattern for the TEM image obtained

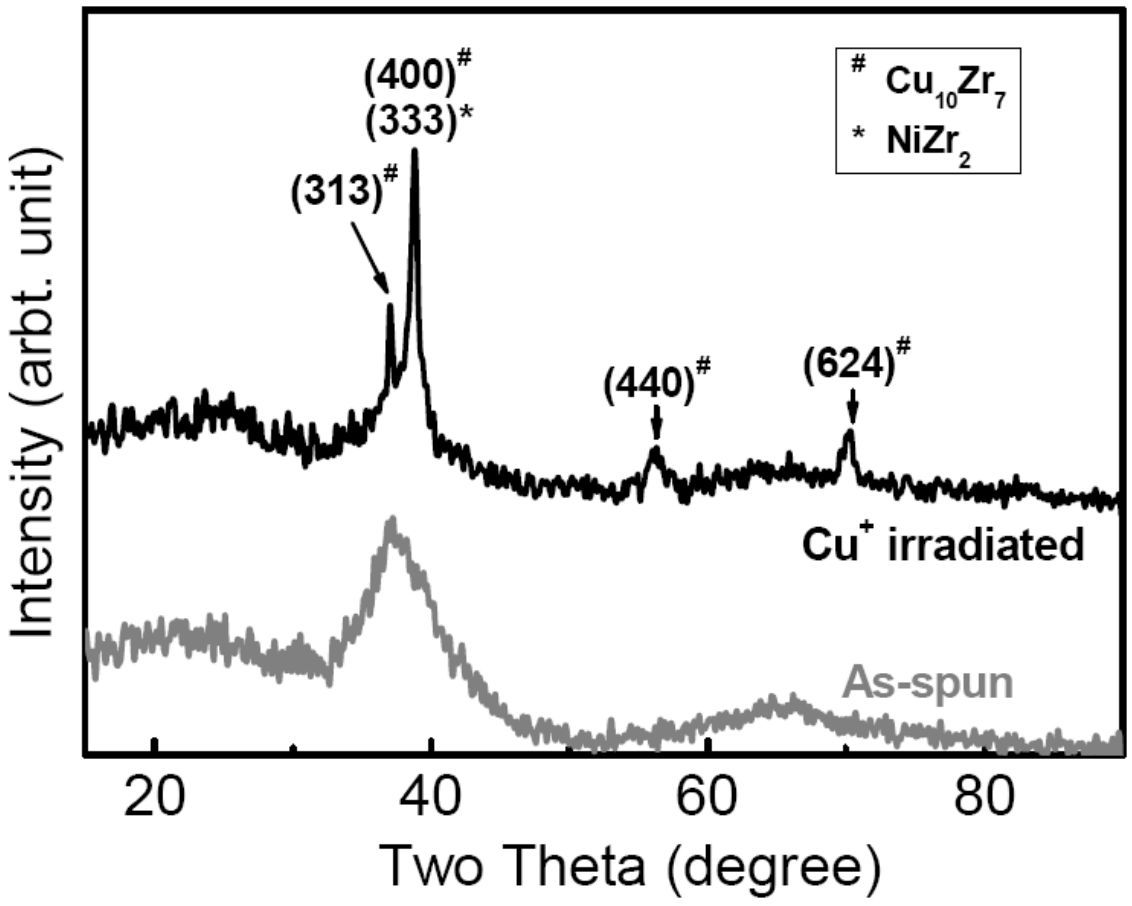

Fig. 42. XRD patterns of as-spun and Cu ion irradiated $Zr_{55}Cu_{30}Al_{10}Ni_5$ glass. Diffraction peaks from crystalline $Cu_{10}Zr_7$ (#) and $NiZr_2$ (*) phases are marked.

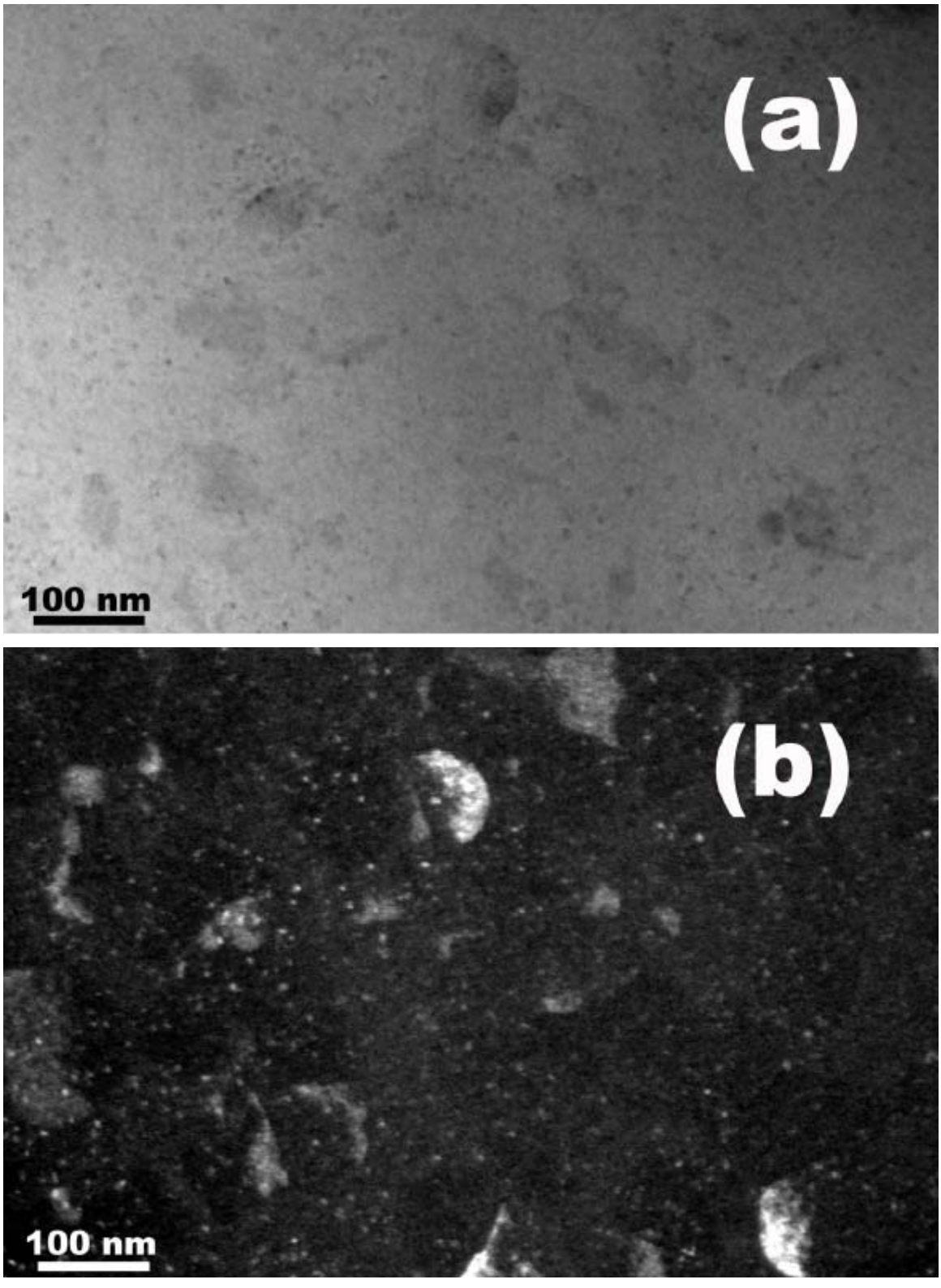

Fig. 43. (a) Bright-field TEM micrograph and (b) dark-field TEM micrograph of the Cu-ion irradiated $Zr_{55}Cu_{30}Al_{10}Ni_5$ glass.

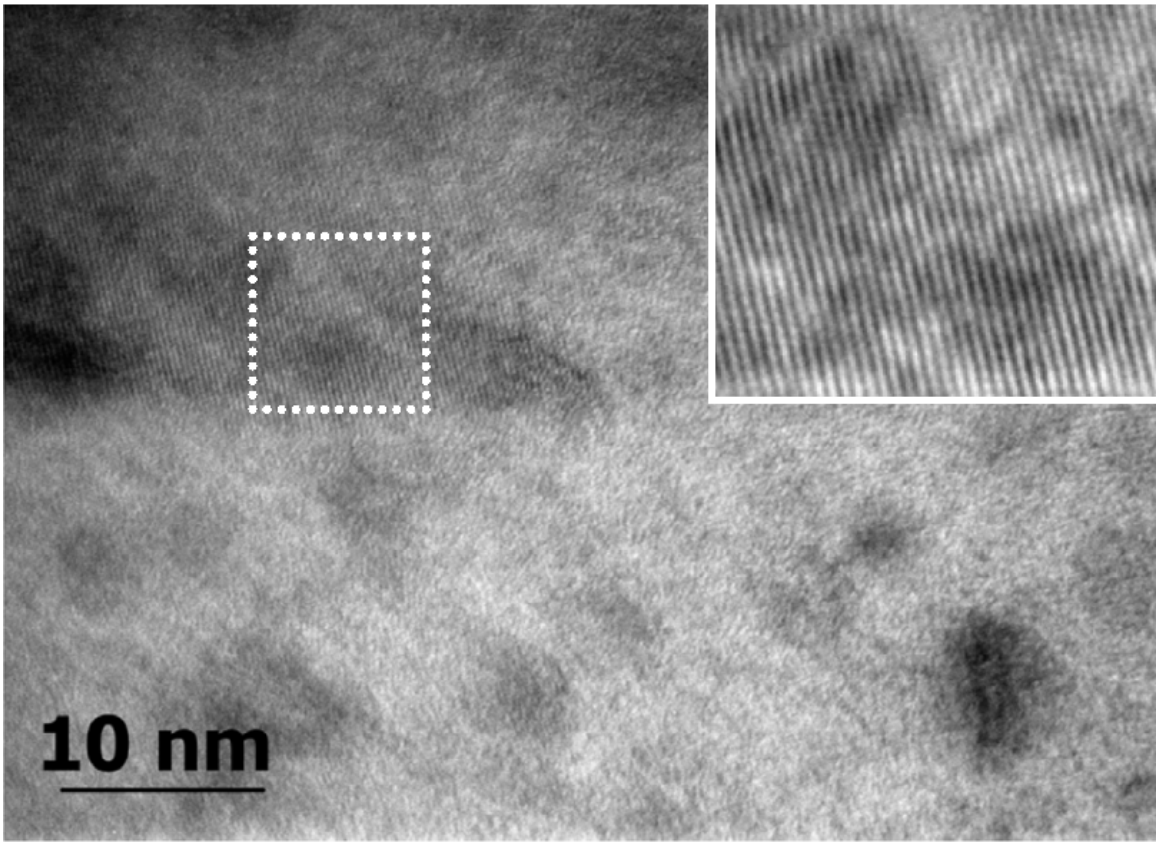

Fig. 44. High resolution TEM micrograph of Cu-ion-irradiated $Zr_{55}Cu_{30}Al_{10}Ni_5$ glass.

from the irradiated sample. Multiple interplanar distances were calculated based on diffraction points observed in this SAD pattern and these spacings were compared with a diffraction database [63, 64, 65]. The calculation considered instrument errors (~6 %) by using a pure single crystal Si (100) sample for calibration.

Table III summarizes the calculated lattice spacings (d-values) compared with corresponding d-values and planar indices that would be present if $Cu_{10}Zr_7$, $NiZr_2$ or $CuZr_2$ had formed. The calculated d-spacing of 2.636 Å can be exclusively assigned to the (204) plane from $Cu_{10}Zr_7$. Thus, the observed crystalline phases in Figs. 43 and 44 should include $Cu_{10}Zr_7$. This observation is strengthened by the calculated d-values at 2.890 Å and 1.280 Å which correspond more closely with the $Cu_{10}Zr_7$ phase than the $NiZr_2$ or $CuZr_2$, respectively. The calculated d-values between 1.411 Å and 1.759 Å correspond closely with database d-values for all three compounds: $Cu_{10}Zr_7$, $NiZr_2$ and $CuZr_2$ with no clear distinction in favor of one phase over the other. The calculated d-values between 0.948 Å and 1.205 Å as well as 2.489 Å may be related to lattice planes from $NiZr_2$ and $CuZr_2$ with no clear distinction in favor of one phase over the other. Therefore, we can declare with certainty that the $Cu_{10}Zr_7$ intermetallic has formed within the irradiated metallic glass samples. Further, the additional d-spacings that could only arise from the presence of $NiZr_2$ or $CuZr_2$ indicate that the observed crystals are a mixture of $Cu_{10}Zr_7$ with $NiZr_2$ or $CuZr_2$ or both phases. These phases agree with those seen in previous chapters (see Tables I and II).

Stability studies on electron irradiated Zr-based MG have shown that $CuZr_2$ is a common stable decomposition product in Zr-Cu metallic glasses [68]. Further, studies on behavior of thermally annealed $Zr_{52}Ti_5Cu_{18}Ni_{15}Al_{10}$ MG have observed the formation of $NiZr_2$ phase [67]. The observations noted above of crystalline planes from either $NiZr_2$ or $CuZr_2$ phases are consistent with these early studies. In fact,

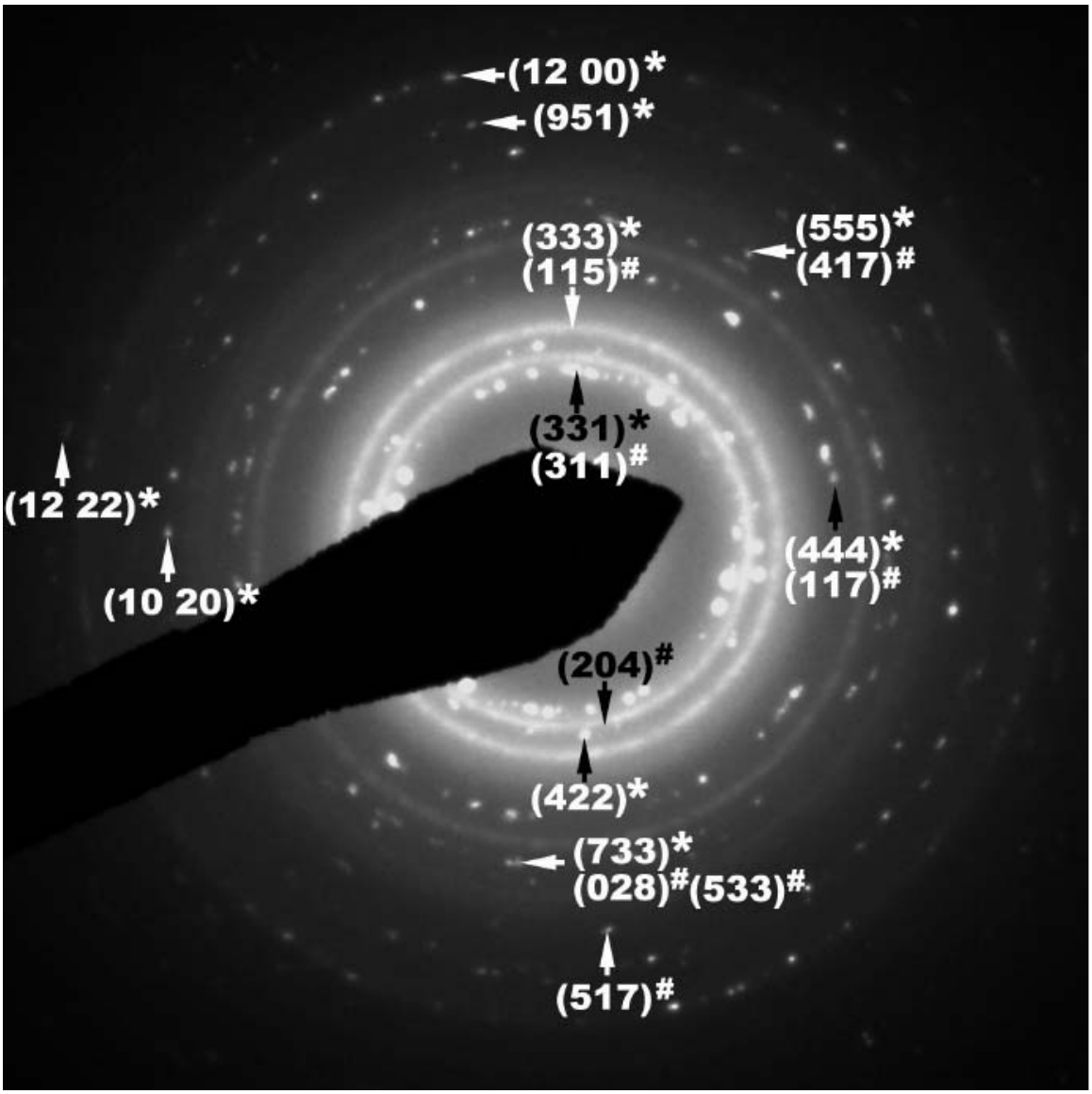

Fig. 45. The SAD pattern of Cu-ion-irradiated $Zr_{55}Cu_{30}Al_{10}Ni_5$ glass. The indexing indicates the co-existence of $Cu_{10}Zr_7$ (#) and $NiZr_2$ (*) phases.

Table III. Calculated d-spacings extracted from SAD in Fig. 45 of Cu irradiated $Zr_{55}Cu_{30}Al_{10}Ni_5$. Shown for comparison are standard d-spacings for $Cu_{10}Zr_7$, $CuZr_2$, and $NiZr_2$ phases and their respective planar indices. Values are in angstroms.

Experimental data	$Cu_{10}Zr_7$ standard d-spacing/orientation	$CuZr_2$ standard d-spacing/orientation	$NiZr_2$ standard d-spacing/orientation
2.890	2.880/(311)	2.812/(331)	
2.636	2.621/(204)		
2.489		2.503/(422)	2.429/(103)
2.326	2.366/(115)	2.360/(333)	
1.759	1.746/(117)	1.767/(444)	1.761/(114)
1.496	1.499/(028)	1.498/(733)	1.441/(116)
1.411	1.416/(417)	1.420/(555)	1.429/(211)
1.280	1.287/(517)		1.219/(206)
1.205		1.203/(1020)	1.191/(118)
1.179		1.187/(951)	1.158/(109)
1.039		1.021/(1200)	1.030/(303)
0.948		0.995/(1222)	0.941/(219)

the similarity between Ni and Cu in electronegativity (1.8 and 1.9) and atomic radius (0.125 nm and 0.128 nm) coupled with the similar stoichiometry of $NiZr_2$ and $CuZr_2$ and tetragonal structures may imply the mutual solubility of $NiZr_2$ and $CuZr_2$. This would imply that a single phase structure with a structure similar to $(Ni_x, Cu_{1-x})\,Zr_2$ may have formed. This type of substitutional intermetallic structure is commonly observed in Fe-Cr-Ni-Zr alloy systems, where $Zr(Fe_x,Cr_y,Ni_z)_2$ and $(Fe_x,Cr_y,Ni_z)Zr_2$ ($x + y + z = 1$) intermetallics have been characterized [69, 70].

It is interesting to note that the monoclinic CuZr phase was not observed here, even though it has the simplest CsCl-type structure. This is because CuZr is thermodynamically unstable at room temperature [37]. Stable CuZr phases do form at a high temperature (> 985 K) [72] and if the cooling rate is high enough, they may avoid decomposition and exist at low temperatures. Otherwise, they are known to decompose into $Cu_{10}Zr_7$ and $CuZr_2$ phases [75]. The $Cu_{10}Zr_7$ has a complex unit cell containing 68 atoms [73]. Although its formation requires highly correlated atomic movements, the required kinetics for nucleation are apparently favorable since this phase was frequently observed in thermal annealing of Cu-Zr system [74].

All of these observations, taken together, point to the formation of two crystalline intermetallic phases within the irradiated metallic glass structure: $Cu_{10}Zr_7$ and $(Ni_x, Cu_{1-x})\,Zr_2$. As shown in Fig. 43, the nanocrystals in the $Zr_{55}Cu_{30}Al_{10}Ni_5$ MG irradiated in this study have a distinctive bi-modal size distributions. One group has a nominal size range of 5 to 10 nm whereas the second has a range from 50 to 100 nm. While the chemical composition of the two different crystallite groups was not determined for this paper, it is unlikely that the large crystals contain a significant quantity of Ni, since it is a minority element in $Zr_{55}Cu_{30}Al_{10}Ni_5$. Following this logic, it is possible to hypothesize that the larger crystal may be the $Cu_{10}Zr_7$ phase and the smaller crystals may be the $(Ni_x, Cu_{1-x})Zr_2$ phase, but a more

detailed characterization is required to make this a definitive conclusion.

Even so, the most important point for the moment is that our study shows clear evidence that ion irradiation does indeed induce nanocrystal formations in $Zr_{55}Cu_{30}Al_{10}Ni_5$ glass. Metallic glasses are metastable at room temperature and crystallization occurs when energy is provided. Our results clearly demonstrate that ion irradiation can influence the crystallization process, which is governed by nucleation and crystal growth mechanism that are enhanced by increasing atomic mobilities. During ion irradiation, displacement creation by energetic particles creates vacancy defects, which increases the free volume within the system, thus enhancing atomic mobility. In addition, the amount of energy loss by the particle will change into local heating, which also contributes to increased atomic mobility. Thus, ion irradiation will enhance chemical decomposition and periodic composition fluctuations and lead to nucleation site formation.

Our finding is in contrast to that by Nagata et al. [81], who reported that ion irradiation of the same alloy at room temperature did not cause any noticeable changes. In their studies, the Cu ion energy was 350 keV and the ion fluence was 4×10^{16} ions/cm^2. In our study, the Cu ion energy was 1 MeV and the ion fluence was 1×10^{16} ions/cm^2. According to the Stopping and Range of Ions in Matter calculation [49], the total displacements per ion for 350 keV Cu is 6.4×10^3 and for 1 MeV Cu, 1.4×10^4. Multiplied by ion fluencies, the total displacements for the previous and present studies are 2.6×10^{20} displacements/cm^2 and 1.4×10^{20} displacements/cm^2, respectively. Thus, the displacement creation is comparable in both studies. It is not clear to us why these two studies lead to opposite conclusions. However, it is important to point out that in the Nagata study, only X-ray diffraction was used to characterize the irradiated samples. Considering XRD's relatively high detection limits, determination of nanocrystalline phases could be difficult without further analysis

using the TEM and SAD techniques employed in this study.

Introducing nanocrystals in MGs can enhance their ductility, but both crystal size and density must be optimized [1]. Although low temperature annealing can form bulk nanocrystalline alloys, this technique is difficult in bulk MGs due to the large exothermic heat of crystallization generated inside the alloy [82]. In other words, using annealing to induce partial crystallization in bulk MGs is impossible because it lacks any sort of control. Ion irradiation can be used as a surface modification technique with high repeatability. Although the modification is limited by the ion's penetration depth, high energy light ion irradiation or electron irradiation can be used to penetrate deeply.

In summary, we investigated structural changes of $Zr_{55}Cu_{30}Al_{10}Ni_5$ metallic glass upon irradiation with 1 MeV Cu ions to a fluence of 1.0×10^{16} ions/cm^2. Post irradiation characterization using TEM reveals nanocrystal formation and SAD analysis suggests that the nanocrystalline phases are a mixture of $Cu_{10}Zr_7$, $NiZr_2$ and $CuZr_2$ phases with the possible formation of a substitutional intermetallic $(Ni_x, Cu_{1-x})\,Zr_2$ phase. In addition, the observed nanocrystals have a distinctive bimodal size distributions. Small nanocrystals with typical sizes ranging from 5 to 10 nm and large nanocrystals with typical sizes ranging from 50 to 100 nm are observed. These findings are different from a previous study which reported no structural changes upon ion irradiation of the same alloy.

CHAPTER IX

ARGON IRRADIATED MG1

Ribbon samples of $Cu_{50}Zr_{45}Ti_5$ metallic glass were prepared by rapid solidification of metallic liquid on a copper roller. Samples have a thickness of 20 μm and a width of 1.5 mm. The microstructure of $Cu_{50}Zr_{45}Ti_5$ was characterized by Bruker-AXS D8 VARIO high resolution X-ray diffractometer (XRD). Transmission electron microscopy (TEM) and high resolution TEM (HRTEM) were performed on a JEOL 2010 microscope equipped with Gatan SC1000 ORIUS CCD camera, operated at 200 kV. Elemental analysis was carried out by an Oxford Instruments ATW type energy dispersive X-ray (EDX) detector with INCA Energy TEM platform. TEM specimens were prepared by two methods. One method used electropolishing at 243 K in a twin jet thinning electropolisher with a solution of 25% nitric acid and 75% methanol. Another method used Ar ion milling with and without liquid nitrogen cooling. Acceleration voltages of 2 kV, 3 kV, and 4 kV were used during Ar ion milling in a Fischione 1010 tabletop system. The specimens were slowly rotated by a DC motor during thinning to avoid inhomogeneous etching. Differential scanning calorimetry (DSC) measurements were performed under a purified argon atmosphere in a TA Instruments DSC-Q1000 calorimeter with finned air cooling system.

Fig. 46 shows an X-ray diffraction (XRD) spectrum of the as-spun ribbon $Cu_{50}Zr_{45}Ti_5$ glass. Only a broad peak is presented. The absence of sharp peaks suggests that there is no long range order in the as-spun material. Fig. 47 shows a DSC curve for the as-spun $Cu_{50}Zr_{45}Ti_5$ sample. DSC was performed at a heating rate of 0.33 K/s. The transition from glass to supercooled liquid occurs at a temperature of 630 K. The crystallization occurs at a temperature of 720 K. The curve demonstrates typical annealing behavior of metallic glasses [33].

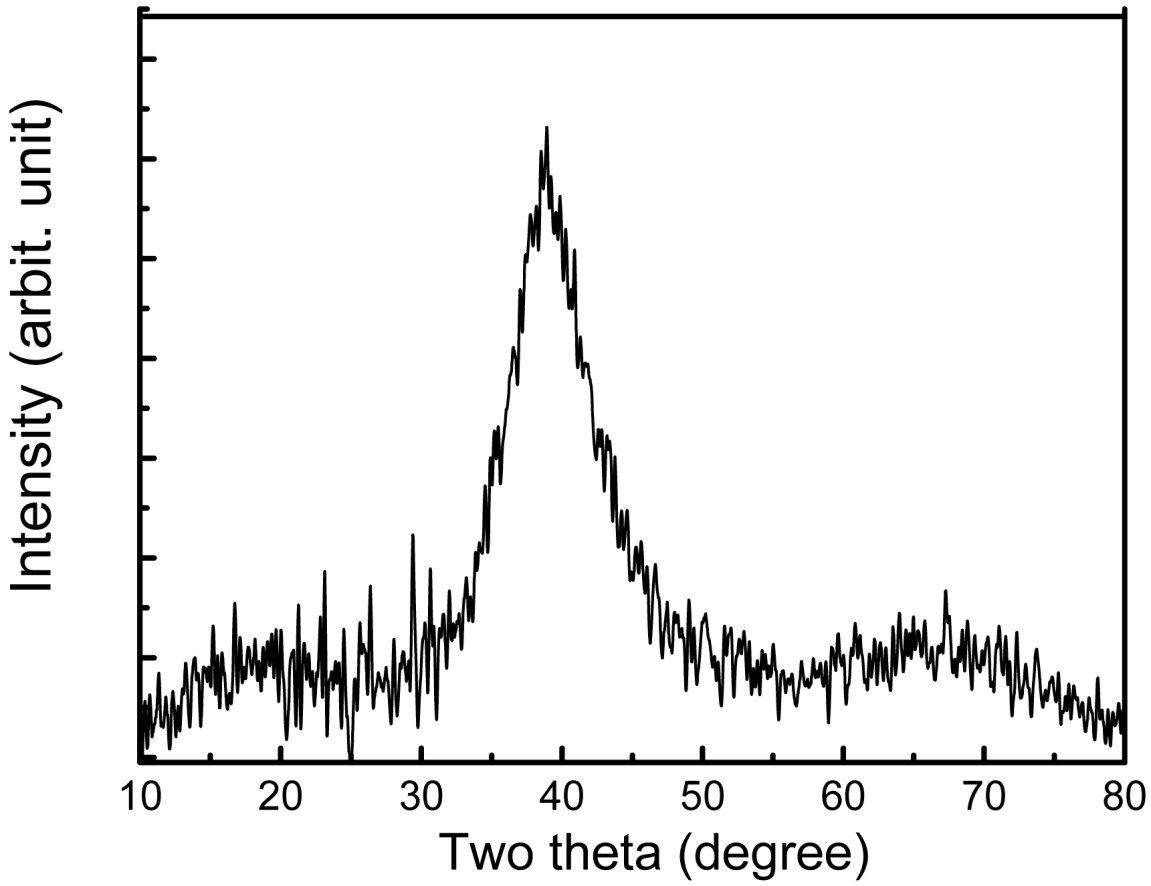

Fig. 46. XRD pattern of as-spun $Cu_{50}Zr_{45}Ti_5$ metallic glass.

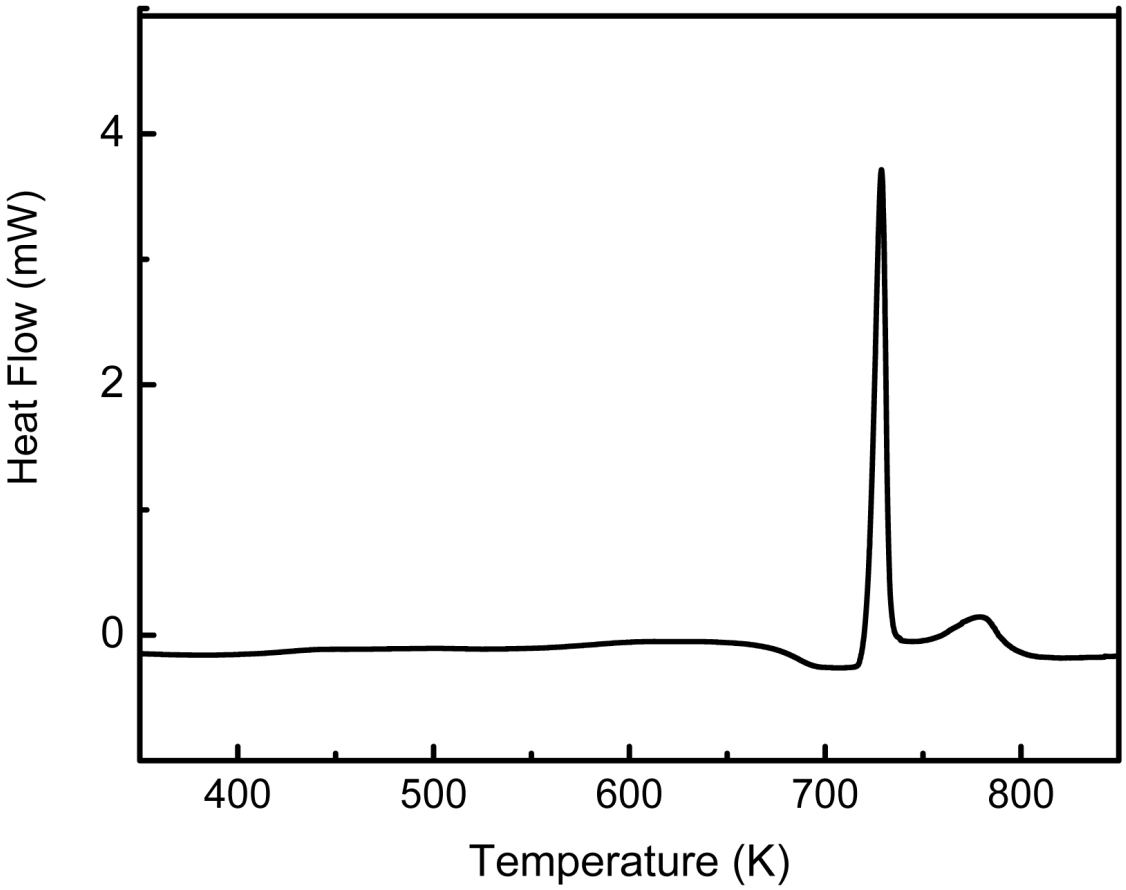

Fig. 47. DSC trace of as-spun $Cu_{50}Zr_{45}Ti_5$ metallic glass.

Fig. 48 shows the TEM micrograph of the sample prepared by electropolishing. No nanocrystals are observed. The inserted micrograph is the selected area diffraction (SAD) pattern for the corresponding TEM image. The micrograph pattern is maze-like and the SAD shows only halo rings. No white spots in the SAD corresponding to crystalline phases are presented. These observations, together with XRD and DSC, verify the glassy state of the as-spun sample. Note that the TEM specimen in Fig. 48 is prepared by using electropolishing, which eliminates the ion bombardment involved in ion milling.

Next, TEM results from specimens prepared by Ar ion milling at different energies are discussed. Fig. 49 shows TEM micrographs of $Cu_{50}Zr_{45}Ti_5$ glass prepared using 4 keV Ar ion milling without cooling. The bright-field image depicted in Fig. 49(a) and the dark-field image depicted in Fig. 49(b) show evidence of crystallization in the sample. Equiaxed grains and nanoparticles with an approximate diameter of 10 nm are observed. The SAD pattern inserted in Fig. 49(a) clearly shows sharp diffraction spots and discontinuous Debye rings. Lattice parameters extrapolated from inter-planar distances are compared with a powder diffraction file database [63]. The analysis suggests the formation of the $Cu_{10}Zr_7$ phase. Fig. 49(c) shows a high resolution TEM image of a selected area. Crystals with defects and small amorphous zones are observed.

Fig. 50 shows a HRTEM micrograph of the specimens prepared using 3 keV Ar ion milling without cooling. The SAD pattern inserted shows white diffraction dots and suggests partial crystallization. The HRTEM image shows nanocrystals dispersed in an amorphous matrix. Different from the case of 4 keV ion milling, the 3 keV ion milling leads to smaller crystals, typically less than 5 nm. Furthermore, HRTEM image reveals zones of dark contrast with an average size of less than 1 nm.

Fig. 51 shows a TEM micrograph from the sample prepared by 2 keV Ar ion

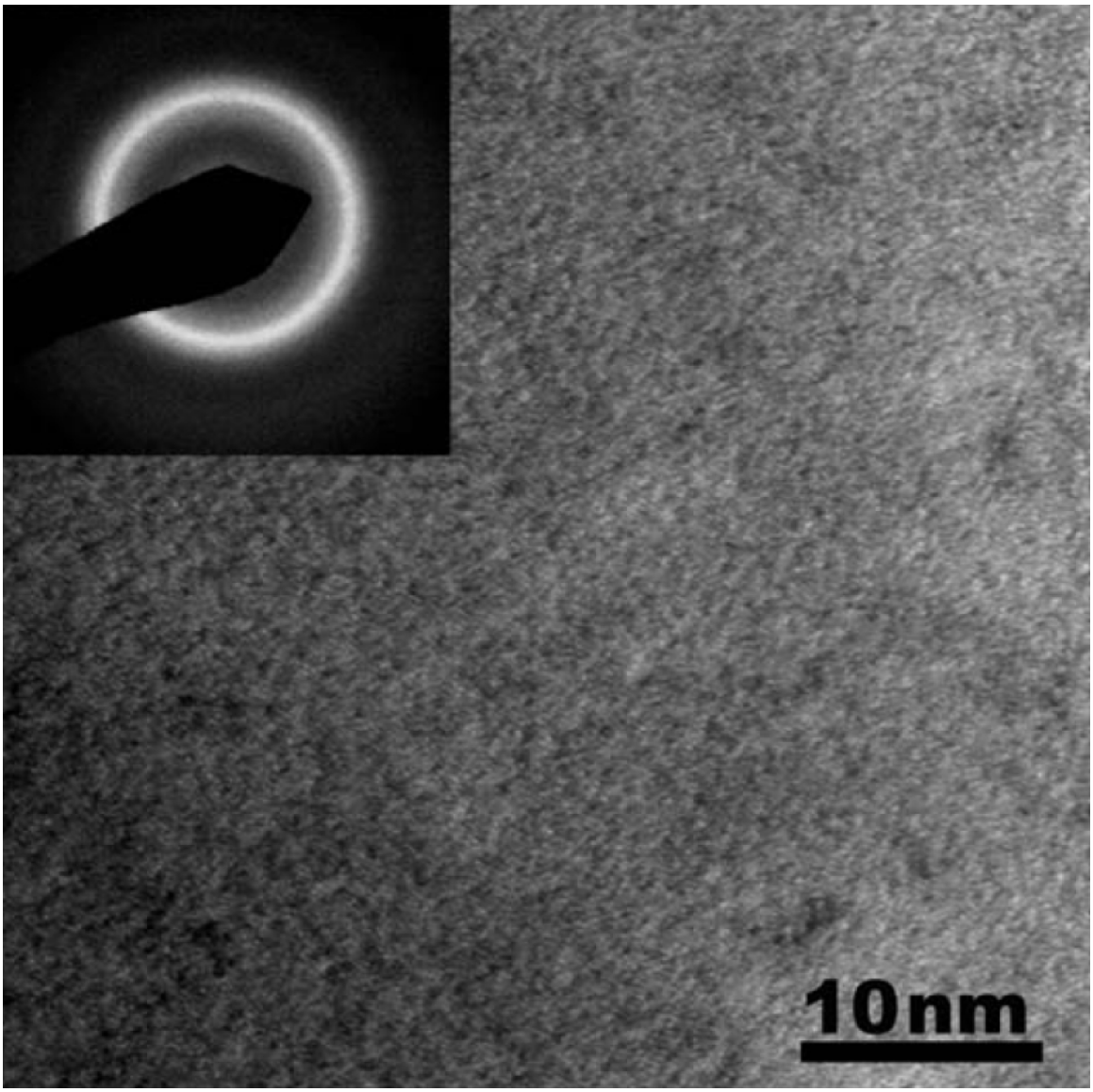

Fig. 48. Bright-field TEM of $Cu_{50}Zr_{45}Ti_5$ specimen prepared by electrochemical polishing and SAD inset.

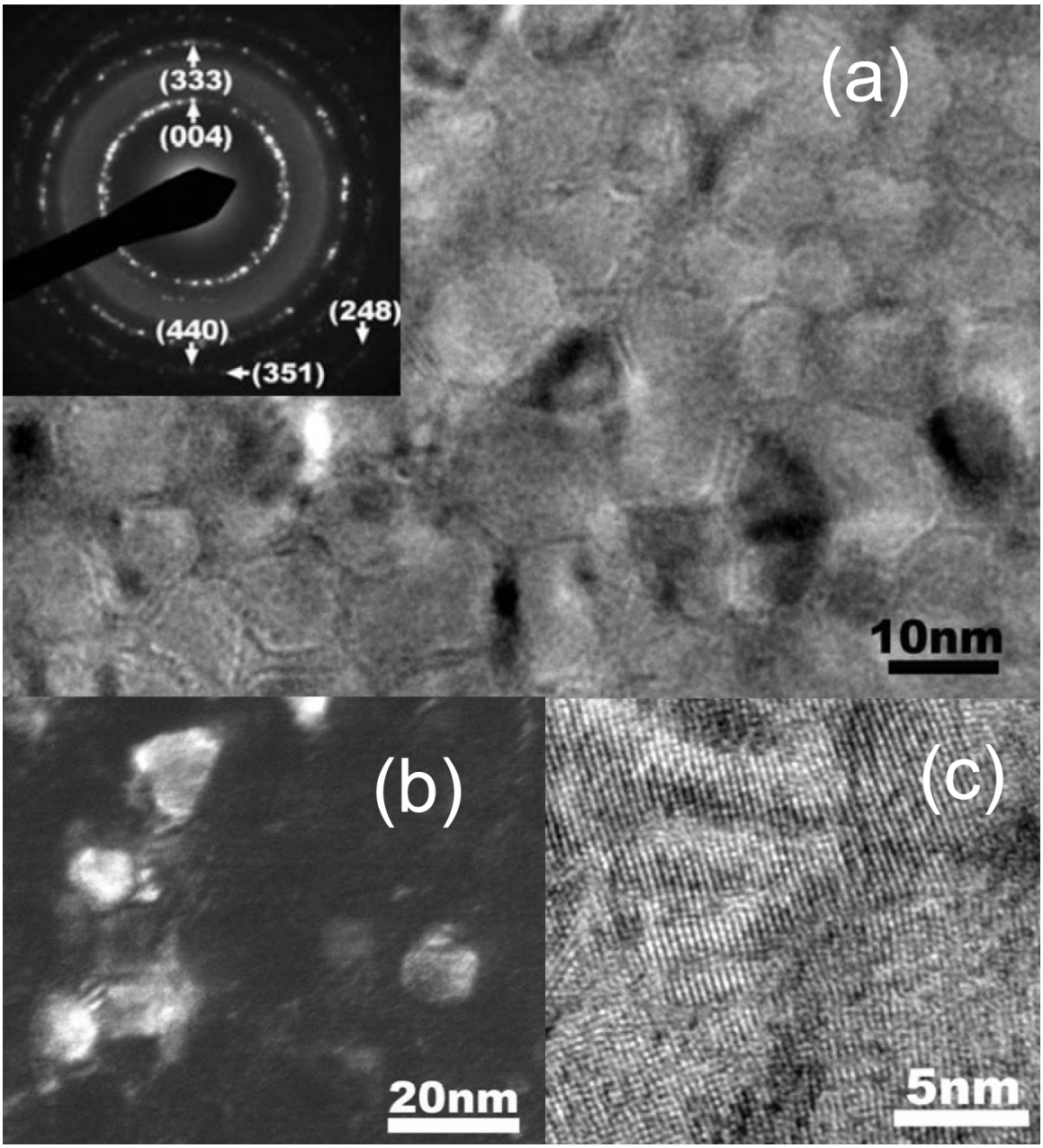

Fig. 49. (a) Bright-field TEM micrograph and SAD inset of $Cu_{50}Zr_{45}Ti_5$ glass specimen prepared using 4 keV Ar ion milling without cooling, (b) dark-field TEM micrograph, and (c) bright-field HRTEM micrograph of the same specimen.

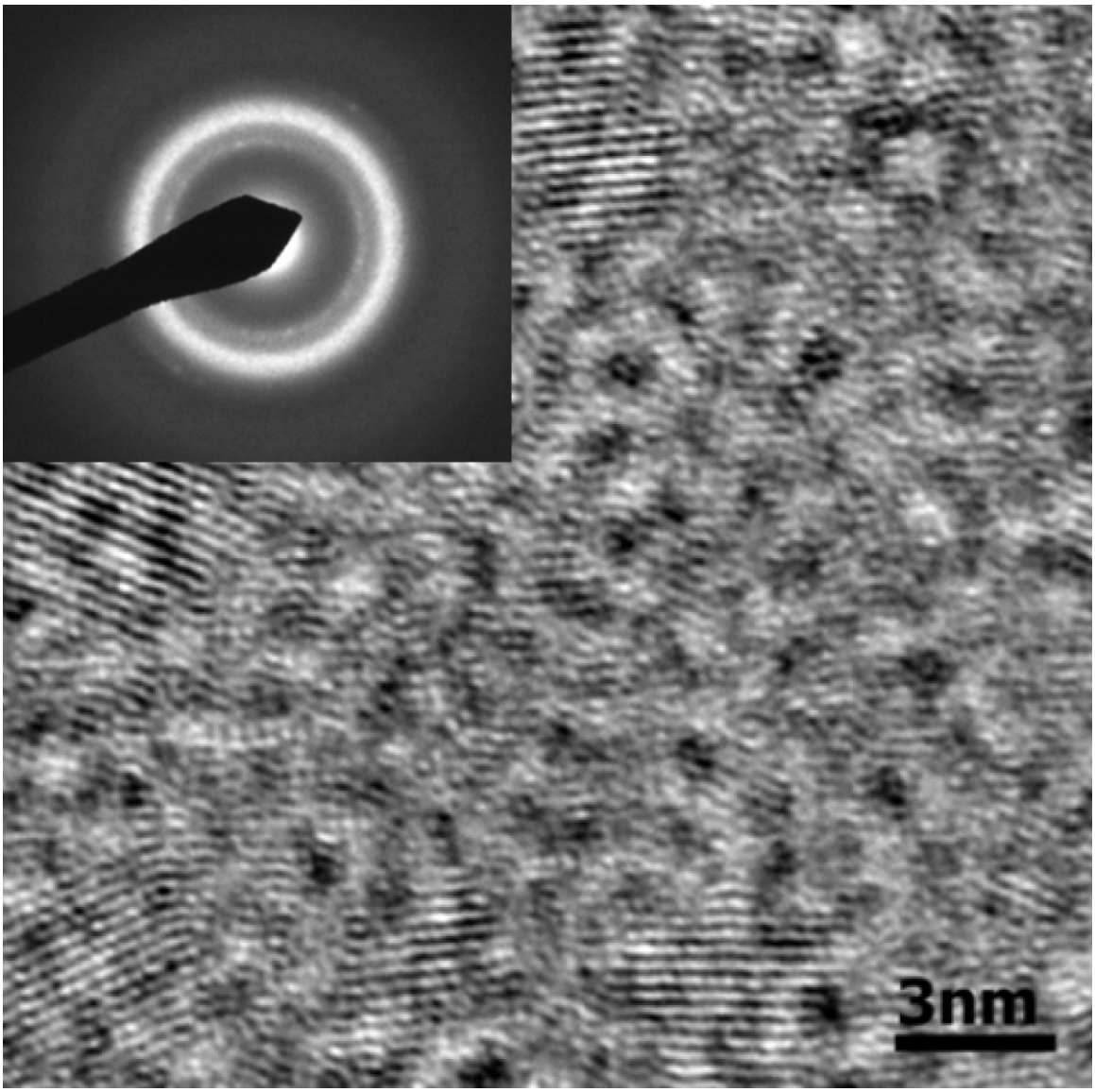

Fig. 50. Bright-field HRTEM micrograph of the specimen prepared using 3 keV Ar ion milling without cooling.

milling without cooling. SAD pattern does not show noticeable white spots. Both TEM and SAD do not suggest nanocrystal formation. Perhaps nanocrystals are too small to be detected. Furthermore, dark zones are found to form in the specimen, typically around 5 nm in size.

The dark contrast observed in both Figs. 50 and 51 could be caused either by inhomogeneous thinning or by composition contrast. To further clarify this, Energy-dispersive X-ray spectroscopy (EDX) is used to analyze the composition at different locations. EDX is not sensitive to specimen thickness. The X-ray intensity is primarily determined by atomic mass. Fig. 52 shows an EDX spectrum collected from the dark region of the sample shown in Fig. 51. Characteristic X-rays emitted from each element are identified. The mole fraction of each element is calculated by using the Cliff-Lorimer method based on the integration of X-ray line intensity of each element. The result shows that the dark region in Fig. 51 is $Cu_{10}Zr_7$ in composition, but not crystalline.

During ion milling, Ar ions were bombarded at a glancing angle of $\sim 5^{\circ}$. At an energy of 2-4 keV, the projected range of Ar ions in $Cu_{50}Zr_{45}Ti_5$ is less than 3 nm [49]. This limits the heavily damaged region to the very near surface region of the specimen. Surface ion bombardment can lead to composition fluctuation up to and beyond the depth of the bombarded region. Fluctuations can be a product of two simultaneous mechanisms. The first mechanism is enhanced atomic migration due to beam heating. Temperature of the specimens can not be measured in the present study, but reports in literature suggest that specimens under similar ion milling conditions (Ar ion milling at energy of 2-4 keV without cooling) can be heated up to 200 $^{\circ}$C [83]. Although this temperature is much lower than the glass transition temperature, previous studies have shown that composition fluctuations can occur upon low-temperature annealing [84]. The second mechanism is enhanced atomic migration as a result of ballistic

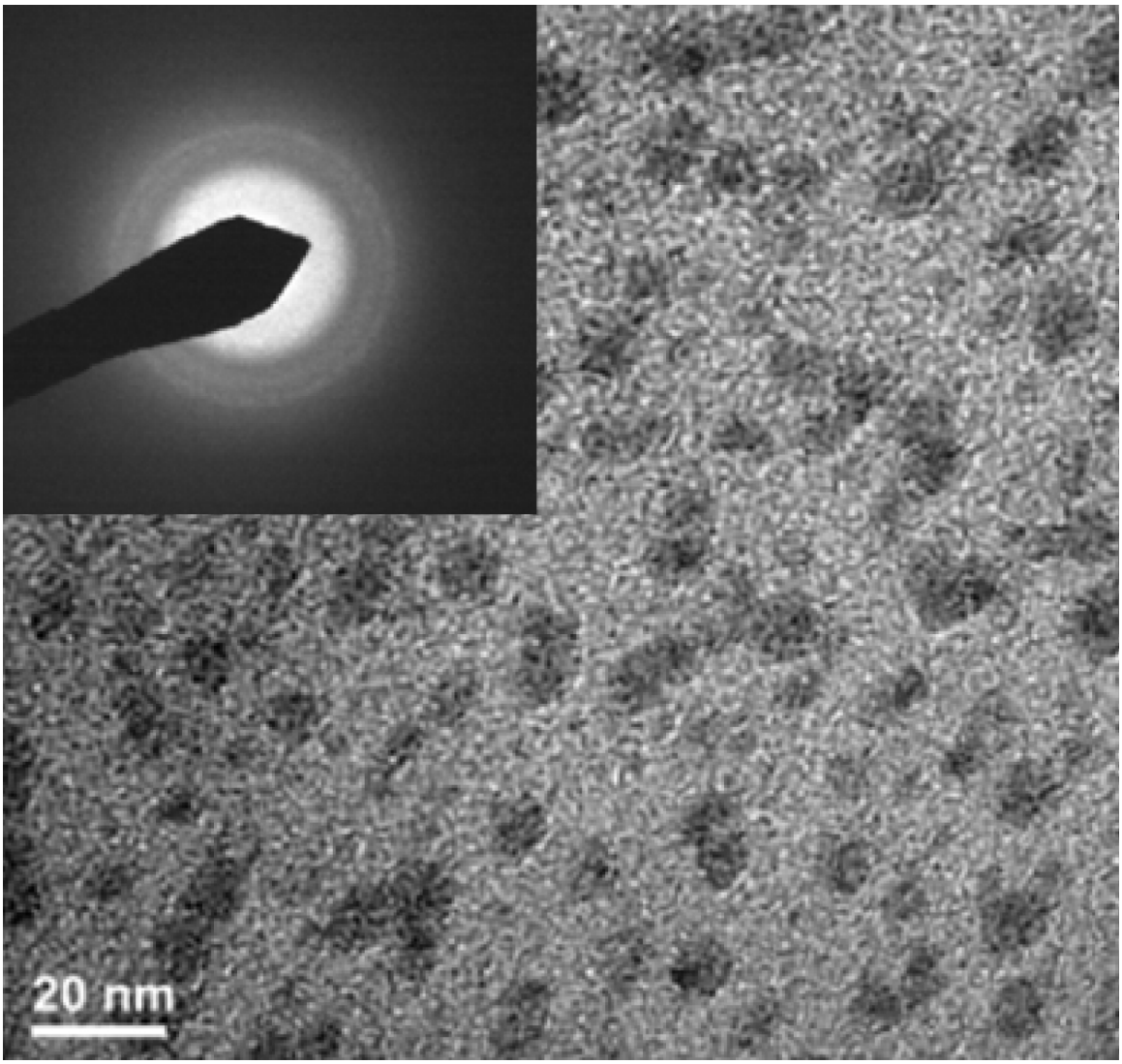

Fig. 51. Bright-field TEM micrograph of the specimen prepared using 2 keV Ar ion milling without cooling.

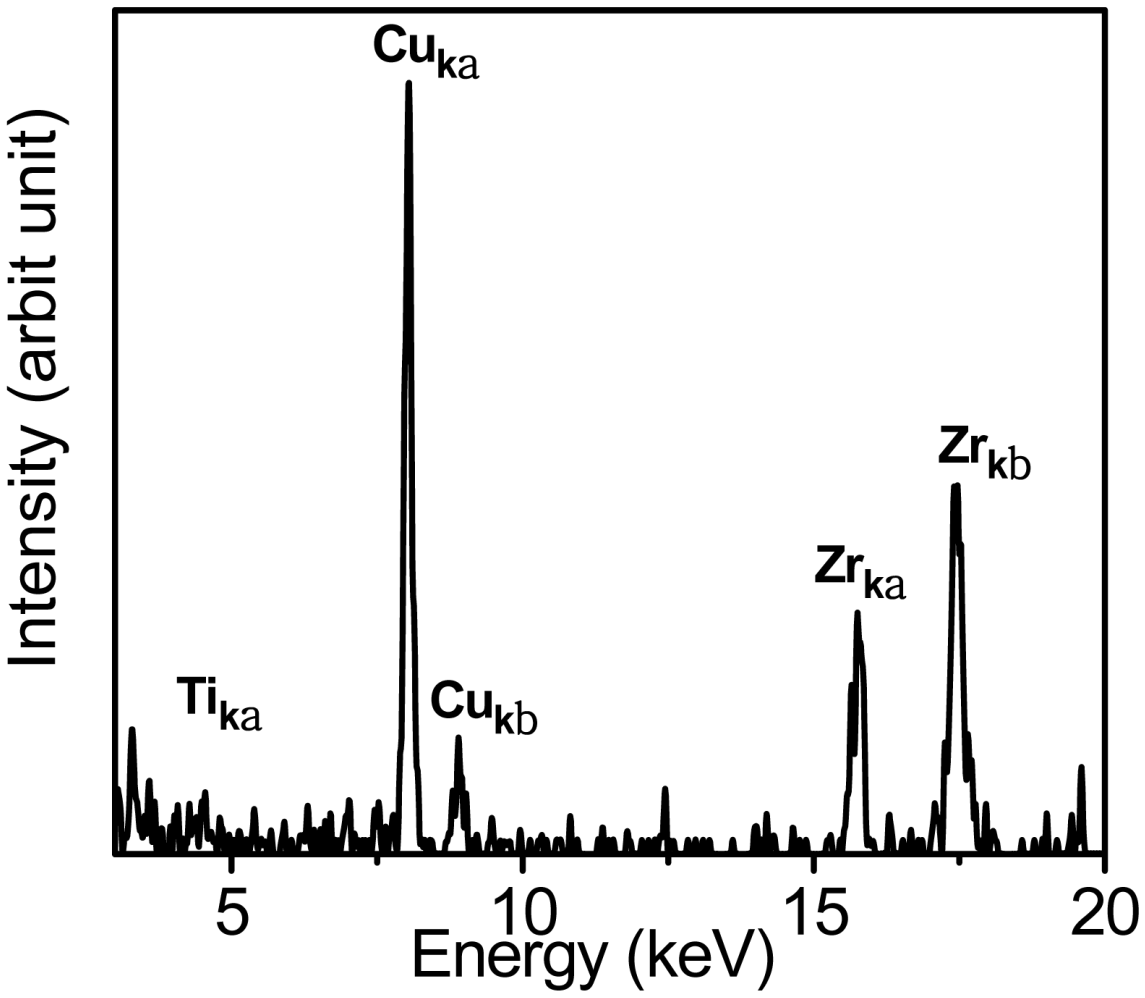

Fig. 52. EDX spectrum of dark region shown in Fig. 51.

collisions and energy dissipation of collision cascades.

Two important observations in the present study are the formation of the $Cu_{10}Zr_7$ phase without appreciable crystallization from low energy ion milling (as shown in Fig. 51) and the formation of nanocrystals in the $Cu_{10}Zr_7$ phase from high energy ion milling (as shown in Fig. 49(a)). The formation of the same phase suggests that chemical decomposition might be a necessary intermediate stage for crystallization. Before crystallization, a decompositional state might form to lower the system's Gibbs free energy, followed by the nucleation of the phase. Furthermore, formation of a crystalline phase suggests that the phase is more thermodynamically stable than the glassy state. The same phase has been observed after isothermal annealing of the same metallic glass [33].

To further shed light onto the crystallization mechanism, we have exposed the specimen (from 2 keV Ar ion milling without cooling) to the TEM analyzing beam for an extended period of time to induce crystallization (estimated ion fluence is larger than 1×10^{27} electrons/m^2). Under high fluence electron irradiation, darker spots appeared as seen in the bright-field TEM micrograph in Fig. 53. Fig. 54 shows the corresponding dark-field TEM image of the same sample. The white spots in dark-field image suggest the spots are nanocrystals. Under electron irradiation, a few nanocrystals form in the bright regions, but a majority of the nanocrystals form in the dark region. This suggests the bright region is relatively stable against crystallization.

Reducing Ar ion energy will reduce the energy deposited on the specimen. This will reduce the specimen temperature and consequently, composition fluctuation and crystallization. Unfortunately, due to space charge effects, it is difficult to further lower Ar ion energy while maintaining reasonable ion fluxes. If beam heating plays an important role, a cold milling will alleviate the issues. Fig. 55 shows the TEM micrograph obtained with 2 keV Ar ion milling plus liquid nitrogen cooling. The

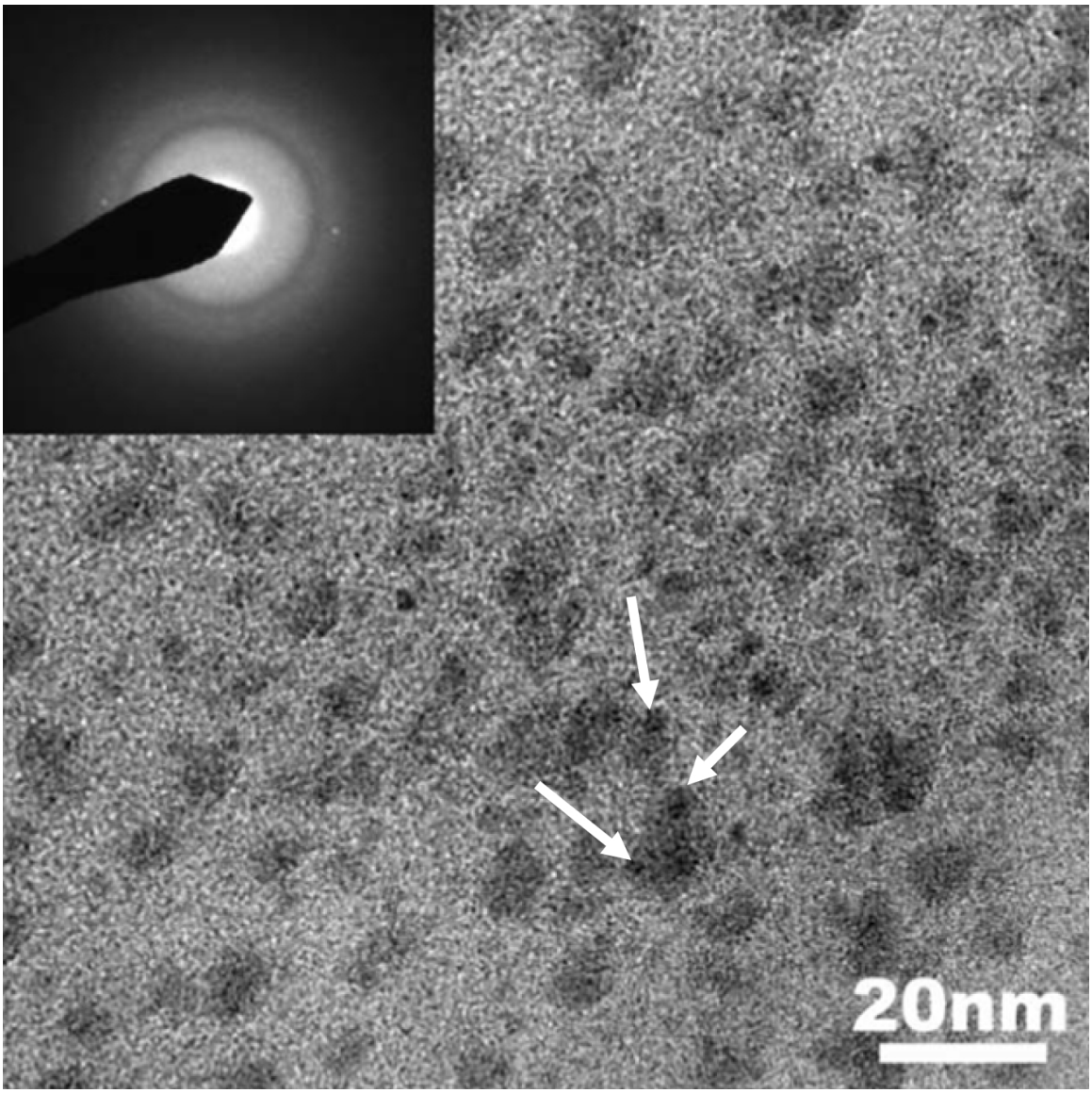

Fig. 53. Bright-field TEM micrograph of the specimen shown in Fig. 51 after exposure to high fluence electron beam. Arrows in the figure indicate nanocrystals.

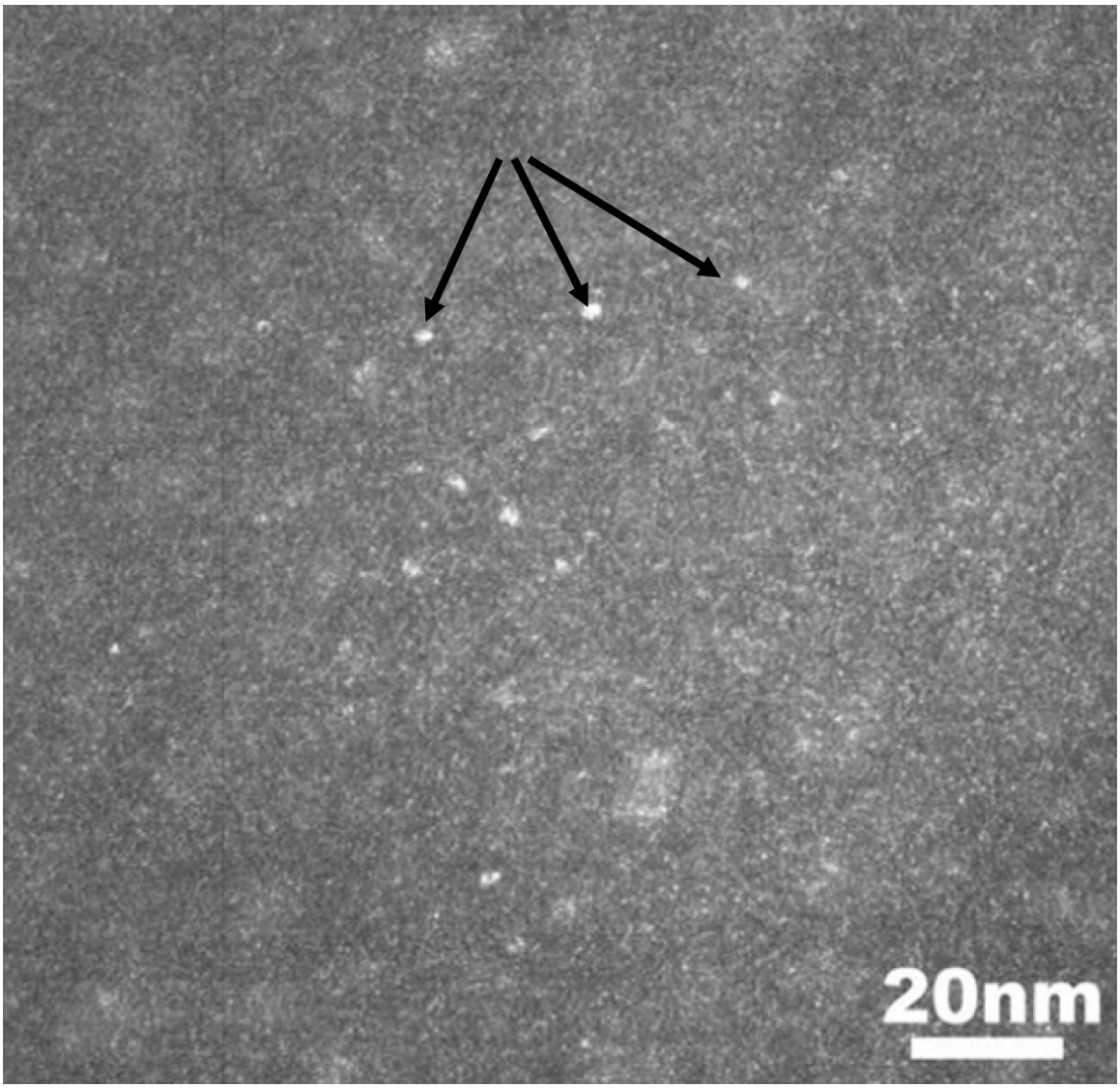

Fig. 54. Dark-field TEM micrograph of the specimen shown in Fig. 51 after exposure to high fluence electron beam. Arrows in the figure indicate nanocrystals.

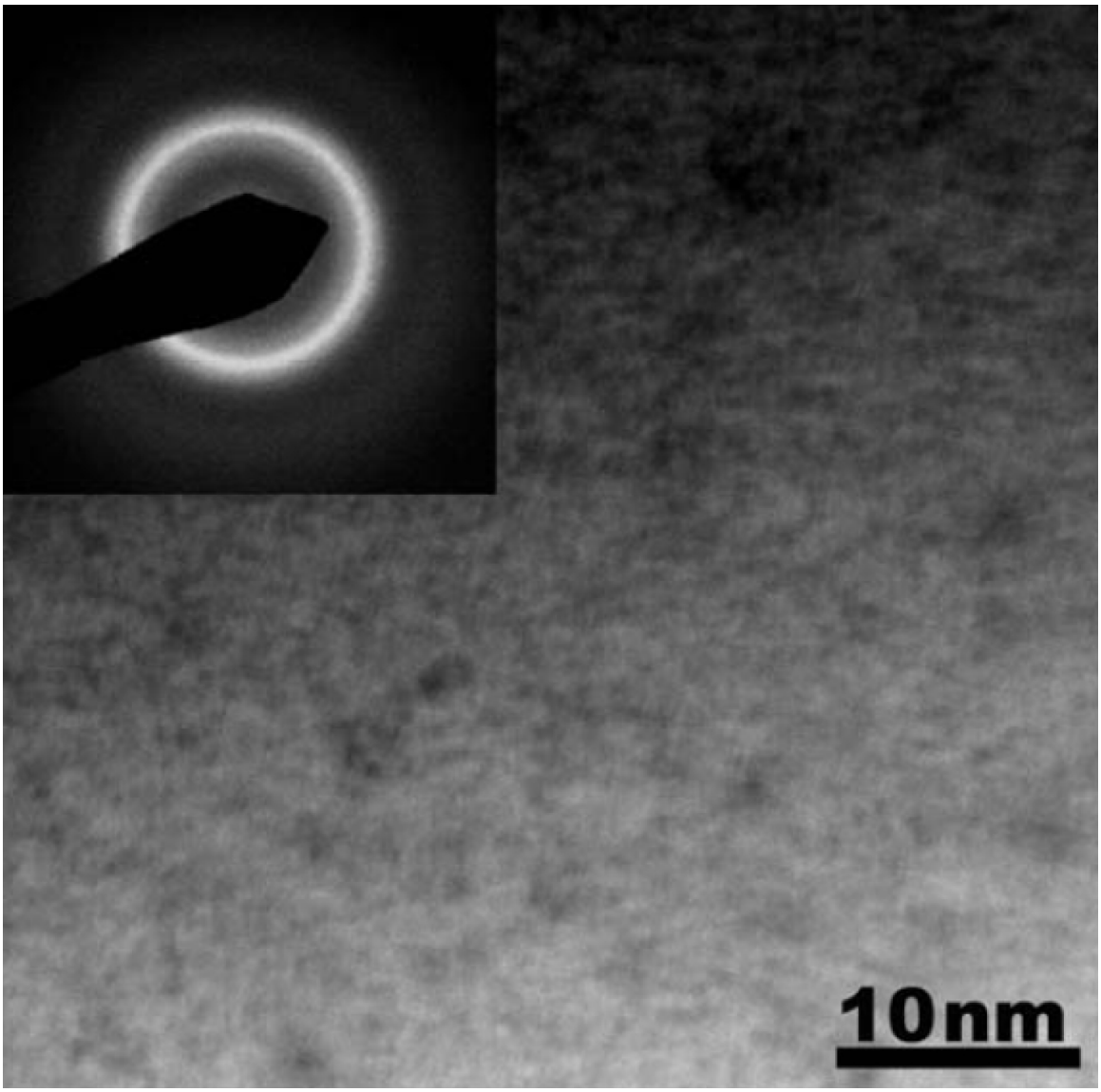

Fig. 55. Bright-field TEM micrograph of the specimen prepared using 2 keV Ar ion milling with liquid nitrogen cooling.

cooling reduced the specimen temperature to around −100°C. Both the TEM image and the inserted SAD pattern did not reveal nanocrystal formation. This proves that the conditions for ion milling must be carefully selected to ensure proper specimen preparation. The microstructure must remain undisturbed through the preparation process for proper sample characterization.

In summary, We have studied the Ar-ion-milling induced microstructural changes in $Cu_{50}Zr_{45}Ti_5$ metallic glass during TEM specimen preparation. High energy ion milling (3 and 4 keV Ar) without cooling can induce specimen crystallization. With lower energy ion milling (2 keV Ar) without cooling, there is no noticeable crystallization, but a nanoscale inhomogeneous decomposition with $Cu_{10}Zr_7$ phase formation is observed and nucleation can be brought about through further irradiation. There are no observable structural changes from specimen preparation using low energy cold milling (2 keV Ar) using liquid nitrogen cooling. Furthermore, upon high fluence electron irradiation in situ by TEM, a Cu-rich $Cu_{10}Zr_7$ phase is formed.

CHAPTER X

DISCUSSION

It has been shown quite clearly that it is possible to initiate crystallization of metallic glass through the use of ion irradiation. This chapter will discuss the overall mechanism for nanocrystal formation in metallic glasses based on the evidence of ion irradiation experiments from previous chapters. Such experiments using different particle irradiation techniques give light to the amorphous-to-crystalline transition as a function of many parameters, such as projectile mass, projectile energy, and glass composition, to name a few. Further discussion of crystallization kinetics will be made using phase diagrams to help explain the phases formed upon irradiation.

In previous chapters, we discussed the driving force for crystallization in metallic glasses, i.e., metallic alloys prefer to be crystalline, but through proper selection of components, the driving force is not enough for long-range ordering. If crystallization is to occur, atoms need to segregate to form a nucleation site and subsequent growth must be aided by decreased viscosity in the system to allow diffusion. An important thing to establish is the physical mechanism allowing for crystallization in a metallic glass under irradiation that differs from other mechanisms, such as annealing [85] or controlled cooling [26].

Since crystallization of metallic glasses can occur under high temperatures, care needs to be taken to not allow the specimen temperature to reach temperatures that invoke crystallization. Under most cases, this is simple - the sample temperature can be monitored my means of a thermocouple attached to the sample stage. This is what has been done during the experiments discussed in this paper with exception of the electron microscope study. For medium and heavy ion irradiation, increase in sample temperature during irradiation was kept below 50 °C. The temperature in the

electron irradiation case was not measured but can be calculated using the energy deposited in the specimen as discussed in a previous chapter. The temperature rise in a sample due to beam heating was determined by Jencic et al. [55] as shown in Eqn. 4.3. The stopping power of an electron was estimated with Eqns. 4.4 and 4.5. The average temperature rise was calculated to be 3.2 K in $Cu_{50}Zr_{45}Ti_5$ (MG1) and 5.5 K in $Zr_{55}Cu_{30}Al_{10}Ni_5$ (MG2), which are almost negligible considering the crystallization temperatures in these metallic glasses are above 700 K. It is clear that beam heating is not the reason for crystallization in these experiments.

Another possible reason for crystallization is through direct nucleation from damage cascades. Pockets of heavily displaced atoms are created by energetic particle irradiation, more so by heavy ions but the effect is still present in light particle irradiation. In a damage cascade, lattice vibration energy near the collision site can be on the order of several thousand degrees and local energy deposition can be many times greater than that needed to melt the material. Atoms in a damage cascade can easily receive more than 1 eV/atom. If the atomic motion is regarded as thermal energy by k_BT, where k_B is Boltzman's constant and T is the temperature, mean temperatures in a displacement cascade can exceed thousands of degrees [48]. For this reason, a large damage cascade is referred to as a "thermal spike".

In a thermal spike, many atoms in a displacement cascade have high energy and become mobile, as if in a liquid [51]. If the thermal spike phenomena directly lead to crystallization, then the mobile atoms in the "melting-zone" would rearrange themselves into the preferred ordered structure as the energy of the system is dissipated or "quenched" back to room temperature. This process is similar to the original quenching of the atoms when the original metallic glass was formed. If the cooling rate is slow enough, ordered structures will form as the temperature drops below the melting temperature. The thermal spike cannot be the direct crystallization event

because the time scale of such an event is too small. The cascade duration is about 10^{-13} seconds and the quench rate of a thermal spike is on the order of 10^{-12} seconds [48]. An approximation of the quench time in a thermal spike is given by

$$t_q \approx \frac{r^2}{4D_T} \tag{10.1}$$

where r is the radius of the thermal spike and D_T is the thermal diffusivity of the material [86]. The thermal diffusivity in MG2 for instance, is about 2×10^{-6} m^2 – s. If the displacement cascade is 10 nanometers in diameter, then the quench time is about 3 picoseconds. If the cascade diameter is increased to 100 nanometers, a rather large cascade, the quench time is still less than a nanosecond. Metallic glass will be very difficult to crystallize from thermal spiking because it was built to withstand crystallization.

If crystallization is to occur by this direct method, then atomic segregation must occur during the very short cascade duration time and crystallization must happen in the short quenching period. This is much faster than the estimated critical cooling rate for Cu-Zr and Cu-Zr-Ti metallic glasses of $10^2 - 10^4$ K/s [76]. Other metallic glasses need similar cooling rates [1]. For crystallization to occur the quench rate must be slower than the critical cooling rate. That is, due to the high viscosity of the glass, which was desired during fabrication, the atoms need a finite and lengthy amount of time to reorganize themselves into a structure. The melting temperature of MG2 is about 1100 K. Using the above quenching rates, a 0.1 - 10 second quench is needed to form a glass, but the thermal spike quench time calculated above is much faster than this. Cooling rates in the damage cascade region would need to be lower than the critical cooling rate to begin an amorphous-to-crystalline transition, so the thermal spike phenomena is not enough to explain crystal formation in metallic glass.

Analysis of experimental data along with investigation of interaction physics

shows that the thermal spike phenomena discussed in a previous chapter is insufficient for direct crystallization. Instead, it is a combination of several displacement cascades combined with enhanced diffusion, as described by the excess free volume model, that is necessary for crystallization.

In a previous chapter, the free volume dependence on diffusivity was discussed. The diffusion coefficient is dependent on the average free volume. Also, it was mentioned that the driving force to crystallize is already built in to the glass, only the diffusivity must be enhanced to begin crystallization. Localized increases in free volume come about through displacing atoms from their sites by particle irradiation. Energetic particles or knock-on atoms can collide with glass atoms and push them to a new location, leaving free space in its place - basically a hole, described earlier as excess free volume. In a damage cascade, large numbers of atoms are displaced from their sites. With large enough holes, the atoms become highly mobile and can begin to rearrange themselves. That physical phenomenon is usually measured as an increase in diffusivity.

The question arises of the quantity of crystallization that is expected during irradiation of metallic glass. It comes down to the damage tomography of an energetic ion. For the same amount of damage, usually measured in displacements per atom (dpa), a heavy ion can create large pockets of displaced atoms which can lead to large diffusivity enhancements at the heart of a damage cascade, as opposed to a light ion which creates a few displacements along its trajectory. This is the reasoning for the mass-dependent study on irradiation of metallic glasses.

If displacements are to be created in order to invoke a diffusivity enhancement, the particle mass and energy must be chosen such that the energy imparted to target atoms is enough to overcome the energy barrier for displacement. The amount of energy a knock-on atom receives is governed by conservation of mass and momentum,

Table IV. Maximum energy transfered to target of elements in metallic glass samples $Cu_{50}Zr_{45}Ti_5$ and $Zr_{55}Cu_{30}Al_{10}Ni_5$ listed with displacement energies for atomic Al, Ti, Ni, Cu, and Zr.

Target	Electron E_{max} (eV)	140 keV He E_{max} (eV)	1 MeV Cu E_{max} (eV)	E_d (eV)
Al	16.3	63×10^3	836×10^3	16
Ti	9.15	40×10^3	980×10^3	19
Ni	7.47	33×10^3	998×10^3	23
Cu	6.9	31×10^3	1000×10^3	19
Zr	4.8	23×10^3	968×10^3	21

but the maximum energy received is calculated using Eqn. 3.2 repeated here:

$$E_{max} = \frac{4m_1m_2}{(m_1^2 + m_2^2)}E,$$

If the minimum displacement energy of a material is E_d, then the condition $E_{max} > E_d$ must be met if displacements are to occur. The quantity E_{max} is simple to compute for a given projectile and target ion, but E_d is more complicated. Usually E_d is computed or experimentally determined for a single element. The displacement energy would be a function of PKA displacement angle due to lattice effects, but a minimum and average value can be extracted. The E_d values of several elemental materials [48, 87] are shown with E_{max} calculated for three different experiments presented in this paper. The calculations are shown in Table IV. The displacement energy for the metallic glasses in these experiments will be slightly different since the glass is a mixture of the elements, but a similar value is expected.

It is clear from the table that the He and Cu ion irradiation experiments in this dissertation are capable of producing displacements in the metallic glasses in ques-

tion. It is not clear, however, for the electron irradiated case since the displacement energy is greater than the maximum energy imparted to target atoms. However, we do show evidence of electron-irradiation-induced crystallization in MG1, and we have shown that beam heating and thermal spiking is not the cause for crystallization, so displacement-induced diffusivity enhancement must be the reason for crystallization. There are, however, several reasons that many displacements can be created in through electron irradiation. It has been proposed that the displacement energy in glasses is less than their crystalline counterparts [53]. This could be a product of density fluctuations in the glass since its packing is random, leading to lessened bonding of atoms in their sites. It has been suggested also [55] that crystallization by subthreshold electrons can be induced by exciting the electrons of the glass leading to lessened bonding to neighbors and decreased displacement energy. Finally, in early radiation experiments by Kinchin and Pease [51], electrons were treated as relativistic. We know from relativistic physics that the expression involving the kinetic energy, E, of a particle is $E + m_0c^2 = \gamma m_o c^2$. In the TEM experiments, electrons were accelerated to 200 keV and the rest mass of an electron is 511 keV, so we can treat the electron as having $\gamma \approx 1.4$ times the mass, which will increase the maximum energy transferred by as much as 40% for heavy elements.

Though there are many reasons that electrons can induce crystallization in MG1, it is apparent that MG2 is more stable under electron irradiation. The lightest atom, Al, which has the highest E_{max}, is not present in MG1, but is present in MG2. Nevertheless, we have shown MG2 did not crystallize under electron irradiation. A possible reason for this is intrinsic stability of MG2 over MG1 shown in the larger subcooled liquid region in MG2. The thermal stability of metallic glass is gauged by the width of the subcooled liquid region, ΔT_x, the temperature difference between the glass transition and crystallization temperatures. MG2 shows a ΔT_x almost twice as

large as MG1, indicating a much greater stability against crystallization than MG1. It is unclear if the resistance to electron irradiation is due to an increased minimum displacement energy or increased viscosity. It is possible that the electron beam is creating displacements, but the resulting diffusivity increase is not enough to crystallize the glass which has shown superior resistance to crystallization. In other experiments with $Zr_{55}Cu_{30}Al_{10}Ni_5$, complicated phases such as $Cu_{10}Zr_7$, $CuZr_2$, and $NiZr_2$ were found in XRD measurements after annealing [88]. These phases were found in heavy ion irradiation. If these complex structures are simultaneously trying to nucleate, a high level of mobility is needed in the glass, but the electron irradiation cannot provide enough energy to do so. Even if the exact reason for radiation tolerance is not known, the electron irradiation study results in an interesting finding regarding the radiation resistance of metallic glasses. Next we will examine the radiation response of metallic glasses to heavier ions.

Using software that can simulate the interactions of ions with matter, such as SRIM (The Stopping and Range of Ions in Matter) [49], the damage, or the displacement density, can be estimated. SRIM uses the Monte Carlo method to simulate ion stopping by using tabulated stopping powers using the ZBL potential (an acronym based on the first letters of its authors, Ziegler, Biersack, and Littmark). It is instructive to see the physical size of damage cascades in both light and heavy ion irradiation. SRIM simulations of several light and heavy ion tracks are shown in Fig. 56. The simulations in Fig. 56(a) represents 140 keV He in MG2, and Fig. 56(b) represents 1 MeV Cu in MG2. The simulations in Fig. 56 illustrate many things. The ranges of 140 keV He and 1 MeV Cu in MG2 are similar, but the Cu ion creates many more displacements per ion track. SRIM estimates that nearly 10 times as many displacements are caused per ion track by Cu than by He. Not only that, but the sizes of displacement cascades are very different. The He ion creates many small

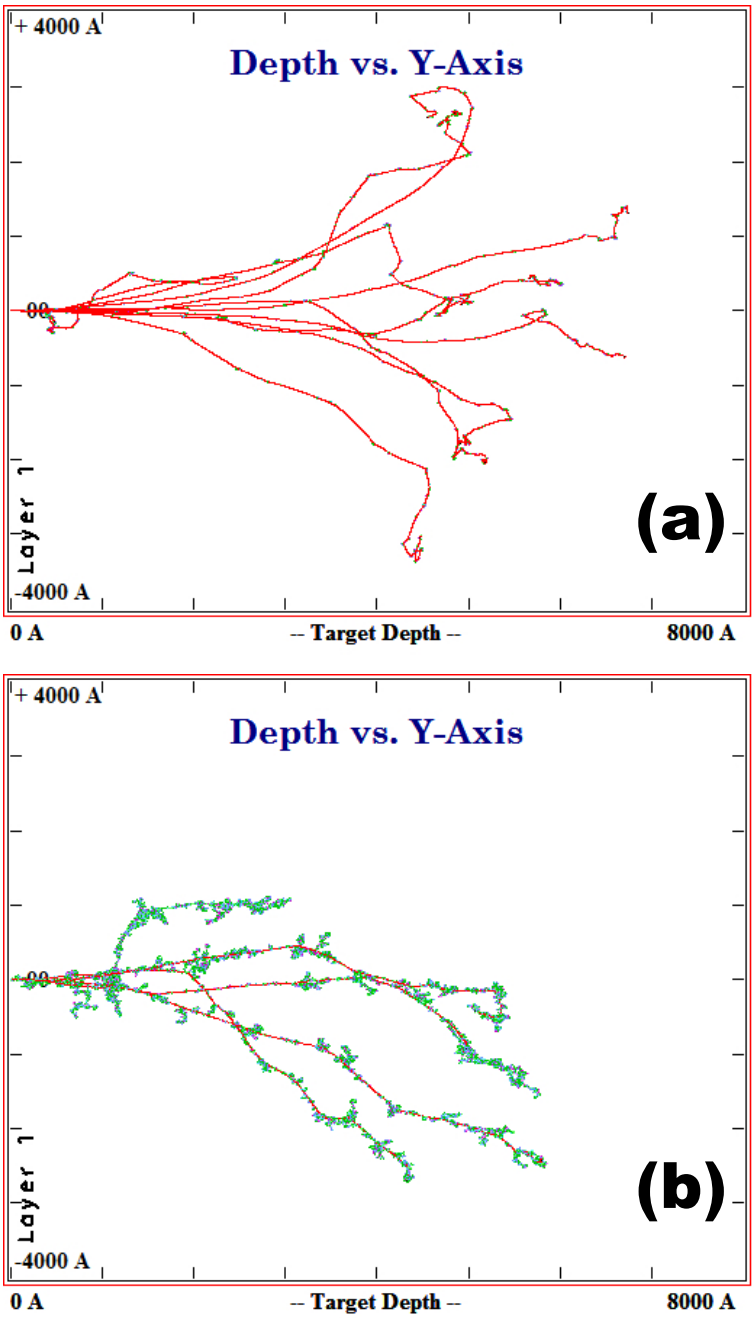

Fig. 56. Simulations from SRIM depicting several ion tracks (red) and subsequent damage cascades (green) in $Zr_{55}Cu_{30}Al_{10}Ni_5$ by (a) 140 keV He and (b) 1 MeV Cu ion irradiation.

cascades along its path with large distance in between. The Cu ion creates few but very dense cascades along its path. In the center of such a dense cascade, many ions are estimated to be displaced, causing an increase in the localized free volume and increased atomic diffusivity. With fewer atoms displaced in a small cascade from a light ion, the free volume increase will be less and the diffusivity enhancement will be less. Therefore, larger crystals are expected in heavy ion irradiation since the local diffusivity enhancement is potentially greater.

Another aspect of ion irradiation is the preferred displacements of elements. The ions slow down when penetrating through matter by collisions with target atoms, but some target atoms present a greater probability of collision than others. This concept is known as cross-section. Therefore the stopping power of ions is a function of both cross section and the amount of energy that can be transferred in collisions. Since metallic glass consists of many elements, the ion may impart more energy to some atoms than others, resulting in irradiation induced segregation of elements in the glass. The stopping powers of Cu in elements found in metallic glass are shown in Fig. 57 using stopping power data from [49]. A Cu ion appears to be able to transfer more energy to Zr than Cu, though conservation of mass and momentum dictates that the PKA energy is maximized in Cu because $m_1 = m_2$. However, this effect is present throughout the sample so the overall effect is less important than the effect of irradiation enhanced diffusivity.

There is much to be learned from the dark-field (DF) micrographs of ion irradiated metallic glass. DF images are a part of the diffracted electron beam in an electron microscope. Therefore the bright spots that show up are exposure due to diffracted electrons. The electrons are diffracted by the planes in the crystal structures of the specimen, nanocrystals in our case. The opposite is true so diffracted ions appear as dark contrasts in bright-field TEM. Many electron micrographs are shown

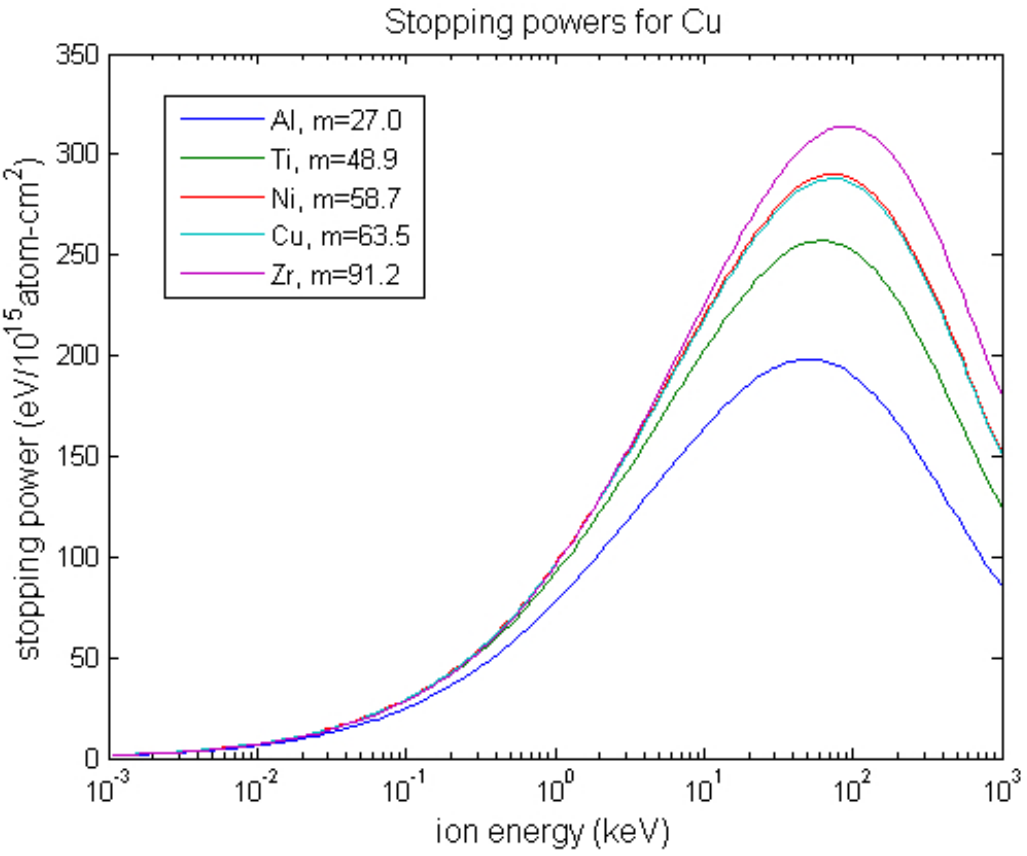

Fig. 57. Stopping power of Cu in metallic glass elements. The normalized (density independent) stopping powers are plotted against Cu ion energy. The five elements are shown with their masses in amu.

in Fig. 58. From Figs. 58(a) and 58(b), the electron in MG1 and He irradiated MG2 cases, Figs. 58(a) and 58(c), respectively, the nanocrystal sizes range from about 1 nm and reach a maximum at about 10 nm. The Cu ion irradiated specimens are shown in Figs. 58(b) (MG1) and 58(d) (MG2). The range of nanocrystal sizes in those cases is much greater, with some nanocrystals exceeding 100 nm in diameter. The total number of atoms involved in a crystal is proportional to d^3, where d is the diameter of the crystal. Hence the number of atoms involved in a crystal of 100 nm diameter is three orders of magnitude higher than in a 10 nm crystal. While the fluences and dpa are not equal in the He and Cu experiments (He irradiation resulted in about 15 dpa while Cu irradiation about 30 dpa), they are far less than 3 orders of magnitude different. This is another indication that heavy ions are able to create larger nanocrystals in metallic glass since the damage cascades are larger.

Both irradiated MG2 specimens show a bimodal nanocrystal size distribution. That is, there exists many nanocrystals that are around 100 nm in size, but also a large population of nanocrystals that are a few nanometers in size. This shows up in both irradiated MG2 specimens but neither irradiated MG1 specimen. TEM diffraction pattern (DP) analysis shows lattice spacings indicative of $Cu_{10}Zr_7$ and $CuZr_2$ phases in both MG1 and MG2, but additionally in MG2 there appears to exist a $NiZr_2$ phase. The $NiZr_2$ phase obviously does not show up in the irradiated MG1 case because no Ni is present in MG1. The small nanocrystals in the irradiated MG2 specimens are likely to be the $NiZr_2$ phase because of the small concentration of Ni (5%) in MG2 ($Zr_{55}Cu_{30}Al_{10}Ni_5$).

Also, the issue of nanocrystal composition in metallic glasses must be discussed. The data shows that, in almost every case, a Cu_xZr_y phase nucleates after irradiation. Primarily, $Cu_{10}Zr_7$ phase was found in electron irradiated, He irradiated, Ar irradiated, and Cu irradiated metallic glass. This makes sense since both metallic glasses

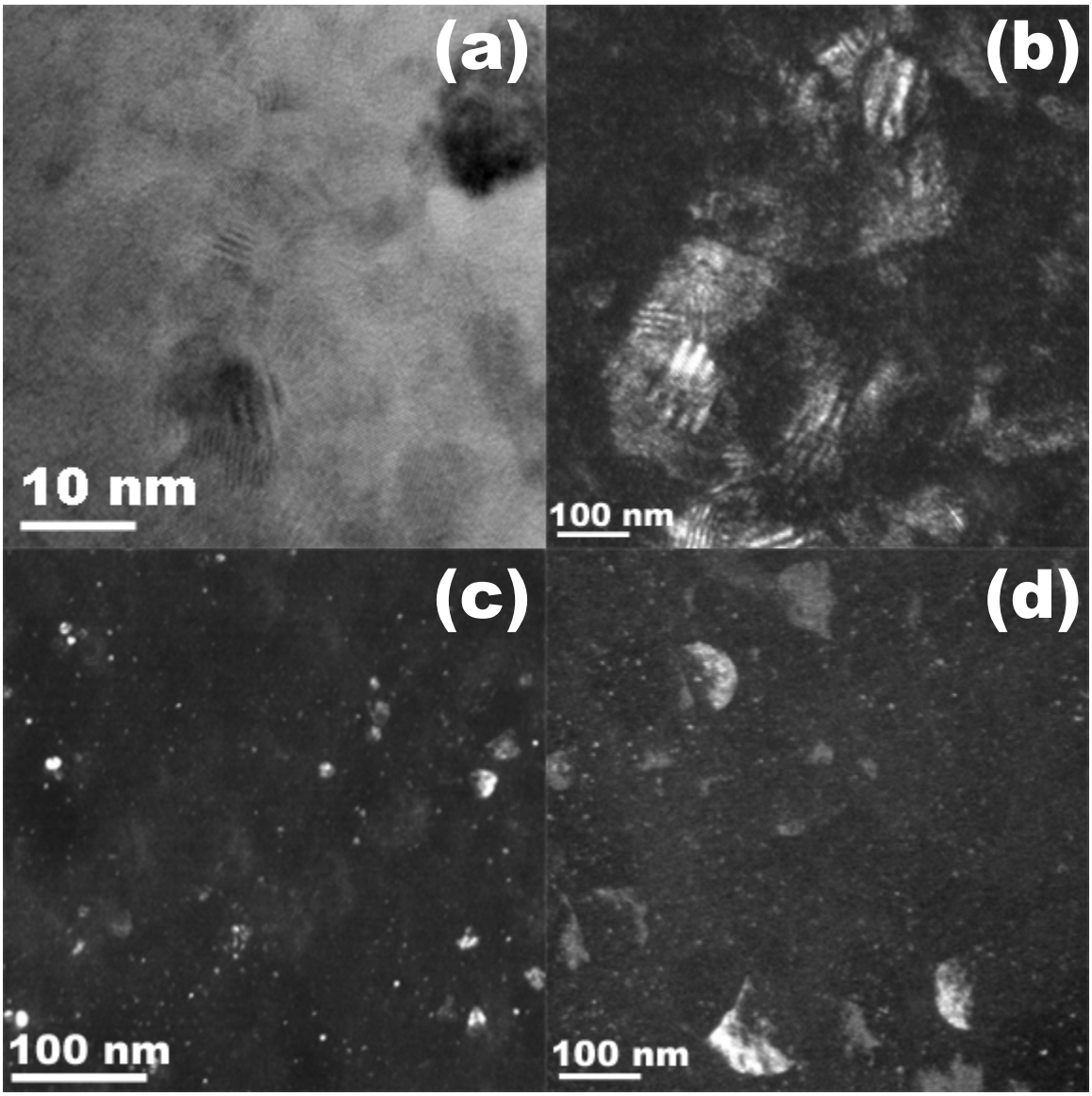

Fig. 58. Electron micrographs of (a) electron irradiated MG1 (bright field), (b) Cu irradiated MG1 (dark field), (c) He irradiated MG2 and (dark field), (d) Cu irradiated MG2 (dark field). Micrographs compare nanocrystal sizes among different irradiated specimens.

used in these experiments, $Cu_{50}Zr_{45}Ti_5$ and $Zr_{55}Cu_{30}Al_{10}Ni_5$ are rich in both Cu and Zr. On the Cu-Zr phase diagram [89], shown in Fig. 59, $Cu_{10}Zr_7$ is stable over a large range of Zr concentrations. In $Zr_{55}Cu_{30}Al_{10}Ni_5$ the atomic ratio of Zr to the total amount of Cu and Zr is (0.45 / (0.50 + 0.45)) = ~47% Zr, and for $Zr_{55}Cu_{30}Al_{10}Ni_5$ the ratio is (0.55 / (0.30 + 0.55)) = ~65% Zr. Both atomic ratios calculated above lie in the range of allowed compositions for $Cu_{10}Zr_7$ and $CuZr_2$, so it is reasonable to believe that both phases could be found in the tested metallic glass compositions. There is also evidence for the formation of a $NiZr_2$ phase in He irradiated and Cu irradiated $Zr_{55}Cu_{30}Al_{10}Ni_5$. There is much more Zr than Ni in this system and looking at the Ni-Zr binary phase diagram [90] in Fig. 60, the $NiZr_2$ phase is seen on the Zr-rich side of the diagram. The $NiZr_2$ phase on the phase diagram exists in a range that covers the Zr/(Ni+Zr) ratio of (0.55 / (0.55 + 0.60)) = ~92% Zr. In all cases, the nucleated phases were the same as those found in isothermal annealing of $Cu_{50}Zr_{45}Ti_5$ [91] and $Zr_{55}Cu_{30}Al_{10}Ni_5$ [88]. However, as discussed later, phase prediction of irradiated glasses cannot solely be based on phase diagrams.

It is worthwhile to note the similarities between $CuZr_2$ and $NiZr_2$. Both exist in the same stoichiometric ratios. The elements Cu and Ni are next to each other on the periodic table, and correspondingly have similar electronegativities (1.8 and 1.9) and have similar atomic ratios (0.125 nm and 0.128 nm). Both $CuZr_2$ and $NiZr_2$ phases are tetragonal structures. This may imply similar solubility of $CuZr_2$ and $NiZr_2$ phases. There may be a single phase that exists in a $(Ni_x, Cu_{1-x})Zr_2$ form. This form has been known to exist in Fe-Cr-Ni-Zr alloy systems [69, 70]. This applies to the bimodal nanocrystal size distribution seen in MG2. The small nanocrystal mode may be either Ni containing phase, $NiZr_2$ or $(Ni_x, Cu_{1-x})Zr_2$. It is then likely that the larger crystals are $Cu_{10}Zr_7$ since it is such a large cell and Cu and Zr are the majority elements in the material. Introducing minor elements to a metallic glass

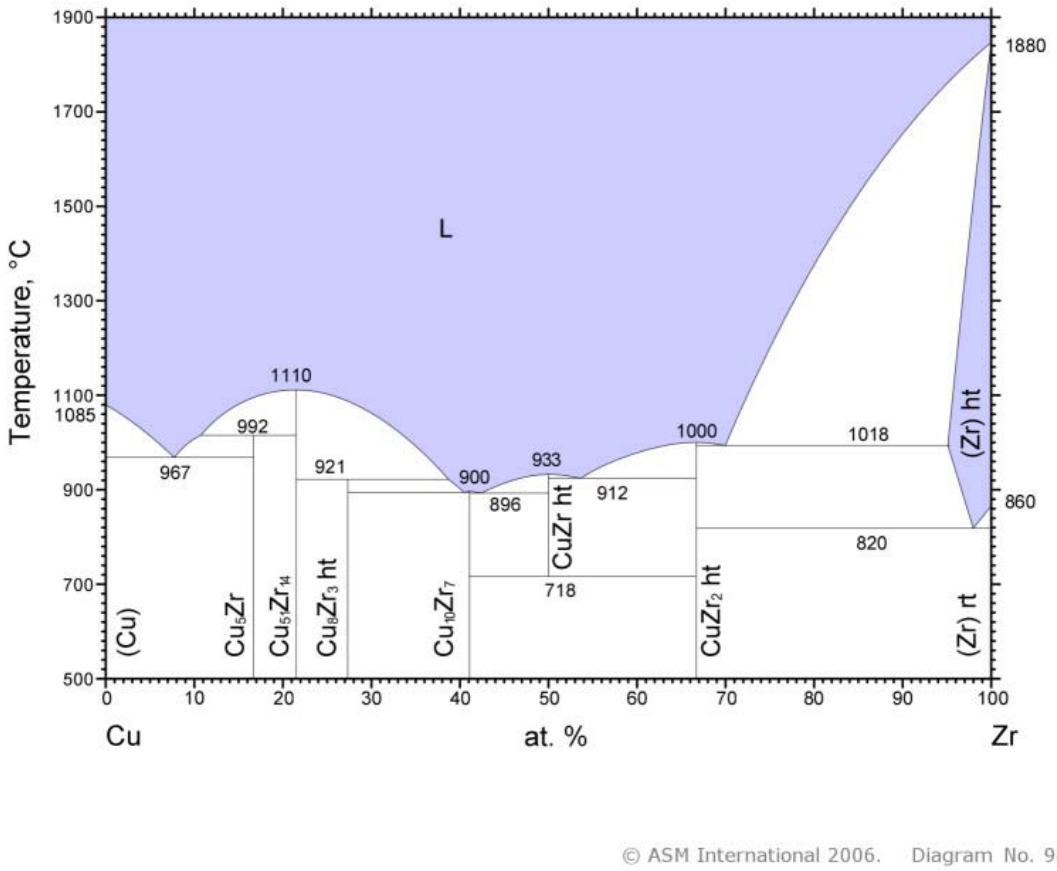

Fig. 59. Simplified copper-zirconium binary phase diagram.

Source: [89].

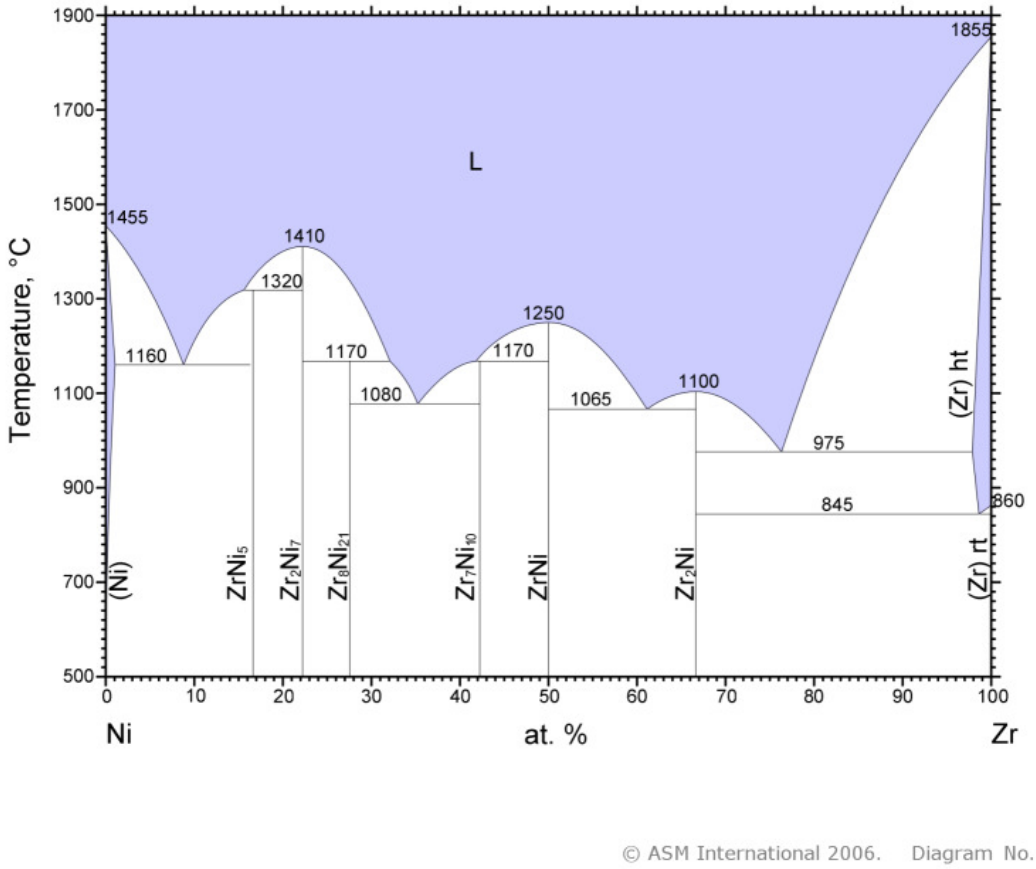

Fig. 60. Simplified nickel-zirconium binary phase diagram.

Source: [90].

may be a way to limit the nanocrystal size and increase radiation tolerance.

One might ask why no other Cu- or Zr- phases appear after irradiation. One explanation is that some binary alloys formed by atoms in these glasses form isomorphous systems, i.e., there is unlimited solid solubility in both the liquid and solid phase. In an isomorphous system, no crystalline phases will nucleate because the two phases can exist in any proportion. Examples of isomorphous systems that exist based on atoms from the metallic glasses of this experiment are Cu-Ni [92] and Ti-Zr [93]. It is also possible that other phases may form in the glass under irradiation, but they are unstable in the presence of radiation. Some structures are not stable under irradiation and will decompose and form other phases as the free energy of the system increases [94]. An example of this would be the formation of the CuZr phase in electron irradiated $Cu_{50}Zr_{45}Ti_5$ [33] and bulk Zr-Cu-Al composites [75], but it is not found after annealing [91]. In the case of Xie et al. [33], the CuZr phase was found from TEM DP analysis during in-situ electron irradiation, but that phase was not found during our analysis. However, our analysis was done at an electron flux of about 6.9×10^{23} electrons/$m^2 - s$, which is around one order of magnitude higher than the flux (8×10^{22} electrons/$m^2 - s$) in the above mentioned study. In Y.F. Sun et al. [75], the CuZr was found in a bulk sample where the cooling rate was fast, but the phase was absent in the region where the cooling rate is slow. According to the Cu-Zr phase diagram, CuZr is a high temperature phase and not stable below 718 °C. Therefore, at room temperature, the CuZr phase is not expected to form. If CuZr forms under quenching conditions in the work by Sun et al., it then may be quenched in as the material is cooled to room temperature. The CuZr phase may also form under low flux irradiation. According to the kinetics of phase transformation, the CuZr phase would be very likely to form during ion irradiation since it structure is monoclinic, the simplest of all binary structures [31] and little reorganization is

necessary. At high fluxes, the CuZr phase may not be stable relative to other phases due to increased system free energy and will decompose into more stable $Cu_{10}Zr_7$ or $CuZr_2$ phases as demonstrated by the experiments performed in this study. It should be noted that the phase diagrams cannot completely predict the formation of crystals in metallic glasses due to particle irradiation. Irradiation induced nanocrystal formation is a non-equilibrium process while phase diagrams assume a thermal equilibrium throughout a material. Ion irradiation takes place on the nanometer scale and on picosecond time increments, while phase diagrams typically assume a bulk material heated throughout. Ion irradiation of metallic glasses represents a very complicated and unique system with thermodynamics and kinetics not examined before. The discussion here should help aid in understanding of radiation response of metallic glasses in an effort to help develop methods to control nanocrystal growth.

CHAPTER XI

CONCLUSION

It is been shown that ion irradiation of metallic glasses indeed causes nanocrystallization. The addition of free volume due to displaced atoms increases the diffusivity locally causing small pockets of mobile atoms leading to elemental segregation and eventually crystallization. Additionally, this dissertation demonstrated that the nanocrystal size can be controlled by both the irradiation conditions and the relative abundance of elements in the glass composition. Light particles can create small crystals and heavy particles can create large crystals. It seems likely to assume that the volume fraction of crystalline material in an amorphous matrix could be continually increased with further irradiation, leading to any volume fraction required. On the other hand, the addition of minor elements can also decrease overall crystallization because of the decreased density of available atoms with which to bond. In other words, if a crystal phase has nucleated, increasing the number of elements different that those in a given a phase will decrease the local density of elements that are a part of the given nucleated phase. If the phase is made of primarily major elements in the composition, the size will be limited due to increased minority elements. If the nucleated phase is made primarily of minority elements, then the crystal size will be limited because there will be so few atoms to bond with from the beginning. This could possibly lead to more radiation-tolerant metallic glasses since the crystallization would be suppressed.

The addition of nanocrystals to metallic glass can lead to improved properties of an already attractive material. With high strength and high ductility, there could be endless applications of amorphous metallic alloys with dispersed nanocrystals. The current study, however, is limited to the near-surface region of materials because

the mass and energies used here do not penetrate more than a micrometer into a specimen. This leads to a small overall volume fraction of crystallization. Perhaps a small overall volume fraction is all that is required for the particular application.

With an increase in energy, particles are able to penetrate deeper into a material, so a larger layer of nanocrystals could be made as particles, particularly light particles such as electrons and He ions, are accelerated to higher energies. Of course care must be taken not to induce any nuclear reactions which can happen as nuclei interact at high energies. If the density of the glass can be reduced, possibly by the implantation of gaseous ions or an advanced quenching technique, particles would be able to penetrate deeper into a material leading to an increased volume fraction of crystals.

This dissertation has been a very interesting look into the thermodynamics and kinetics of an amorphous material. Classical radiation materials science deals with ordered structures, either polycrystalline or monocrystalline, while here we have dealt with the opposite structure - a completely disordered structure. The common idea of "interstitials," "vacancies," and "defects" do not apply, but the terms can be loosely translated when speaking of excess volume in the amorphous material. Many problems often arose when dealing with a material that is metastable from the beginning. The material has to be dealt with very carefully to ensure that the changes made to it come from the intended source and not by some other mechanism - atoms themselves do not care where the energy came from, they will use it regardless.

This is by no means the end of radiation experiments on metallic glasses. More work is needed to study crystallization behavior and eventually materials properties of metallic glasses with dispersed nanocrystals. The author plans on doing dose-dependent studies as well as cross-sectional TEM studies on irradiated metallic glasses to further understand and predict nanocrystallization. Also, other glasses outside the

Cu-Zr system need to be studied to understand a more general picture of nanocrystallization in metallic glasses. Still, the data presented in this dissertation represents a new body of knowledge that will help the rest of the scientific community understand the crystallization behavior of metallic glasses.

REFERENCES

[1] A. Inoue, "Stabilization of metallic supercooled liquid and bulk amorphous alloys," *Acta Materialia*, vol. 48, pp. 279–306, 2000.

[2] F. Faupel, W. Frank, M. P. Macht, H. Mehrer, V. Naundorf, K. Ratzke, H. R. Schober, S. K. Sharma, and H. Teichler, "Diffusion in metallic glasses and supercooled melts," *Reviews of Modern Physics*, vol. 75, pp. 237–280, 2003.

[3] A. L. Greer, K. L. Rutherford, and I. M. Hutchings, "Wear resistance of amorphous alloys and related materials," *International Materials Reviews*, vol. 47, pp. 87–112, 2002.

[4] C. A. Pampillo, "Flow and fracture in amorphous alloys," *Journal of Materials Science*, vol. 10, pp. 1194–1227, 1975.

[5] C. A. Schuh and T. G. Nieh, "A survey of instrumented indentation studies on metallic glasses," *Journal of Materials Research*, vol. 19, pp. 46–57, 2004.

[6] W. H. Wang, C. Dong, and C. H. Shek, "Bulk metallic glasses," *Materials Science and Engineering R*, vol. 44, pp. 45–89, 2004.

[7] A. Inoue, W. Zhang, T. Zhang, and K. Kurosaka, "High-strength Cu-based bulk glassy alloys in Cu-Zr-Ti and Cu-Hf-Ti ternary systems," *Acta Materialia*, vol. 49, pp. 2645–2652, 2001.

[8] K. Amiya, A. Urata, N. Nishiyama, and A. Inoue, "Fe-B-Si-Nb bulk metallic glasses with high strength above 4000 MPa and distinct plastic elongation," *Materials Transactions*, vol. 45, pp. 1214–1218, 2004.

[9] G. E. Dieter, *Mechanical Metallurgy*, 3rd edition, London: McGraw-Hill, 1988.

[10] M. Naka, "Corrosion resistivity of amorphous iron alloys containing chromium," *The Journal of the Japan Institute of Metals*, vol. 38, pp. 835–841, 1974.

[11] H. M. Lin, J. K. Wu, C. C. Wang, and P. Y. Lee, "The corrosion behavior of mechanically alloyed CuZrTi bulk metallic glasses," *Materials Letters*, vol. 62, pp. 2995–2998, 2008.

[12] T. Meydan and G. W. Healey, "Linear variable differential transformer - linear displacement transducer utilizing ferromagnetic amorphous metallic glass ribbons," *Sensors and Actuators A*, vol. 32, pp. 582–587, 1992.

[13] M. Telford, "The case for bulk metallic glass," *Materials Today*, vol. 7, pp. 36–43, 2004.

[14] A. Peker and W. L. Johnson, "A highly processable metallic glass $Zr_{41.2}Ti_{13.8}Cu_{12.5}Ni_{10.0}Be_{22.5}$," *Applied Physics Letters*, vol. 63, pp. 2342–2344, 1993.

[15] Y. C. Choi and S. I. Hong, "Mechanical properties and microstructure of commercial amorphous golf club heads made of Zr-Ti-Cu-Ni-Be bulk metallic glass," *Materials Science and Engineering A*, vol. 449-451, pp. 126–129, 2007.

[16] E. O. Hall, "The deformation and ageing of mild steel iii discussion of results," *Proceedings of the Physical Society of London Section B*, vol. 64, pp. 747–753, 1951.

[17] N. J. Petch, "The cleavage strength of polycrystals," *Journal of the Iron and Steel Institute*, vol. 174, pp. 25–28, 1953.

[18] N. J. Petch, "The ductile-cleavage strength transition in alpha-iron," in *Proceedings of an International Conference on the Atomic Mechanisms of Fracture*

held in Swampscott, Massachusetts, April 12-16, 1959, pp. 54–67.

[19] S. M. Bruemmer, E. P. Simonen, P. M. Scott, P. L. Andresen, G. S. Was, and J. L. Nelson, "Radiation-induced material changes and susceptibility to intergranular failure of light-water-reactor core internals," *Journal of Nuclear Materials*, vol. 274, pp. 299–314, 1999.

[20] G. S. Was, *Fundamentals of Radiation Materials Science*, Berlin: Springer, 2007.

[21] A. Jenssen, L. G. Ljungberg, J. Walmsley, and S. Fisher, "Importance of molybdenum on irradiation-assisted stress corrosion cracking in austenitic stainless steels," *Corrosion*, vol. 54, pp. 48–60, 1998.

[22] L. S. Langston, "Crown jewels," *Mechanical Engineering Magazine Online*, February 2006. Available: http://memagazine.asme.org.

[23] C. A. Schuh, T. C. Hufnagel, and U. Ramamurty, "Mechanical behavior of amorphous alloys," *Acta Materialia*, vol. 55, pp. 4067–4109, 2007.

[24] D. C. Hofmann, J. Y. Suh, A. Wiest, G. Duan, M. L. Lind, M. D. Demetriou, and W. L. Johnson, "Designing metallic glass matrix composites with high toughness and tensile ductility," *Nature*, vol. 451, pp. 1085–1090, 2008.

[25] K. Lu, "Nanocrystalline metals crystallized from amorphous solids - nanocrystallization, structure, and properties," *Materials Science and Engineering R*, vol. 16, pp. 161–221, 1996.

[26] Q. S. Zhang, W. Zhang, G. Q. Xie, K. S. Nakayama, H. Kimura, and A. Inoue, "Formation of bulk metallic glass in situ composites in $Cu_{50}Zr_{45}Ti_5$ alloy," *Journal of Alloys and Compounds*, vol. 431, pp. 236–240, 2007.

[27] C. Fan, A. Takeuchi, and A. Inoue, "Preparation and mechanical properties of zr-based bulk nanocrystalline alloys containing compound and amorphous phases," *Materials Transactions*, vol. 40, pp. 42–51, 1999.

[28] J. J. Kim, Y. Choi, S. Suresh, and A. S. Argon, "Nanocrystallization during nanoindentation of a bulk amorphous metal alloy at room temperature," *Science*, vol. 295, pp. 654–657, 2002.

[29] M. L. Trudeau, J. Y. Huot, R. Schulz, D. Dussault, A. Van Neste, and G. L'Esperance, "Nanocrystalline Fe-(Co,Ni)-Si-B the mechanical crystallization of amorphous alloys and the effects on electrocatalytic reactions," *Physical Review B*, vol. 45, pp. 4626–4636, 1992.

[30] H. Chen, Y. He, G. J. Shiflet, and S. J. Poon, "Deformation-induced nanocrystal formation in shear bands of amorphous alloys," *Nature*, vol. 367, pp. 541–543, 1994.

[31] M. Nastasi and J. W. Mayer, "Thermodynamics and kinetics of phase transformations induced by ion irradiation," *Materials Science Reports*, vol. 6, pp. 1–51, 1991.

[32] T. Nagase, M. Nakamura, and Y. Umakoshi, "Electron irradiation induced nanocrystallization in $Zr_{66.7}Ni_{33.3}$ amorphous alloy and $Zr_{60}Al_{15}Ni_{25}$ metallic glass," *Intermetallics*, vol. 15, pp. 211–224, 2007.

[33] G. Xie, Q. Zhang, D. V. Louzguine-Luzgin, W. Zhang, and A. Inoue, "Nanocrystallization of $Cu_{50}Zr_{45}Ti_5$ metallic glass induced by electron irradiation," *Materials Transactions*, vol. 47, pp. 1930–1933, 2006.

[34] L. C. Chen and F. Spaepen, "Calorimetric evidence for the micro-quasicrystalline

structure of 'amorphous' Al/transition metal alloys," *Nature*, vol. 336, pp. 366–368, 1988.

[35] W. H. Wang, E. Wu, R. J. Wang, S. J. Kennedy, and A. J. Studer, "Phase transformation in a $Zr_{41}Ti_{14}Cu_{12.5}Ni_{10}Be_{22.5}$ bulk amorphous alloy upon crystallization," *Physical Review B*, vol. 66, pp. 104205, 2002.

[36] R. Busch, "The thermophysical properties of bulk metallic glass-forming liquids," *JOM*, vol. 52, pp. 39–42, 2000.

[37] H. Okamoto, "Cu-Zr (copper-zirconium)," *Journal of Phase Equilibria and Diffusion*, vol. 29, pp. 204, 2008.

[38] W. Klement, F. H. Willens, and P. Duwez, "Non-crystalline structure in solidified gold-silicon alloys," *Nature*, vol. 187, pp. 869–870, 1960.

[39] Y. J. Kim, R. Busch, W. L. Johnson, A. J. Rulison, and W. K. Rhim, "Experimental determination of a time-temperature-transformation diagram of the undercooled $Zr_{41.2}Ti_{13.8}Cu_{12.5}Ni_{10.0}Be_{22.5}$ alloy using the containerless electrostatis levitation processing technique," *Applied Physics Letters*, vol. 68, pp. 1057–1059, 1996.

[40] A. Masuhr, T. A. Waniuk, R. Busch, and W. L. Johnson, "Time scales for viscous flow, atomic transport, and crystallization in the liquid and supercooled liquid states of $Zr_{41.2}Ti_{13.8}Cu_{12.5}Ni_{10.0}Be_{22.5}$," *Physical Review Letters*, vol. 82, pp. 2290–2293, 1999.

[41] F. E. Luborsky, *Amorphous Metallic Alloys*, London: Butterworths Monographs in Materials, 1983.

[42] M. H. Cohen and D. Turnbull, "Molecular transport in liquids and glasses," *The Journal of Chemical Physics*, vol. 31, pp. 1164–1169, 1959.

[43] F. Spaepen, "A microscopic mechanism for steady state inhomogeneous flow in metallic glasses," *Acta Metallurgica*, vol. 25, pp. 407–415, 1977.

[44] Y. Limoge and G. Brebec, "Relation between viscosity and diffusion in amorphous metallic alloys," *Acta Metallurgica*, vol. 36, pp. 665–673, 1988.

[45] A. van den Beukel, "Analysis of structural relaxation data in metallic glasses in terms of different models," *Acta Metallurgica et Materialia*, vol. 39, pp. 2709–2717, 1991.

[46] R. B. Pond and J. M. Winter, "Calorimetric comparison of quench rates in melt spinning and melt extraction," *Materials Science and Engineering*, vol. 23, pp. 87–89, 1976.

[47] R. W. Cahn and A. L. Greer, *Physical Metallurgy*, vol. 2, 4th edition, Amsterdam: Elsevier Science B.V., 1996.

[48] M. Nastasi, J. W. Mayer, and J. K. Hirvonen, *Ion-Solid Interactions*, Cambridge: Cambridge University Press, 1996.

[49] J. F. Ziegler, J. P. Biersack, and U. Littmark, *The Stopping and Range of Ions in Solids*, New York: Pergamon, 1985.

[50] O. B. Firsov, "A qualitative interpretation of the mean electron excitation energy in atomic collisions," *Sov. Phys. JETP*, vol. 36, pp. 1076, 1959.

[51] G. H. Kinchin and R. S. Pease, "The displacement of atoms in solids by radiation," *Reports on Progress in Physics*, vol. 18, pp. 1–51, 1955.

[52] J. A. Brinkman, "Production of atomic displacements by high-energy particles," *American Journal of Physics*, vol. 24, pp. 246–267, 1956.

[53] S. Bellini, A. Montone, and M. Vittori-Antisari, "Radiation-enhanced diffusion in amorphous Ni-Zr studied by in situ electron irradiation in a transmission electron microscope," *Physical Review B*, vol. 50, pp. 9803–9809, 1994.

[54] V. Rosato and F. Cleri, "A molecular dynamics simulation of the effects of excess free volume on the diffusion in metallic glasses," *Journal of Non-Crystalline Solids*, vol. 144, pp. 187–195, 1992.

[55] I. Jencic, M. W. Bench, I. M. Robertson, and M. A. Kirk, "Electron-beam-induced crystallization of isolated amorphous regions in Si, Ge, Gap, and GaAs," *Journal of Applied Physics*, vol. 78, pp. 974–982, 1995.

[56] D. E. Newbury and R. L. Myklebust, "Simulation of electron-excited X-ray spectra with NIST-NIH Desktop Spectrum Analyzer (DTSA)," *Surface and Interface Analysis*, vol. 37, pp. 1045–1053, 2005.

[57] K. Lu and J. T. Wang, "Activation energies for crystal nucleation and growth in amorphous alloys," *Materials Science and Engineering A*, vol. 133, pp. 500–503, 1991.

[58] D. T. A. Matthews, V. Ocelik, P. M. Bronsveld, and J. Th. M. De Hosson, "An electron microscopy appraisal of tensile fracture in metallic glasses," *Acta Materialia*, vol. 56, pp. 1762–1773, 2008.

[59] A. Leonhard, L. Q. Xing, M. Heilmaier, A. Gebert, J. Eckert, and L. Schultz, "Effect of crystalline precipitations on the mechanical behavior of bulk glass forming Zr-based alloys," *Nanostructured Materials*, vol. 10, pp. 805–817, 1998.

[60] B. M. Clemens, H. Kung, and S. A. Barnett, "Structure and strength of multilayers," *MRS Bulletin*, vol. 24, pp. 20, 1999.

[61] C. Fan and A. Inoue, "Ductility of bulk nanocrystalline composites and metallic glasses at room temperature," *Applied Physics Letters*, vol. 77, pp. 46, 2000.

[62] E. G. Fu, J. Carter, M. Martin, G. Xie, X. Zhang, Y. Q. Wang, R. Littleton, and L. Shao, "Electron irradiation-induced structural tranformation in metallic glasses," *Scripta Materialia*, vol. 61, pp. 40–43, 2009.

[63] R. G. Walmsley, A. F. Marshall, D. Bouchet, and D. A. Stevenson, "Crystallization of amorphous $Cu_{60}Zr_{40}$ prepared by magnetron sputter deposition," *Journal of Non-Crystalline Solids*, vol. 54, pp. 277–300, 1983.

[64] C. E. Lundin, D. J. McPherson, and M. Hansen, "System zirconium-copper," *Journal of Metals*, vol. 5, pp. 273–278, 1953.

[65] Z. Altounian, E. Batalla, J. O. Strom-Olsen, and J. L. Walter, "The influence of oxygen and other impurities on the crystallization of $NiZr_2$ and related metallic glasses," *Journal of Applied Physics*, vol. 61, pp. 149–155, 1987.

[66] L. Liu, Z. F. Wu, and J. Zhang, "Crystallization kinetics of $Zr_{55}Cu_{30}Al_{10}Ni_5$ bulk amorphous alloy," *Journal of Alloys and Compounds*, vol. 339, pp. 90–95, 2002.

[67] N. Mattern, U. Khn, H. Hermann, S. Roth, H. Vinzelberg, and J. Eckert, "Thermal behavior and glass transition of Zr-based bulk metallic glasses," *Materials Science and Engineering A*, vol. 375-377, pp. 351–354, 2004.

[68] T. Nagase and Y. Umakoshi, "Thermal stability and electron irradiation effect on Zr-based amorphous alloys," *Journal of Applied Physics*, vol. 93, pp. 912–918,

2003.

[69] S. M. McDeavitt, D. P. Abraham, and J. Y. Park, "Evaluation of stainless steel-zirconium alloys as high-level nuclear waste forms," *Journal of Nuclear Materials*, vol. 257, pp. 21–34, 1998.

[70] D. P. Abraham, J. W. Richardson Jr., and S. M. McDeavitt, "Laves intermetallics in stainless steel-zirconium alloys," *Materials Science and Engineering A*, vol. 237-240, pp. 658–664, 1997.

[71] D. V. Louzguine, H. Kato, and A. Inoue, "High-strength Cu-based crystal-glassy composite with enhanced ductility," *Applied Physics Letters*, vol. 84, pp. 1088–1089, 2004.

[72] E. M. Carvalho and I. R. Harris, "Constitutional and structural studies of the intermetallic phase, ZrCu," *Journal of Materials Science*, vol. 15, pp. 1224–1230, 1980.

[73] P. Garoche and J. Bigot, "Comparison between amorphous and crystalline phases of copper-zirconium alloys by specific-heat measurements," *Physical Review B*, vol. 28, pp. 6886–6895, 1983.

[74] H. R. Wang, Y. F. Ye, Z. Q. Shi, X. Y. Teng, and G. H. Min, "Crystallization processes in amorphous $Zr_{54}Cu_{46}$ alloy," *Journal of Non-Crystalline Solids*, vol. 311, pp. 36–41, 2002.

[75] Y. F. Sun, B. C. Wei, Y. R. Wang, W. H. Li, T. L. Cheung, and C. H. Shek, "Plasticity-improved ZrCuAl bulk metallic glass matrix composites containing martensite phase," *Applied Physics Letters*, vol. 87, pp. 1–3, 2005.

[76] L. Ge, X. Hui, E. R. Wang, G. L. Chen, R. Arroyave, and Z. K. Liu, "Prediction of the glass forming ability in Cu-Zr binary and Cu-Zr-Ti ternary alloys," *Intermetallics*, vol. 16, pp. 27–33, 2008.

[77] A. Meldrum, S. J. Zinkle, L. A. Boatner, and R. C. Ewing, "A transient liquid-like phase in the displacement cascades of zircon, hafnon and thorite," *Nature*, vol. 395, pp. 56–58, 1998.

[78] C. Gaukel, M. Kluge, and H. R. Schober, "Diffusion and relaxations in liquid and amorphous metals," *Philosophical Magazine B*, vol. 79, pp. 1907–1914, 1999.

[79] M. Kluge and H. R. Schober, "Diffusion in a binary amorphous metal - pair-correlation in $Cu_{33}Zr_{67}$," *Journal of Non-Crystalline Solids*, vol. 352, pp. 5093–5097, 2006.

[80] P. J. Tao, Y. Z. Yang, X. J. Bai, Z. X. Mu, G. Q. Li, Z. W. Xie, and X. C. Chen, "Study on implantation of Co ions in ZrCuAlNi bulk metallic glass," *Surface and Coatings Technology*, vol. 203, pp. 1656–1659, 2009.

[81] S. Nagata, S. Higashi, B. Tsuchiya, K. Toh, T. Shikama, K. Takahiro, K. Ozaki, K. Kawatusra, S. Yamamoto, and A. Inouye, "Ion irradiation effects on amorphization and thermal crystallization in ZrAlNiCu alloys," *Nuclear Instruments and Methods in Physics Research B*, vol. 257, pp. 420–423, 2007.

[82] T. S. Chin, C. Y. Lin, M. C. Lee, R. T. Huang, and S. M. Huang, "Bulk nano-crystalline alloys," *Materials Today*, vol. 12, pp. 34 – 39, 2009.

[83] D. B. Williams and C. B. Carter, *Transmission Electron Microscopy: A Textbook for Materials Science*, New York: Plenum Press, 1996.

[84] N. Van Steenberge, A. Concustell, J. Sort, J. Das, N. Mattern, A. Gebert, S. Surinach, J. Eckert, and M. D. Baro, "Microstructural inhomogeneities introduced in a Zr-based bulk metallic glass upon low-temperature annealing," *Materials Science and Engineering A*, vol. 491, pp. 124–130, 2008.

[85] S. Pauly, J. Das, N. Mattern, D. H. Kim, and J. Eckert, "Phase formation and thermal stability in Cu-Zr-Ti(Al) metallic glasses," *Intermetallics*, vol. 17, pp. 453–462, 2009.

[86] J. A. Davies, *Surface Modification and Alloying by Laser, Ion and Electron Beams*, New York: Plenum Press, 1983.

[87] H. H. Andersen, "The depth resolution of sputter profiling," *Applied Physics A*, vol. 18, pp. 131–140, 1979.

[88] J. Zhang, Y. H. Wei, K. Q. Qiu, H. F. Zhang, M. X. Quan, and Z. Q. Hu, "Crystallization kinetics and pressure effect on crystallization of $Zr_{55}Al_{10}Ni_5Cu_{30}$ bulk metallic glass," *Materials Science and Engineering A*, vol. 357, pp. 386–391, 2003.

[89] M. Hamalainen, N. Bochvar, L. L. Rokhlin, and K. Zeng, "Cu-Zr phase diagram," ASM Alloy Phase Diagrams Center, P. Villars, editor-in-chief; H. Okamoto and K. Cenzual, section editors; http://www.asminternational.org/AsmEnterprise/APD, ASM International, Materials Park, OH, 2006.

[90] N. Saunders, "Ni-Zr phase diagram," ASM Alloy Phase Diagrams Center, P. Villars, editor-in-chief; H. Okamoto and K. Cenzual, section editors; http://www.asminternational.org/AsmEnterprise/APD, ASM International, Materials Park, OH, 2006.

[91] G. Xie, D. V. Louzguine-Luzgin, Q. Zhang, W. Zhang, and A. Inoue, "Structure and crystallization kinetics of a $Cu_{50}Zr_{45}Ti_5$ glassy alloy," *Journal of Alloys and Compounds*, 2008, doi:10.1016/j.jallcom.2008.07.191.

[92] Y. W. Chung, *Introduction to Materials Science and Engineering*, Boca Raton: CRC Press, 2007.

[93] T. Fukunaga, S. Shibuya, K. Suzuki, and M. Misawa, "Chemical fluctuation of Ti-Zr isomorphous alloy obtained by rapid quenching," *Journal of Materials Science Letters*, vol. 6, pp. 1435–1436, 1987.

[94] K. Y. Liou and P. Wilkes, "The radiation disorder model of phase stability," *Journal of Nuclear Materials*, vol. 87, pp. 317–330, 1979.

VITA

Name: Jesse Carter

Address: Department of Nuclear Engineering

Texas A&M University

3133 TAMU

College Station, TX 77843-3133

Email: jesse.carter@gmail.com

Education: B.S. Nuclear Engineering

Texas A&M University

2003

M.S. Nuclear Engineering

Texas A&M University

2006

Ph.D. Nuclear Engineering

Texas A&M University

2009